NANYANG TECHNOLOGICAL UNIVERSITY

SENSITIZTION OF TIO_2 NANOSTRUCTURES FOR PHOTOELECTROCHEMCIAL HYDROGEN GENERATION

LUO JINGSHAN

SCHOOL OF PHYSICAL AND MATHEMATICAL SCIENCES

2013

SENSITIZTION OF TIO_2 NANOSTRUCTURES FOR PHOTOELECTROCHEMCIAL HYDROGEN GENERATION

LUO JINGSHAN

2013

SENSITIZTION OF TiO_2 NANOSTRUCTURES FOR PHOTOELECTROCHEMCIAL HYDROGEN GENERATION

LUO JINGSHAN

School of Physical and Mathematical Sciences

A thesis submitted to the Nanyang Technological University
in fulfillment of the requirement for the degree of
Doctor of Philosophy

2013

Acknowledgements

PhD is a long journey for me. In the past four years, I have learnt a lot, experienced a lot, and gained a lot. There are successes and failures, joys and pains, progresses and struggles. I will keep the enthusiasm to search for the unknown, and continue to work hard in the future. This thesis is not possible without the guidance and help from the people around me, and I would like to take this opportunity to express my sincere thanks to them.

First of all, I would like to thank my supervisor, Professor Fan Hongjin, for his inspiring guidance and continuous support. I really learnt a lot from him, not only the knowledge in research, but also the attitude for life. Professor Yu Ting, Professor Shen Zexiang and Professor Sun Handong also helped me a lot, especially for the usage of their equipment.

I would also like to thank my colleagues and friends, especially Dr. Cheng Chuanwei, for his help with the experimental techniques; Dr Luo Yongsong, for introducing me to a new research area; Dr Siva Krishna Karuturi and Mr Liu Jilei, for the close collaboration. And all the others, namely Dr Ignacio Minguez Bacho, Dr Liu Monan, Mr Li Xianglin, Miss Ma Lin, Mr Guan Cao, Dr Jiang Jian, Dr Xing Guichuan, Dr Xia Xinhui, Dr Qi Xiaoying, Mr Chi Fan Ng, Dr Zeng Zhiyuan, Mr Zhao Guanjia and Mr Li Yong for their kind assistance, suggestions and collaborations. I also appreciate the help from the technical and academic staff from general office in our division.

Finally, my deepest gratitude goes to my family and my girlfriend, for their unselfish and continuous support and encouragement.

Table of Contents

Summary

Energy is an eternal research topic concerning the continuous development of our society and daily life. Finding a sustainable, green and efficient way to harvest, store and use the energy is highly demanded. This thesis is part of my research efforts for developing efficient and low cost material systems for energy conversion and storage.

With the inspiration from my undergraduate experiences in quantum dots synthesis, I have decided to choose the sensitization of TiO_2 with short band gap semiconductors for photoelectrochemical (PEC) hydrogen generation as my research topic. This thesis contains mainly three parts, chapter 1, chapters 2-4 and chapter 5. Chapter 1 is a general introduction, focusing on three parts: an overview of the energy demands and challenges, an introduction of the basic principles and working mechanisms of the PEC cell, and a short review of the recent advancement of using TiO_2 for PEC hydrogen generation. Chapter 2-4 are the main body of the thesis, which describes the experiments and strategies I have carried out and developed to improve the efficiency of hydrogen generation. In specific, chapter 2 is focused on the study of different kinds of sensitizers, their optical properties, band edge positions, electron injection efficiencies and stability for PEC hydrogen generation. Studying these properties provides a physical background for the design of efficient PEC system. Chapter 3 is focused on improving the surface area of TiO_2. TiO_2 inverse opal has attracts wide attention in the application of dye sensitized solar cell and

semiconductor sensitized solar cell due to its unique three-dimensional structure. However, its surface area is still low, thus the efficiency is low compared to the conventional TiO_2 nanoparticles. In this chapter, we try to improve the surface area of TiO_2 inverse opal by further growth of ZnO nanowires inside. The higher surface area would result in higher amount of sensitizer loading and more active sites for water splitting reactions. Thus the CdS sensitized hierarchical structure shows nearly double photocurrent of the pristine TiO_2 inverse opal with CdS sensitization. In chapter 4, a new sensitization method ALDIER based on atomic layer deposition (ALD) and ion exchange reaction (IER) has been developed. Deep penetration of the sensitizers into the complex nanostructures has been a challenge for a long time in improving the efficiency of short band gap semiconductor sensitized device. This is mainly due to the large size of the sensitizer and the high aspect ratio of the complex nanostructure for sensitization. ALD is a powerful thin film deposition technique, which could provide homogeneous coating on high aspect ratio nanostructures with excellent step coverage. However, direct deposition of the sensitizers by ALD is limited by the toxic precursors and complex processes. An indirect way by IER with the well-developed ZnO by ALD provides a great versatility for choosing different sensitizers. The newly developed ALDIER method in this chapter by combining the two powerful techniques together shows more than double the performance of the conventional successive ionic layer adsorption and reaction (SILAR) method, which solves the penetration challenge for sensitization. Chapter 5 concludes the whole thesis in a general way with the comments of the problems existed in the current material systems, as well as

the recommendations for the future efforts in overcoming the challenges and improving the efficiency of PEC cell for hydrogen generation.

In summary, this thesis studies the basic physical properties of the materials regarding the efficiency for PEC hydrogen generation first, and then provides two practical strategies to improve the efficiency by tailoring the TiO_2 nanostructures and improving the sensitizer deposition method, respectively. I hope this thesis could provide some useful information and ideas for the other researchers.

Publications

1. ***Luo, J.***; Karuturi, S. K.; Liu, L.; Su, L. T.; Tok, A. I.; Fan, H. J., Homogeneous photosensitization of complex TiO(2) nanostructures for efficient solar energy conversion. ***Scientific reports*** 2012, 2, 451.
2. Karuturi, S. K.; ***Luo, J.;(equal contribution)*** Cheng, C.; Liu, L.; Su, L. T.; Tok, A. I.; Fan, H. J., A novel photoanode with three-dimensionally, hierarchically ordered nanobushes for highly efficient photoelectrochemical cells. ***Advanced Materials*** 2012, 24, 4157-4162.
3. ***Luo, J.***; Ma, L.; He, T.; Ng, C. F.; Wang, S.; Sun, H.; Fan, H. J., TiO2/(CdS, CdSe, CdSeS) Nanorod Heterostructures and Photoelectrochemical Properties. ***The Journal of Physical Chemistry C*** 2012, 116, 11956-11963.
4. ***Luo, J.***; Liu, J.; Zeng, Z.; Ng, C. F.; Ma, L.; Zhang, H.; Lin, J.; Shen, Z.; Fan, H. J., 3D Graphene Foam Supported Fe3O4 Lithium Battery Anodes with Long Cycle Life and High Rate Capability. ***Nano Letters,*** online published DOI: 10.1021/nl403461n.
5. ***Luo, J.***; Xia, X.; Luo, Y.; Guan, C.; Liu, J.; Qi, X.; Ng, C. F.; Yu, T.; Zhang, H.; Fan, H. J., Rationally Designed Hierarchical TiO2@Fe2O3Hollow Nanostructures for Improved Lithium Ion Storage. ***Advanced Energy Materials*** 2013, 3, 737-743.
6. Xia, X.; ***Luo, J.; (equal contribution)*** Zeng, Z.; Guan, C.; Zhang, Y.; Tu, J.; Zhang, H.; Fan, H. J., Integrated photoelectrochemical energy storage:

solar hydrogen generation and supercapacitor. ***Scientific reports*** 2012, 2, 981.

7. Luo, Y.; ***Luo, J.; (equal contribution)*** Zhou, W.; Qi, X.; Zhang, H.; Yu, D. Y. W.; Li, C. M.; Fan, H. J.; Yu, T., Controlled synthesis of hierarchical graphene-wrapped TiO2@Co3O4 coaxial nanobelt arrays for high-performance lithium storage. ***Journal of Materials Chemistry A*** 2013, 1, 273-281.
8. Luo, Y.; ***Luo, J.***; Jiang, J.; Zhou, W.; Yang, H.; Qi, X.; Zhang, H.; Fan, H. J.; Yu, D. Y. W.; Li, C. M.; Yu, T., Seed-assisted synthesis of highly ordered TiO2@α-Fe2O3 core/shell arrays on carbon textiles for lithium-ion battery applications. ***Energy & Environmental Science*** 2012, 5, 6559-6566.
9. Xing, G.; ***Luo, J.***; Li, H.; Wu, B.; Liu, X.; Huan, C. H. A.; Fan, H. J.; Sum, T. C., Ultrafast Exciton Dynamics and Two-Photon Pumped Lasing from ZnSe Nanowires. ***Advanced Optical Materials*** 2013, 1, 319-326.
10. Jiang, J.; ***Luo, J.***; Zhu, J.; Huang, X.; Liu, J.; Yu, T., Diffusion-controlled evolution of core-shell nanowire arrays into integrated hybrid nanotube arrays for Li-ion batteries. ***Nanoscale*** 2013, 5, 8105-8113.
11. Zou, X.; ***Luo, J.***; Lee, D.; Cheng, C.; Springer, D.; Nair, S. K.; Cheong, S. A.; Fan, H. J.; Chia, E. E. M., Temperature-dependent terahertz conductivity of tin oxide nanowire films. ***Journal of Physics D: Applied Physics*** 2012, 45, 465101.

12. Su, L. T.; Karuturi, S. K.; ***Luo, J.***; Liu, L.; Liu, X.; Guo, J.; Sum, T. C.; Deng, R.; Fan, H. J.; Liu, X.; Tok, A. I., Photon upconversion in hetero-nanostructured photoanodes for enhanced near-infrared light harvesting. ***Advanced Materials*** 2013, 25, 1603-1607.
13. Xia, X.; Zhu, C.; ***Luo, J.***; Zeng, Z.; Guan, C.; Ng, C.F.; Zhang, H.; Fan, H. J., Synthesis of Free-Standing Metal Sulfide Nanoarrays via Anion Exchange Reaction and Their Electrochemical Energy Storage Application, ***Small***, Accepted
14. Luo, Y.; Kong, D.; ***Luo, J.***; Chen, S.; Zhang, D.; Qiu, K.; Qi, X.; Zhang, H.; Li, C. M.; Yu, T., Hierarchical TiO2 nanobelts@MnO2 ultrathin nanoflakes core–shell array electrode materials for supercapacitors. ***RSC Advances*** 2013, 3, 14413-11422.
15. Luo, Y.; Kong, D.; Jia, Y.; ***Luo, J.***; Lu, Y.; Zhang, D.; Qiu, K.; Li, C. M.; Yu, T., Self-assembled graphene@PANI nanoworm composites with enhanced supercapacitor performance. ***RSC Advances*** 2013, 3, 5851-5859.
16. Luo, Y.; Jiang, J.; Zhou, W.; Yang, H.; ***Luo, J.***; Qi, X.; Zhang, H.; Yu, D. Y. W.; Li, C. M.; Yu, T., Self-assembly of well-ordered whisker-like manganese oxide arrays on carbon fiber paper and its application as electrode material for supercapacitors. ***Journal of Materials Chemistry*** 2012, 22, 8634.
17. Pan, L. Y.; Zhang, Y. L.; Wang, H. Y.; Liu, H.; ***Luo, J.***; Xia, H.; Zhao, L.; Chen, Q. D.; Xu, S. P.; Gao, B. R.; Fu, L. M.; Sun, H. B., Hierarchical

self-assembly of CdTe quantum dots into hyperbranched nanobundles: suppression of biexciton Auger recombination. ***Nanoscale*** 2011, 3, 2882-8.

18. Liu, J.; Yang, H.; Zhen, S. G.; Poh, C. K.; Chaurasia, A.; ***Luo, J.***; Wu, X.; Yeow, E. K. L.; Sahoo, N. G.; Lin, J.; Shen, Z., A green approach to the synthesis of high-quality graphene oxide flakes via electrochemical exfoliation of pencil core. ***RSC Advances*** 2013, 3, 11745-11750.
19. Xia, X.; Tu, J.; Zhang, Y.; Chen, J.; Wang, X.; Gu, C.; Guan, C.; ***Luo, J.***; Fan, H. J., Porous Hydroxide Nanosheets on Preformed Nanowires by Electrodeposition: Branched Nanoarrays for Electrochemical Energy Storage. ***Chemistry of Materials*** 2012, 24, 3793-3799.
20. Zhu, J.; Jiang, J.; Sun, Z.; ***Luo, J.***; Fan, Z.; Huang, X.; Zhang, H.; Yu, Ting., 3D Carbon/Cobalt-Nickel Mixed-Oxide Hybrid Nanostructured Arrays for Asymmetric Supercapacitors. ***Small*** published online DOI: 10.1002/smll.201302937.

Chapter 1

Background and Literature Survey

1.1 Energy demands and challenges

The prosperity of the economy and human life depends on the continuous energy supply from various resources, which can be mainly divided into two categories, non-renewable and renewable energies. The non-renewable energies mainly include fossil fuels and original chemicals or minerals, which are the resources that can't renew at a sufficient rate for sustainable economic extraction in meaningful human timeframes. Renewable energies are the energies that are inexhaustible or could replenish at a rate comparable to their utilization, such as solar, wind, geothermal, hydropower and biomass. It is anticipated by the U.S. Energy Information Administration that the total world

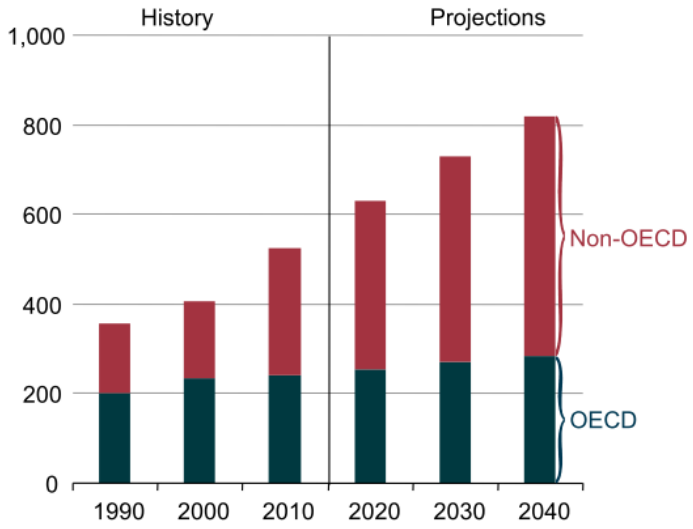

Figure 1.1 *World energy consumption, 1990-2040 (quadrillion Btu). OECD stands for the countries in the Organization for Economic Cooperation and Development.[2]*

energy consumption will rise from 524 quadrillion British thermal units (Btu) in 2010 to 630 Btu in 2020 and to 820 quadrillion Btu in 2040, as shown in Figure 1.1.[2] To meet such a huge energy demand, it is important to explore the new energy resources and increase the efficiencies of the current technologies.

Though the renewable energy and nuclear power play the fastest growing role in energy supply, fossil fuels will continue to supply 80% of the world energy consumption by 2040 as shown in Figure 1.2.[2] The major concern of

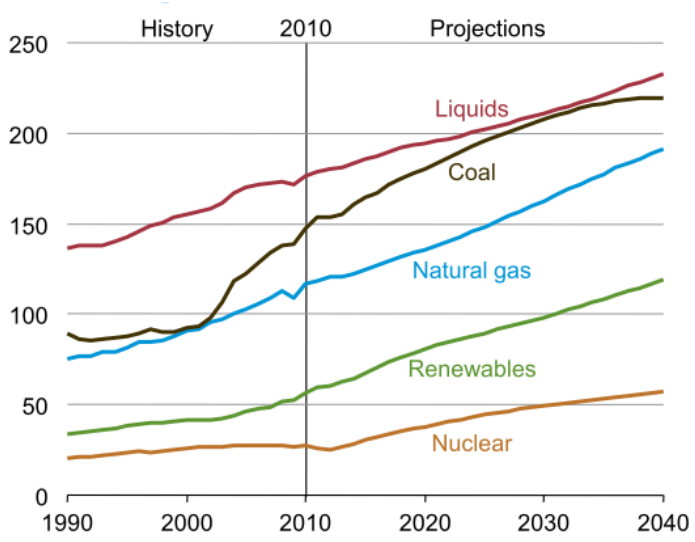

Figure 1.2 *World energy consumption by fuel type, 1990-2040 (quadrillion Btu).* [2]

the fossil fuels is that they are non-renewable energy resources, which means that sooner or later they will run out, and it is just a matter of time. Based on the current proved reserves and consumption rate, it is estimated that oil, coal and gas will be depleted in 35, 107 and 37 years, respectively.[9] Though nuclear energy could reduce the consumption of fossil fuels, it is still a non-renewable energy source and has a lot of other issues, such as the radioactive waste and the terrible risk of accident. The recent Fukushima nuclear disaster prompts the

rethinking of building nuclear power stations all over the world.[10] Besides the finite nature of the fossil fuels, there are other concerns, such as the environmental pollution and global warming. Combustion of the fossil fuels will emit sulfur dioxide, nitrogen oxides, particulate matters, carbon monoxide, carbon dioxide and a number of other pollutants. There is statistic data showing that more than 57% of greenhouse gas emissions on earth come from the combustion of fossil fuels.[11] In addition, the unrest of political situation in the fossil fuel supply countries and the risk of shutdown of the transportation pathway make the energy supply unsecure for most of the countries. The recent nuclear issue in Iran and the Arab Spring revolution blurs the energy supply of fossil fuels in the near future. Thus it is highly demanded to develop renewable energy resources.

Among various renewable energy resources, solar energy is by far the largest exploitable resource, providing more energy in 1 hour to the earth than all of the energy consumed by humans in an entire year.[12] There are mainly three strategies to harvest the solar energy, namely solar water heater, concentrated solar power and photovoltaic.[13] The solar water heater as a supplementary supply of hot water now stands on the roofs of most of the buildings in China and merges into people's daily life. However, its highly dependent property inhibits its large scale utilization for producing electricity. Concentrated solar power and photovoltaic harvest the solar energy and convert it into electricity. Concentrated solar power uses mirrors or lens to concentrate

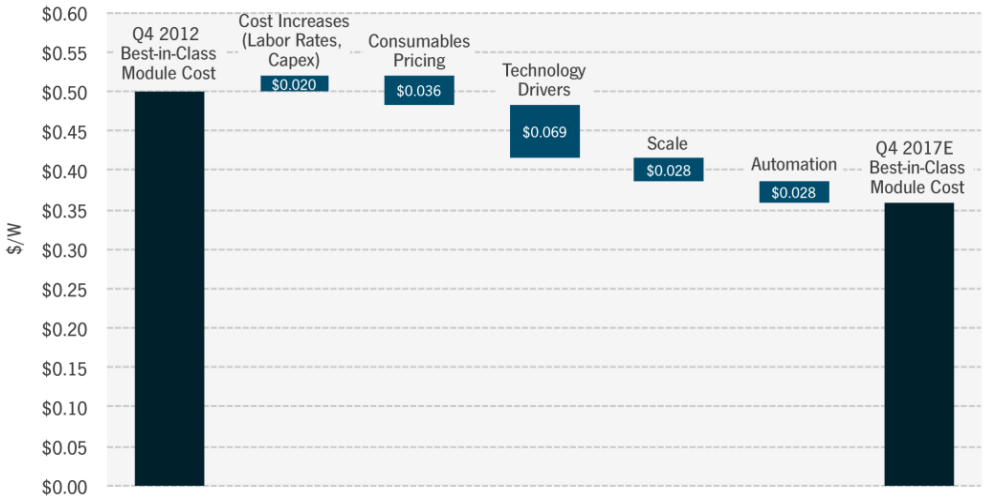

Figure 1.3 *Contribution of key drivers toward all-in module cost reduction, best-in-class China producer, Q4 2012-Q4 2017E.[1]*

the solar energy to heat working fluids which drive an engine to produce electricity. The advantage of the concentrated solar power is that the conventional generators and infrastructures used for thermal electricity can also be used here. Besides, the concentrated solar power systems could introduce a kind of molten salts which could store the heat generated in the daytime and use it to continue generating electricity in the night. The typical example is the Andasol-1 concentrating solar power project in Spain, which has a production capacity of 50 MW and could continue to run 7.5 hours without sunshine.[14] This is one of the promising ways of harvesting the solar energy. However, the high manufacture cost, the stringent requirement of the land and the delicate design and engineering of the systems inhibit the wide spread installation. Photovoltaic, based on the photoelectric effect, is a direct way to covert solar energy into electricity. Though the price of the electricity made from the photovoltaic is far more expensive than the conventional methods, the cost is decreasing as the production is made into large scale. According to the data of

GTM research, the price of the best in class crystalline silicon solar panel made

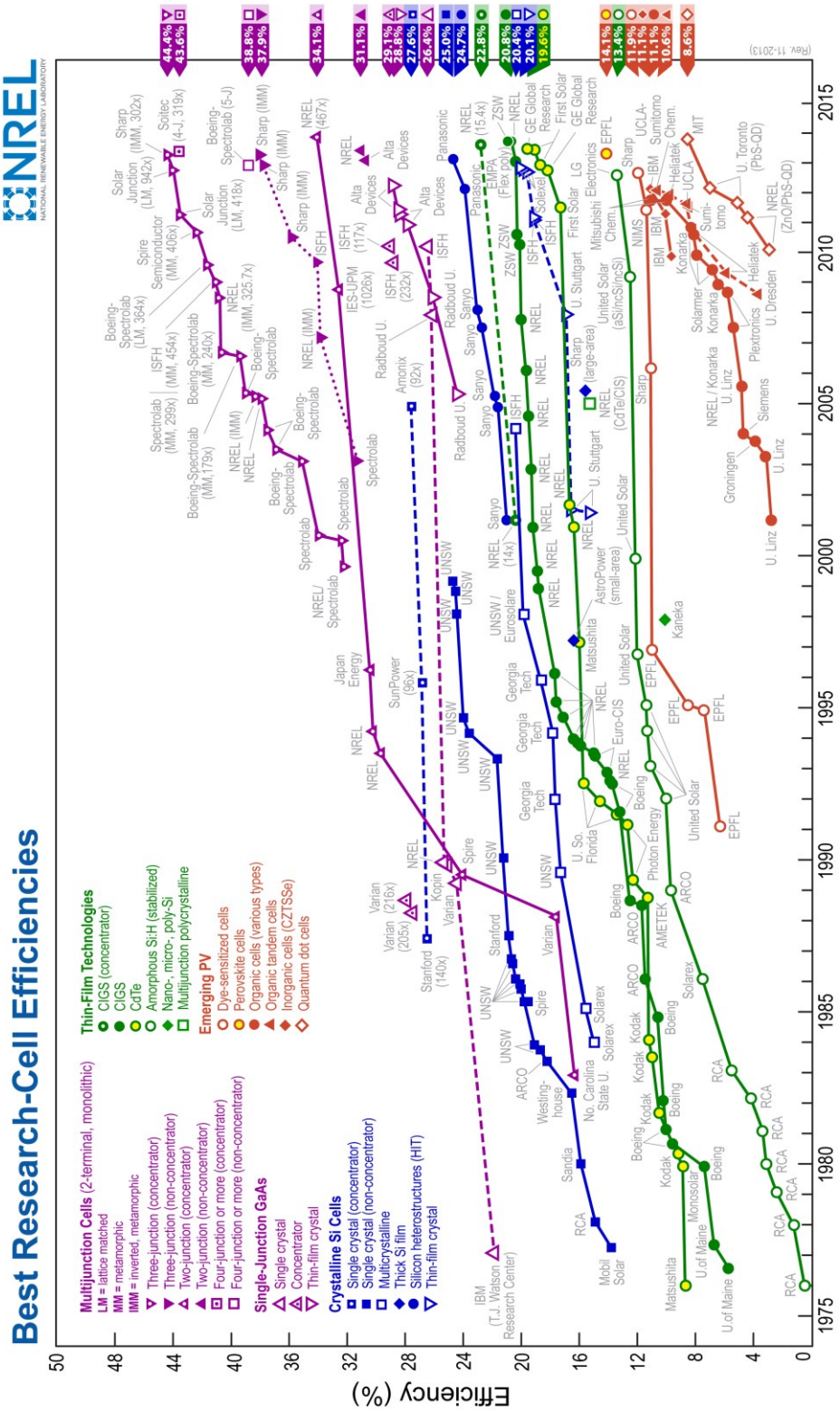

Figure 1.4 *Best Research solar cell efficiencies.[1]*

by Chinese manufactures has reached $0.50/W in 2012, and this will decrease further to 36 Cents per Watt in 2017, Figure 1.3.[1] Now the most efficient Si solar cell has reached an efficiency of 28%, which nearly approaches the Shockley-Queisser limit.[1] Other recent developed solar technologies, such as the thin film CIGS and CdTe solar cells also reach the efficiency of around 20%.[1] And the emerging low cost dye sensitized solar cell and polymer solar cell also overcome the 10% efficiency benchmark for commercialization.[1] Most recently, the provskite sensitized solar cell has reached an efficiency of more than 15%.[15, 16] Figure 1.4 shows a summary of the efficiency development steps for various solar cells. The innovation and development around the globe will make the way of harvesting solar energy much cheaper in the future.

Due to the daily and seasonable variability of the weather conditions, providing a stable and constant energy supply through photovoltaic is a challenge. To overcome the intermittent effect of photovoltaic, it is necessary to develop the energy storage technologies to store the energy produced in the day time and use it in the night. The most straightforward way to store the energy is to use a battery. A small system connecting the solar panels to the battery is enough to power the LED or lighten the road. However, the large scale storage for the solar farm with battery is quite expensive and challenging. The high cost of the battery technologies hinders the grid scale power storage. Scientists are trying to develop next generation battery technology for low cost and high

efficiency storage, such as lithium ion and redox flow batteries.[17-19] The lithium ion batteries now dominate the electronic devices market and keep on growing in the electric vehicles market, and the small scale grid energy storage for the industrial and business parks. As a new concept of energy storage, redox flow battery has the great advantages for large scale grid energy storage. It can have almost unlimited storage capacity just by using larger and larger storage tanks, and it can be left completely discharged for long periods with no ill effects, which offers a great opportunity for the energy storage in solar farm and wind turbine power station.

Another route for the solar energy storage is to directly convert the solar energy into fuel, which could directly replace the currently used gasoline for the public transportation and coal for thermal power generation. In nature, the green plants make photosynthesis every day, harvesting the energy from sunlight and splitting water into hydrogen and oxygen. Then hydrogen is bonded with carbon dioxide to form carbohydrates, such as glucose, which is a kind of chemical fuel storage for the solar energy.[20] If we could mimic the nature, and make a device that could harvest the sunlight and split water into hydrogen and oxygen, we are going to be able to have hydrogen as a fuel, and the only by product after combustion of it is water, which could provide a green and sustainable energy resource for the future. Thus, hydrogen generation from water via sunlight is considered as the “Holy Grail” of solar energy conversion and storage.[21] The brute way to split water with solar energy is to combine

the photovoltaic with an electrolyser. Robert E. Blankenship et. Al. have compared the photosynthetic efficiency in nature with the production of hydrogen by combing the photovoltaic with an electrolyser.[22] They calculated that based on a normal 18% single junction Si solar cell, with 95% solar illumination due to the changing of the solar zenith angle, combined with the 80% efficient modern electrolyser, the solar water spitting efficiency is around 14% (0.18*0.95*0.8). Taking account of the efficiency loss of 20% to 30% due to the voltage mismatch between the photovoltaic and the voltage needed for electrolysis, the current technology for water splitting efficiency is around 10% to 11%. Though the efficiency has met the 10% requirement given by the department of energy of US for the commercialization, the high cost associated with the fabrication of the components and the integration of such a system inhibits the real application. A direct solar water splitting or artificial photosynthesis device involves fewer transduction steps, which could reduce the loss between the photovoltaic and the electrolyser and reduce the system cost. However, it is still a dream in the near term. No systems have been demonstrated to be efficient, low cost, and robust for the real application. To fulfill this green dream, there is still a long way to go.

1.2 PEC cells for hydrogen generation

1.2.1 Thermodynamics of water electrolysis

The PEC cell for hydrogen generation evolves from the water electrolysis cell, which combines the hydrogen evolution at the cathode and oxygen evolution at the anode. The following equation depicts the water decomposition reaction. 1mol of H_2O will release 1 mol of H_2 and 0.5 mol of O_2, and results in a standard Gibbs free energy change of 273 kJ mol^{-1}. The positive value indicates that the water splitting reaction is thermodynamically uphill, thus energy is needed to make the reaction happen. The standard Gibbs free energy corresponds to a reversible potential of 1.23 V, which is the minimum potential needed for water electrolysis.[23, 24]

$$H_2O\ (l) \rightarrow H_2(g) + \frac{1}{2}O_2\ (g)$$

$$\Delta G = +273\ kJ\ mol^{-1}$$

$$E_{rev} = \frac{\Delta G}{nF} = 1.23\ V$$

Due to the low ionic conductivity of water, which is typically less than 0.05 S m^{-1}, electrolysis of pure water is very difficult. Thus, in commercial electrolyser, strong acidic or alkaline solution is used as the electrolyte to increase the conductivity.[24] In alkaline condition, the two half reactions can be written as follows:

Cathode reaction (reduction):

$$4H_2O + 4e^{-1} \rightarrow 2H_2 + 4OH^{-1}$$

$$E^0_{red} = -0.83\ V\ vs.NHE$$

Anode reaction (oxidation):

$$4OH^{-1} + 4h^{+} \rightarrow 2H_2O + O_2$$

$$E^0_{ox} = +0.40\ V\ vs.NHE$$

In acidic condition, the two half reactions can be written as follows:

Cathode reaction (reduction):

$$4H^{+} + 4e^{-1} \rightarrow 2H_2$$

$$E^0_{red} = 0.00\ V\ vs.NHE$$

Anode reaction (oxidation):

$$2H_2O + 4h^{+} \rightarrow 4H^{+} + O_2$$

$$E^0_{ox} = +1.23\ V\ vs.NHE$$

Thermodynamically, a potential of 1.23 V is just enough to drive the water splitting reaction. However, due to multiple effects (polarization effects, kinetics and mass transport) associated with the reactions at both anode and cathode, ohmic loss due to the resistance of the electrolyte and the contact, and the systematic loss, overpotentials are needed to drive the actual reaction. The real operational potential needed can be written as follow:

$$E_{op} = E_{rev} + \eta_a + \eta_c + \eta_\Omega + \eta_{sys}$$

where E_{rev} is the standard reversible potential, η_a and η_c are the anodic and cathodic overpotentials, η_Ω is the ohmic loss, and η_{sys} is the systematic loss. In order to achieve a reasonable H_2 and O_2 generation rate, the potential employed in commercial electrolyser is around 1.6 V to 1.9 V.[25, 26]

1.2.2 Introduction of PEC cell

An electrical water splitting cell uses the electrical energy to split water. In contrast, the PEC cell harvests the energy from sunlight, and generates electron and hole pairs. Electrons will reduce water into hydrogen at the cathode, and holes will oxidize water into oxygen at the anode. The main component of the PEC cell is the semiconductor. The n-type semiconductor acts as photoanode, and the p-type semiconductor acts photocathode. A PEC cell can be either a photoanode system which combines of a photoanode and a metal counter electrode or a photocathode system which combines of a photocathode and a metal counter electrode, or both with the photoanode and photocathode connected together. Figure 1.5 shows the possible PEC configurations under light illumination.

Similar to the conventional solar cell, in order to have a highly efficient PEC cell, there are several steps that need to be optimized. First is the light absorption, in order to harvest more sunlight, the band gap of the semiconductors should be low. However, it should be larger than the standard reversible potential 1.23 V for water splitting. Besides this, there are more

stringent requirements of the band edge positions for the semiconductors. The

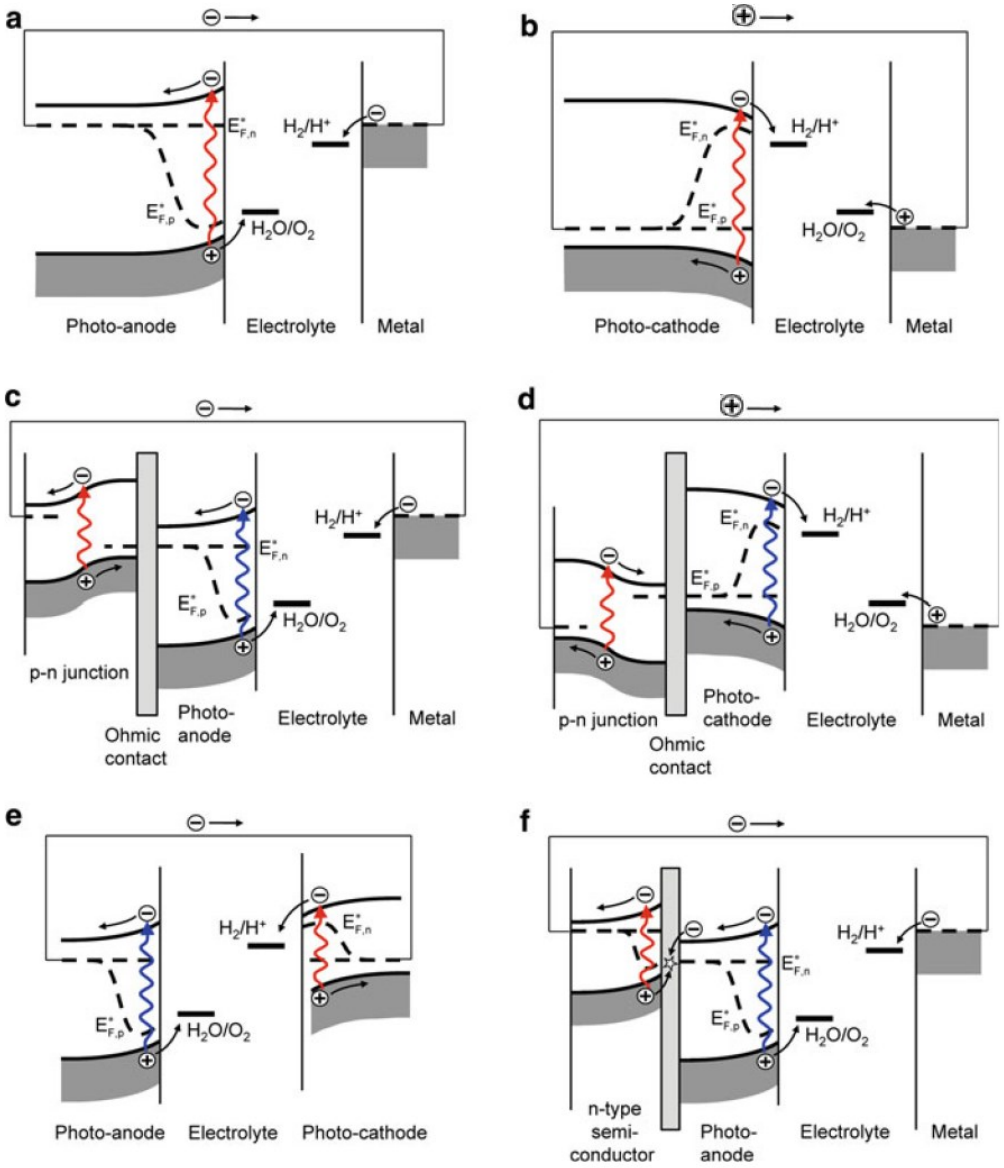

Figure 1.5 *Examples of possible PEC configurations under illumination. Top row: Standard single semiconductor devices based on a photoanode (**a**) or photocathode (**b**) with a metal counter electrode. Middle row: Monolithic devices based on a photoanode (**c**) or photocathode (**d**) biased with an integrated p–n junction. Bottom row: p–n junction photoelectrochemical device (**e**), and an n–n heterojunction PEC device based on a photoanode deposited on top of a second n-type semiconductor that "boosts" the energy of the electrons (**f**)[3]*

conduction band edge should be more negative compared to the water reduction potential, and the valence band edge positions should be more positive than the

water oxidation potential. More precisely, they should be at the qusi-electron and hole levels. Second is the charge separation and transport. Sunlight illumination generates electron and hole pairs inside the semiconductors, and the separation of the electron and hole pairs and the transportation of them to the opposite electrodes become the next priority. In order to have enough time for the separation and transportation, the semiconductor should have long a charge carrier lifetime. Unlike the conventional solid state solar cells, the charges can be separated by the built in electric field and transport to the respect electrodes. PEC cell depends on the rectifying junction between the semiconductor and the electrolyte, which will be discussed in detail in the following paragraph. The charge transport inside the semiconductor mainly depends on the diffusion. Thus the semiconductor should have longer carrier diffusion length. Third is the electrochemical reactions induced by the electrons and holes. Specifically, they are the hydrogen generation at the cathode and the oxygen evolution at the anode. Due to various factors, such as the low activity of the electrode, the poor mass transport of the electrolyte, and the slow charge transport, the electrodes need a higher overpotential to drive the reaction, which will result in a low efficiency. To solve this problem, the electrodes can be coated with catalyst to improve the reaction kinetics. Last but not the least, the semiconductor must be stable in the electrolyte, and this point contains two aspects. On one hand, the semiconductor has to be compatible with the electrolyte. Specifically, the semiconductor should not be soluble in the

electrolyte or react with the electrolyte. On the other hand, upon sunlight illumination, the semiconductor should not decompose. If the oxidation or reduction potential of the semiconductor itself is more favorable compared to the water oxidation and reduction potential respectively, the charge carriers generated by the illumination will decompose the semiconductor itself. Usually, such kind of decomposition is caused by the minority carriers. Thus, for n-type semiconductor, the hole quasi-Fermi level should be more negative than the anodic decomposition potential, and for p-type semiconductor, the electron quasi-Fermi level should be more positive than the cathodic decomposition potential. Overall, the decomposition potentials of the semiconductor should not lie within the bandgap.

1.2.3 Physics of the semiconductor electrolyte interface

According to the quantum mechanics, each single isolated atom has defined atomic orbitals filled with electrons of different energy levels. When the atoms are brought together forming molecules, the orbitals of different atoms will interact with each other and form molecular orbitals. As the number of the atoms increasing, the molecule orbitals become larger and larger and the energy levels become finer and finer. Finally, when large quantities of atoms form into a solid, the energy levels of the solid will be so close that they can be considered as a continuum which can be called as a band.[27] The highest occupied energy band is valence band, and the lowest unoccupied band is

conduction band. Correspondingly, the upper edge of the valence band is called valence band edge (E_{VB}), and the lower edge of the conduction band is called conduction band edge (E_{CB}). And their energy difference is called band gap (E_{BG}). The semiconductor can be thermally or photochemically excited, with the electrons jumped to the conduction band, leaving the holes in the valence band.

The electrochemical potential of the electrons in semiconductor can be described by the Fermi level (E_F), which is defined as the energy level at which the probability of occupation by the electrons is 50%. The Fermi level in semiconductor physics is usually referenced to the vacuum level. The Fermi level energy can be calculated by the following equation, [24]

$$E_F = \frac{1}{2}(E_{VB} + E_{CB}) + \frac{1}{2}(kTln\frac{N_{VB}^*}{N_{CB}^*})$$

where k is the Boltzmann constant, T is temperature, N_{VB}^* and N_{CB}^* are the density of energy states in the valence band and conduction band respectively. For intrinsic semiconductor, the Fermi level lies in the middle of the band gap, and for highly doped n-type and p-type semiconductors the Fermi levels lie just below the conduction band or above the valence band respectively. In electrochemistry, the electrochemical potential of the electrons in electrolyte is called redox potential, which is usually with reference to the standard hydrogen electrode (SHE).[28] The redox potential is defined by the concentrations of the

oxidized and reduced species in the electrolyte, which can be calculated by the following equation,

$$E_{F,redox} = E^0_{redox} + kTln(\frac{C_{ox}}{C_{red}})$$

where k is the Boltzmann constant, T is temperature, and C_{ox} and C_{red} are the concentrations of the oxidized and reduced species in the electrolyte, respectively. When semiconductor is immersed into the electrolyte, the semiconductor electrolyte interface will be formed. In order to explain the charge transfer process across the interface and reconcile the different terminologies between physicist and chemists, the redox potential of the electrolyte can be considered as the Fermi level of the electrolyte. [28, 29]

For an n-type semiconductor, usually its Fermi level is higher than the electrolyte. Thus, when an n-type semiconductor is immersed in electrolyte, free electrons in the semiconductor will flow to the solid electrolyte interface, leaving the positive charges behind and negative charges in solution. The negative charges in the electrolyte will induce a thin Helmholtz layer, usually in the range of a few nm. In contrast, the positive charges in the semiconductor not only exist on the surface but also spread to the bulk of the solid typically for several μm, and the region is called space charge layer.[30] The inhomogeneous charge distribution in the semiconductor will induce an inhomogeneous electric field across the semiconductor electrolyte interface, which can be revealed by the band bending. For the n-type semiconductor

electrolyte interface, when the semiconductor is photoexcited, majority electrons will migrate to the semiconductor and minority holes will move to the electrolyte to drive the water oxidation reaction. Due to this, the PEC cells are minority carrier device.

Under illumination, excess electron and hole pairs will be generated, new

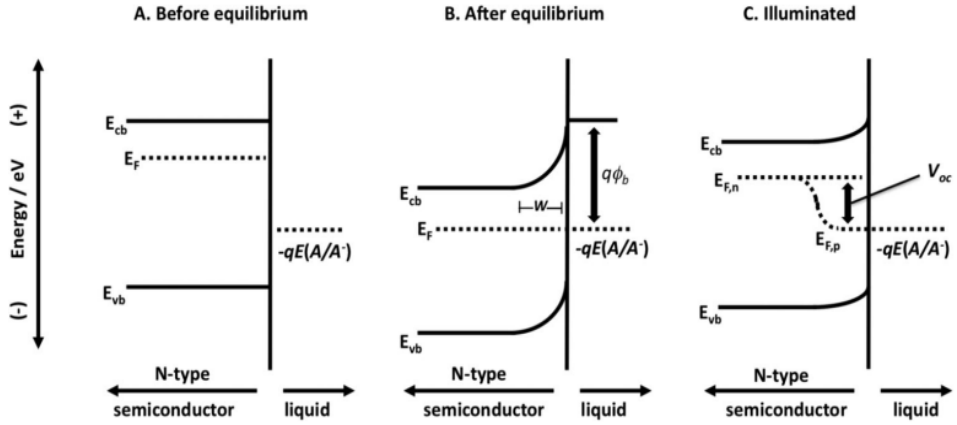

Figure 1.6 *The band energetics of a semiconductor/liquid contact are shown in three cases: (A) before equilibration between the two phases; (B) after equilibration, but in the dark; and (C) in quasi-static equilibrium under steady state illumination. In panel B, $q\varphi_b$ is known as the barrier height, and its magnitude determines the theoretical maximum energy that can be extracted from a separated electron-hole pair at the semiconductor/liquid junction. In panel C, where steady-state illumination yields nonequilibrium electron and hole populations, $E_{F,n}$ is the electron quasi-Fermi level and $E_{F,p}$ is the hole quasi-Fermi level. The voltage generated by the junction under illumination is given by the difference between $E_{F,n}$ and - qE(A/A$^-$).[8]*

equilibrium will be reached. For n-type semiconductor, electrons are majority carries which are barely changed by the illumination. The concentration of the minority holes will increase significantly. At this time, the Fermi level of the semiconductor cannot be described by a single level. Instead, it is in a dynamic state, which can be considered as two levels now, the electron quasi-Fermi-level and the hole quasi-Fermi-level respectively. The split of the

Fermi level is mainly due to the shift of the hole quasi-Fermi-level. The energy separation between the two levels determines the energy that can be extracted, which is correlated to the open circuit voltage. In order to split water without any given bias, the electron quasi-Fermi-level must be sufficiently higher than the hydrogen evolution potential and the hole quasi-Fermi-level must be sufficiently lower than the water oxidation potential at the same time. This is the stringent way to describe the requirement to split water rather than the band gap of the semiconductor should straddle the water splitting potentials.

The band energetics of the semiconductor electrolyte interface in different conditions can be summarized in Figure 1.6. [8]

1.2.4 Flat band potential

Except the light illumination, applying external bias potential will also change the band bending condition of the semiconductor electrolyte interface. At certain potential, there is no band bending for the semiconductor, and this potential is called Flat band potential.[28] For an n-type semiconductor, giving a bias more positive than the flat band potential will cause a deep depletion in the semiconductor, and the reverse potential will cause the accumulation in the semiconductor.

At the flat band potential, there is no current even under illumination, as the charge transfer process depends on the electric field caused by the depletion or inversion. In order to know the capability of the semiconductor for water

splitting, it is important to test its flat band potential.[31] There are mainly three different ways to test it.[31, 32] The first method is to measure the open circuit potential at different illumination intensity; the second method is to measure the onset potential of the photocurrent; and the third one is to measure the capacitance of the space charge area and use the Mott-Schottky equation to determine the flat band potential. The easiest method is to measure the onset potential of the photocurrent, which is the potential where photocurrent starts. In specific, it is the potential where the dark current and the photocurrent intercept. In the illuminated open circuit potential method, the light illumination will generate electron and hole pairs, for the n-type semiconductor, the holes will move to the electrolyte, and electrons will be left behind and generate an opposing electric field. Under sufficient illumination condition, the band of the semiconductor will become flat, and the open circuit potential at this time reaches maximum and approaches flat band potential. Thus, measuring the open circuit potential at different light illumination condition will give a curve, and the plateau of the curve can be considered as the flat band potential. The most complicated way to measure the flat band potential is to use the Mott-Schottky relationship, which is an electrochemical impedance spectroscopy (EIS) technique. [33]The Mott-Schottky equation is as follow,[33]

$$\frac{1}{C_{sc}^2} = \frac{2}{\varepsilon\varepsilon_0 A^2 e N_D}(V - V_{fb} - \frac{kT}{e})$$

where C_{sc} is the space charge layer capacitance, ε is the dielectric constant of the semiconductor, ε_0 is the permittivity of the free space, A is the interfacial

area, N_D is the donor density of the semiconductor, V is the applied potential, V_{fb} is the flat band potential, k is Boltzmann constant, and T is the temperature. For the capacitance, there are two here. One is the space charge layer capacitance, and the other is the double layer capacitance. These two capacitances are in series. As the latter one is much smaller than the former one, the contribution to the total capacitance is nearly negligible. According to the Mott-Shcottky equation, the plot of $1/C_{sc}^2$ versus electrode potential (V) will be linear, and the intercept at zero potential is $V_{fb} + kT/e$, thus the flat band potential can be derived.

1.2.5 Efficiency of PEC cell for water splitting

The efficiency of the water splitting cell is determined by the amount of the chemical energy stored in hydrogen over the light energy shining on the device.[3, 31] Each step in the water splitting process has an impact on the efficiency. There are mainly three steps that determine the efficiency. The first step is the light absorption by the semiconductor, the second step is the conversion of the photons to electric charges, and the third step is the electrochemical reactions for water splitting induced by the charges. Thus, the overall efficiency can be written as

$$\eta = \eta_{abs} \times \eta_{con} \times \eta_{rea}$$

where η is the overall efficiency, η_{abs} is the absorption efficiency, η_{con} is the exiton generation efficiency, and η_{rea} is the electrochemical reaction

efficiency. However, experimentally, it is hard to separate the three steps and measure the individual efficiency. Assuming all the electrons and holes generated by the illumination are used to drive the water splitting reaction, which means η_{rea} is 100%, and two electrons are correlated with one H_2 molecule, the Gibbs free energy stored in H_2 per area can be written as $1.23 \times J$, J is the photocurrent density. The total conversion efficiency can be written as

$$\eta = \frac{1.23 \times J}{P}$$

where P is the light illumination intensity. In all the known materials, only very few semiconductors with large band gaps can have unassisted water splitting, and for the rest it is necessary to apply an external bias to drive the water splitting reaction. To calculate the efficiency at this condition, the energy contributed by the external bias has to be reduced, and the efficiency can be written as

$$\eta = \frac{(1.23 - E_{bias}) \times J}{P}$$

where E_{bias} is the external bias applied. In the characterization of the water splitting device, the PEC measurements are usually done in three electrode configuration. However, the bias in the equation above is only applied to the two electrode configuration, which is the bias between the working and counter electrode.[31]

The incident photon to current efficiency (IPCE) is another important parameter to characterize the efficiency. It represents the efficiency of the first two processes of light absorption and charge conversion together, and it is also called as quantum efficiency. It is a function of wavelength, and can be calculated by measuring the photocurrent under a particular wavelength of light illumination with a known intensity.[3, 31] The equation is

$$IPCE(\lambda) = \frac{hc}{e}\left(\frac{J}{P(\lambda)\cdot\lambda}\right) = 1024\left(\frac{J}{P(\lambda)\cdot\lambda}\right)$$

where J is the photocurrent density, $P(\lambda)$ is the power density of the light at wavelength λ. If the IPCE at all wavelength range is known, the total photocurrent can be calculated by integrating the IPCE with the power density of the illumination light. Another parameter to characterize the quantum efficiency is the absorbed photon to current efficiency (APCE), which depicts the efficiency in the second step process. The APCE reduces the loss of reflection and transmission for the IPCE, which can be written as follow,

$$APCE(\lambda) = \frac{IPCE(\lambda)}{A} = \frac{IPCE(\lambda)}{1-R-T}$$

where A is the absorption of the semiconductor, R is the reflection and T is the transmission. Note that A is the absorption, which is different form the commonly used absorbance a tested by the UV-visible spectroscopy. The relation between the two is $A = 1 - 10^{-a}$.

Photocurrent is the indirect way to characterize efficiency, but it is the most frequently used parameter in water splitting device. Assuming Faradic efficiency is 100%, the photocurrent can be directly correlated with the amount of hydrogen generated. For a given semiconductor, assuming all the photons exceeding the band gap can be absorbed and used to generate the electron and hole pairs, and all these pairs are converted to the photocurrent, the maximum photocurrent attainable by the semiconductor can be calculated. Figure 1.7

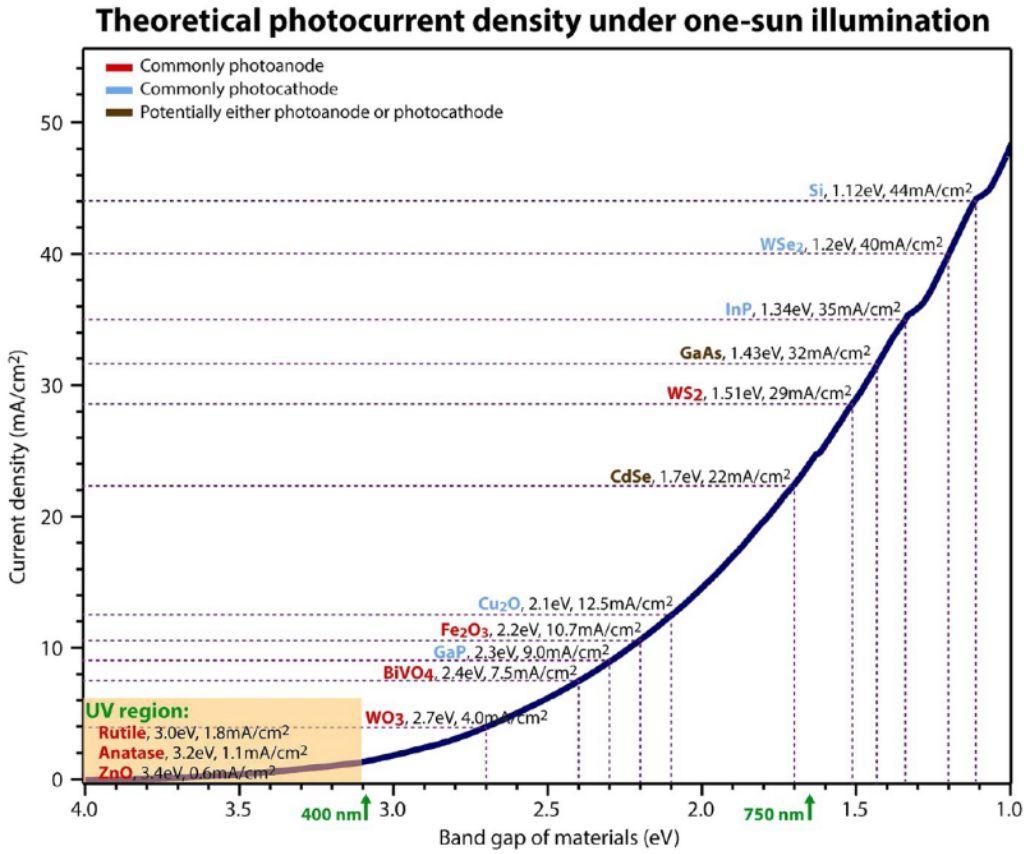

Figure 1.7 *Theoretical photocurrent densities for semiconductors under one-sun illumination. The blue curve is the integrated photon flux at different cutoff energies, based on the AM1.5G solar spectrum (ASTM G173-03 reference). The theoretical photocurrent is calculated assuming that all incident photons above the semiconductor band gap contribute to the photocurrent. Several of the semiconductors used in solar-to-fuel conversion are also listed, along with their reported band gaps in bulk phases. The arrows at the bottom indicate the regions of ultraviolet (UV) (below 400nm), visible (400 − 750 nm), and infrared (IR) spectra.[6]*

shows the theoretical photocurrent densities of the semiconductors for a single junction water splitting device as a function of the wavelength and band gap under one-sun illumination, and the photocurrent of some commonly studied electrode is directly pointed out. [6]

In order to harvest more sunlight, two or more kinds of materials can be combined together to work as a multi-junction cell or tandem cell. [7]In this kind of cell, the sunlight passes through one material first and gets absorbed partially, and the filtered light will be absorbed by the second material. Thus, a larger part of the sunlight can be harvested. The photovoltage will be sum of the two cells, and the current will be equal to the smaller one of the two. In terms of the device configuration, the most direct way is to combine the photoanode and photocathode together. Combining the materials together to work as just photoanode or photocathode is also common. Though the photocurrent of the tandem cell is lower than that of the single junction cell, the overall efficiency can be significantly higher. Theoretically, the two junction configuration could extend the solar to hydrogen conversion efficiency to 30%.[7, 34] Based on the tandem cell with two absorbers, assuming that each semiconductor absorbs all photons with energy $hv > E_g$ and transmits all photons with energy $hv < E_g$ without reflection or scattering losses. The maximum expected η_{STH} as a function of the chosen band gap energies, E_{g1} and E_{g2}, can be predicted considering the distribution of photons in the standard solar illumination (AM 1.5G 1000 Wm^{-2}) as shown in Figure 1.8.[7]

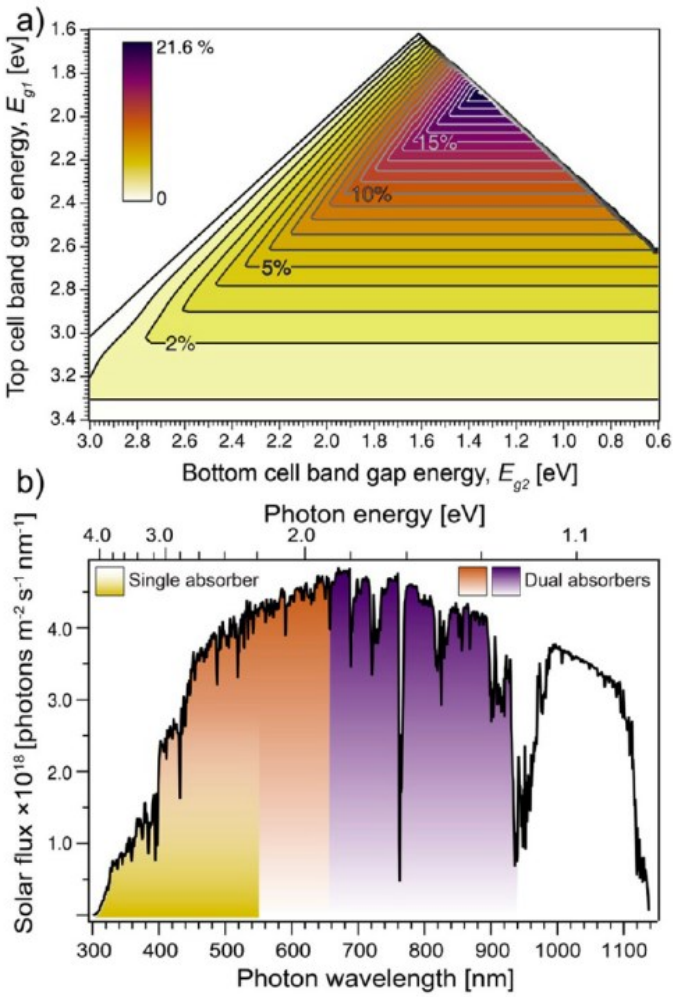

Figure 1.8 (a) *Contour plot (thick gray lines) showing the maximum predicted* η_{STH} *with AM 1.5G incident radiation (1000 W m*$^{-2}$*) and a total loss,* U_{loss}*, set at 2.0 eV as it depends on the chosen semiconductor band gap energies,* $E_{g,i}$*, i = 1, 2 (with* $E_{g1} > E_{g2}$*).* ***(b)*** *The benefits of the tandem cell approach are shown through the AM 1.5G solar photon flux as a function of wavelength and photon energy. The shaded area of the spectrum represents the photos that could be harvested using a single semiconductor absorber (yellow) and a dual absorber tandem approach (light brown and purple).[7]*

1.2.6 PEC measurements

In order to measure the PEC performance of the electrodes, the first thing to do is to build a suitable PEC cell setup. The most common setup is the three electrodes cell configuration, with a compartment to store the electrolyte and three electrodes for test. Usually, the samples serve as the working electrode. In

order to transport current, a suitable counter electrode is needed. Besides, a reference electrode is needed to accurately adjust the potential of the working electrode. Sometimes, it is required to process the samples before the test.[31] For example, for the samples without a good contact, wire bonding is needed to increase the conductivity. Copper wire can be used, and silver paste could be utilized as the glue. In order not to shunt the circuit from the active material, the exposed conductive part needs passivation. The non-transparent epoxy or black nail polish could be a good choice, which can not only passivate the material but also help to define the active area of the sample.

The choice of the counter electrodes depends on the samples that need to be tested. For the n-type semiconductor, Pt foil or mesh can be used as the counter electrode, as Pt is a good catalyst for hydrogen evolution. With same principle, the counter electrode for the p-type electrode should be a good oxygen evolution catalyst. Anyhow, in order not to limit the reaction kinetics of the working electrode, the size of the counter electrode is usually double or more times of the working electrode.

Reference electrode could control the potential of the working electrode on an electrochemical scale by using well defined redox systems. There are various kinds of reference electrodes, and the choice of suitable reference electrode depends on the electrolyte used. The normal hydrogen electrode is a standard for the electrochemical potential, and is considered as the zero potential. However, it is hard to construct in real experiment condition, which needs a

platinum electrode surrounded with the solution containing1M H^+ ions and H_2 gas bubble through at 1 atm pressure. As the Pt/electrolyte interface is irreproducible, a theoretical condition is assumed to define the zero potential as the standard hydrogen electrode potential. In real experiments, the most commonly used electrodes are saturated calomel electrode (SCE) and saturated Ag/AgCl electrode, and they can be used in wide pH ranges. For long time experiments in strong H_2SO_4 acid or alkaline solutions, $Ag/AgSO_4$ and Hg/HgO reference electrodes can be used respectively.

As the electrochemical potentials of the water splitting reactions and the band edge positions of the semiconductor change with the pH values, thus it is necessary to define an electrode whose potential doesn't change with the pH values, and the reversible hydrogen electrode (RHE) fulfills this goal. As a result, it is more convenient to use than SHE. To compare the PEC performance of different electrodes, it is necessary to convert the electrochemical potentials measured with different reference electrodes to RHE. For the most frequently used Ag/AgCl electrode, it can be converted by the following equation,

$$E_{RHE} = E_{Ag/AgCl} + E^0_{Ag/AgCl} + 0.059 \times pH$$

where $E_{Ag/AgCl}$ is the potential measured with respect to the Ag/AgCl electrode, $E^0_{Ag/AgCl}$ is the potential of Ag/AgCl electrode referred to SHE. For saturated KCl filled Ag/AgCl, it is 0.1976 V.

The current-potential profile is one of the most important characteristics of the PEC electrodes, and it can be described by the Gartner model.[3, 35] Gartner uses an equation to derive the photocurrent in a semiconductor under external bias,

$$j_G = j_0 + e\emptyset(1 - \frac{e^{-\alpha W}}{1 + \alpha L_p})$$

j_0 is the saturation current density, $\emptyset$ is the incident light flux, α is the absorption coefficient, W is the depletion layer width, and L_p is the hole diffusion length.

1.2.7 Recent advances in using TiO_2 for water splitting

Ever since Fujishima and Honda had demonstrated the photoelectrolysis of water with TiO_2,[36] TiO_2 has received a wide attention in water splitting, photocatalysis, and solar cell.[8, 37, 38] Though TiO_2 is cheap, nontoxic and has high photoactivity, its large bandgap limits the absorption in the UV range, and results in low efficiency. In order to improve its performance for water splitting, extensive research has been done in the past several decades, which can be summarized into three categories as following.

The first approach is to dope or introduce deficiencies into TiO_2 to enhance the visible light absorption. In 1994, Choi et al had systematically studied the doping of TiO_2 with different metal ions, and found that doping could change the photoactivity and charge transfer rate of TiO_2.[39] Later on,

Anpo et al found that doping of TiO_2 with the Cr ions could broaden the absorption range of TiO_2 toward the visible part, and the extent can be tuned by varying the concentration of the dopants.[40] Since then, various metal ions doped TiO_2 have been studied.[41-45] The mechanism of visible light response by the cations doping can be explained by the defect states created in the band gap of TiO_2.[41] Recently, Liu et al have developed the solution method to

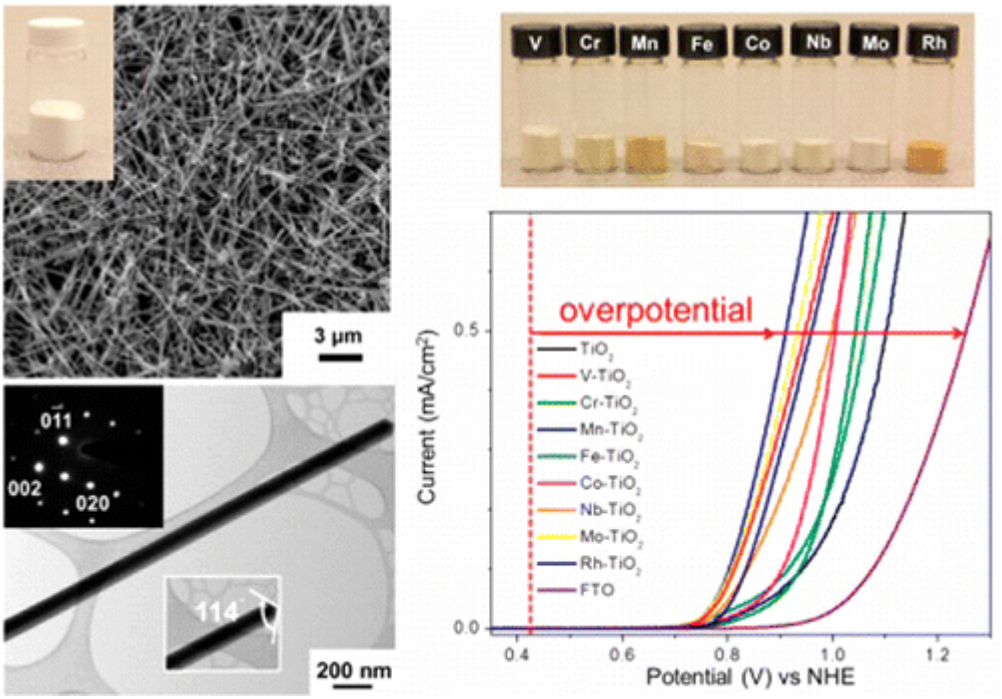

Figure 1.9 *Transition metal doped TiO_2 nanowires with controllable overpotential.[5]*

synthesize transition metal doped TiO_2 nanowires with controllable overpotentials, as shown in Figure 1.9. [5] Even the light response range is broadened by the transition metal doping, there are no great improvements achieved for the performance of the samples due to the recombination centers and reduced carrier mobility. Most detrimentally, some cation doping will shift the conduction band edge of TiO_2 downward, making it less sufficient for water

reduction reaction.[46] Thus, in terms of the performance in water splitting, there is no obvious enhancement through cation doping and sometime even worse. Besides cation doping, anion doping can also improve the visible light response of TiO_2. Early in 1986, Sato had reported the NOx doped TiO_2.[47] However, the anion doping has only received a wide attention since the work reported by Asahi et al.[48] They had calculated the doping effect of various anions for TiO_2, (such as C, N, F, P, and S) and concluded that N was the most effective dopant. By sputtering TiO_2 in the N_2 and Ar gas mixture followed by

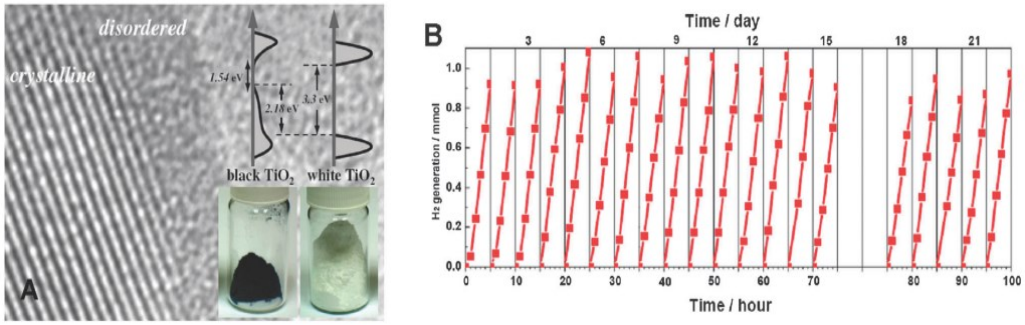

Figure 1.10 *(A) Schematic illustration of the density of states of disorder-engineered TiO_2 nanocrystals as compared to that of unmodified TiO_2 nanocrystals. The background is part of a disorder-engineered TiO_2 nanocrystal. Photos of disorder-engineered (black) and unmodified (white) TiO_2 nanocrystals are also shown. (B) Cycling measurements of hydrogen gas generation through direct photocatalytic water splitting with disorder-engineered black TiO_2 nanocrystals under simulated solar light.[49, 50]*

annealing at 550°C in N_2 gas, the authors had improved the activity of TiO_2 in photocatalyst application. Later on, Khan et al had developed C modified TiO_2 by the flame method, and demonstrated its superiority over pure TiO_2 in water splitting.[51] Not only the external cations or anions can cause doping, the

oxygen deficiency in the TiO_2 can create Ti^{3+} sites, which can be called as self-doping.[52] TiO_2 can be reduced by annealing at high temperature in vacuum or hydrogen atmosphere, this reduction is usually accompanied with the broadening of the absorption spectrum.[53] The most common color of the TiO_2 with oxygen vacancy is blue.[54] Recently, black TiO_2 has also been developed by surface hydrogenation, as shown in Figure 1.10. [50]

The hydrogenation will cause disorder on the surface of TiO_2 and introduce the defect states inside the bandgap, which are continuum. The black TiO_2 has demonstrated a great improvement in photocatalysis compared to the pristine white samples. For the efforts by doping, no matter whether cations or inions are used, the dopant concentration is always a very important parameter that needs to be well controlled. Insufficient doping will not be able to have effect in performance, while excess doping will cause a high rate of recombination.[46] In order not to increase the recombination rate during doping, a co-doping method has been proposed.[46] By introducing the cations as donors and anions as acceptors at the same time, the recombination centers by doping can be reduced. Theoretically, various combinations have been proposed.[46, 55, 56] However, they are difficult to realize due to the limitations of the experiment conditions and methods. Recently, Zheng et al had employed a new flame method to co-dope TiO_2 with W and C.[57] Due to the reduced charge recombination, co-doped samples exhibit superior performance compared to the mono-doped ones. Though doping could improve the performance of TiO_2 to

some extent, the improvement could never be significant or revolutionary due to the defects induced by the doping. Thus, it is highly demanded to search for other methods to improve the performance.

The second approach is to make TiO_2 nanostructures. Compared to the bulk electrodes, nanostuctures have many advantages, which can address the limitation of the materials.[3, 49, 58, 59] The most significant effect of nanostructure is the increment of the surface area. As water splitting reactions take place on the surface, more surface area will create more reaction sites and improve the charge transfer kinetics at the interface. The second advantage is the shortening of the charge carrier transport length. For the bulk electrode, the charge carriers have to travel across the whole electrode to reach the surface to induce water splitting reactions. In contrast, for the nanowire electrode, the carriers only need to transport the length of half the diameter of the nanowire to reach the surface. The third advantage is the enhancement of the light absorption. In order to harvest more light, the electrode needs to be thick enough to the reach the absorption depth. As nanostructures could promote light scattering on the electrode surface and increase the light transport path inside the electrode, the strong light absorption and efficient charge transfer can be achieved at the same time. Furthermore, since the different surfaces of the material may exhibit different activities toward the water splitting reactions, precise nanostructure engineering could expose more active surfaces and increase the reaction rates. Due to the advantages discussed above, various TiO_2

nanostructures have been extensively studied and successfully synthesized.[60-64] The most common type is nanoparticles, because they have a high surface area. Another attraction of making nanoparticles is the quantum confinement effect. When the charge carriers are confined to a volume that is less than their De Broglie wavelength, quantum confinement effect will be induced, and the band gap of the material will be changed.[65] However, this effect is very difficult to induce for TiO_2, mainly due to the large electron and hole masses.[66, 67] Theoretical calculations prove that different facets of TiO_2 have different reactivity.[68-73] For example, due to the high densities of under-coordinated Ti atoms and very large Ti–O–Ti bond angles at the surface, (001) facet is predicted to be more active than the thermodynamically stable (101) facet. Synthesizing the TiO_2 nanocrystals with high percentage of (001) facets becomes a fever at a time, and the representing work is done by Yang et al.[74-76] By using the hydrofluoric acid as a morphology controlling agent, they have synthesized uniform anatase TiO_2 single crystals with 47% of (001) facets. Though the TiO_2 nanoparticles are very efficient in photocatalytic water splitting when suspended in the solution, the efficiency is nearly negligible when casted as a film. Directly grown TiO_2 nanostructures on conductive substrates is favorable in PEC water splitting. Grimes et al had demonstrated the TiO_2 nanotubes on Ti foil for water splitting by electrochemical anodization.[77] Due to the efficient charge carrier transport, they have achieved a high efficiency. Later on TiO_2 nanorod arrays directly grown on

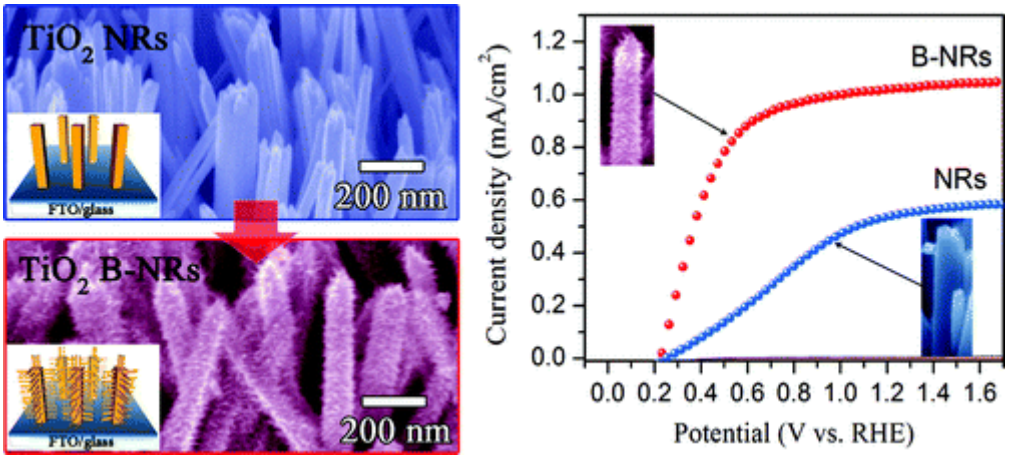

Figure 1.11 *Branched TiO_2 nanostructures for water splitting.[4]*

FTO have been developed.[61, 64] And Hwang et al have studied the length and surface passivation effects by ALD for water splitting in detail.[78] Though TiO_2 nanorod film shows a favorable charge transport pathway compared to the nanoparticle flim, the surface area is greatly reduced. Thus in the conventional photocatalyst and solar cell application, TiO_2 nanoparticles still outperform the TiO_2 nanorods.[64, 79] In order to increase the surface area, the tree-like branched structure is proposed.[80, 81] Zheng et al have demonstrated enhanced water splitting by using the branched TiO_2 nanostructure and achieved greatly improved performance compared to pristine TiO_2 nanorods, Figure 1.11.[4] Nanostructured TiO_2 is indeed more active compared to bulk TiO_2 due to the improved charge transport. However, even the charge transport is 100% efficient, the maximum photocurrent of anatase and rutile TiO_2 can reach is 1.1 mA/cm^2 and 1.8 mA/cm^2 respectively under AM 1.5 G solar illumination, as nanostructure can't make TiO_2 absorb more light beyond its own bandgap.

The band gap limitation of the TiO_2 makes it inefficient for water splitting. By making composites or heterostructures with the other materials, this limitation can be complemented, and this strategy can be counted as the third approach to improve the performance of TiO_2. TiO_2 has three different phases in nature, anatase, rutile and brookite.[82] Due to different crystal structures, their electronic structure, carrier diffusion length and redox potentials are different. Thus they have different performance towards water splitting. Anatase is proved to be the most efficient among the three, and some claim that it is mainly due to the higher conduction band edge, which could have a higher overpotential for hydrogen reduction.[83, 84] To make composite or hetero-structures, the first thing can be started with is using different phases of TiO_2. In fact, the mixture of any two of the three did show higher efficiency than the individual.[85-89] The famous Degussa P25 TiO_2 nanoparticles are composed of anatase and rutile together, which have a wide application in photocatalysis and solar cell.[90] And higher efficiency of water splitting has been proved by using anatase and rutile junction.[76] Except forming a homo-junction by mixing different phases, there are several other ways to improve the performance of TiO_2 by making composite nanostuctures, such as decorating TiO_2 with noble metals, organic dyes and short band gap semiconductors.[37, 38, 84, 91, 92] There is no consensus on the role of noble metals yet. In the early stage, it was proposed that the electron transfer from TiO_2 to the metal enhanced the charge separation. As the metal usually have a

lower Fermi level compared to TiO_2, so when they are deposited onto the TiO_2 surface, the electrons generated from TiO_2 will transfer to the metal, resulting in enhanced the charge carrier separation.[37] Several reports have supported this mechanism.[93-97] Later on, researchers proposed that the enhancement is actually through the plasma effect.[98, 99] Regarding this point, there are still two different views. Some claim that the light excitation will cause surface plasma in the noble metal, and the decay of these plasmas will create electron and hole pairs inside the metal like the semiconductors. Most of the excited electrons in the metals are hot electrons, which are energetic enough to transfer to TiO_2. The noble metals here serve as the photosensitizer, which is similar to the sensitization by using the organic dye or the semiconductors discussed later.[99, 100] While, the others claim that this is impossible, as the electron hole pairs is not realistic in metals due to the lack of highest occupied molecular orbital-lowest unoccupied molecular orbital (HOMO-LUMO) energy separation or analogous valence band-conduction band energy separation in a plasmon excitation, and the band alignment between the metal and TiO_2 makes it energetically unfavorable for the electron transfer to TiO_2.[98] And they claim that the enhancement is due to the enhancement of the local electric field near the TiO_2 surface by the plasmon resonance rather than electron transfer.[98] For the sensitization method, both the functions of the organic dye and short band gap semiconductor on TiO_2 are to enhance the light absorption, [101, 102] and the idea for water splitting cell is evolved from the conventional dye sensitized

solar cell and quantum dot sensitized solar cell. The difference between water splitting cell and the sensitized solar cell is that there are no regenerative agents in the electrolyte, thus the water splitting cell is also called as photosynthetic cell. Youngblood et al have demonstrated the overall water splitting by using the organic dye $[Ru(bpy)_3]^{2+}$ as the sensitizer capped by the $IrO_2 \cdot nH_2O$ particles, which function as the water oxidation catalyst, as shown in Figure 1.12.[103]

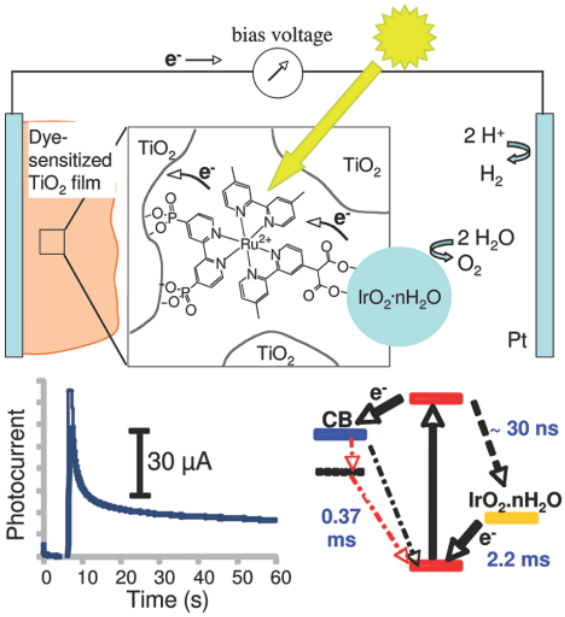

Figure 1.12 *(top) Schematic diagram of a water-splitting dye-sensitized solar cell. The inset illustrates a sensitizer-capped $IrO_2 \cdot nH_2O$ catalyst particle in the mesopores of the TiO_2 electrode film. (bottom left) Current transient obtained under visible light illumination. (bottom right) Energy level diagram showing the rates of forward and back electron transfer from and to the sensitizer molecule.[8]*

However, most of the dyes degrade quickly under water oxidation, thus this concept faces a great challenge in real application.[91] Alternatively, the utilization of short band gap semiconductors as the sensitizers has been proposed, as they are relatively more stable, and it is also the focus of this thesis. Sensitization of TiO_2 with short band gap semiconductors has been extensively

studies for quantum dots sensitized solar cell in the past decade. [102, 104] In However, less attention has been devoted to solar fuel generation. As the concepts and ideas for quantum dots sensitized solar cell can also be used here, a brief overview is provided here. In the initial stage, researchers have been focused on the developing the sensitization method, mainly pre-synthesized route or direct growth.[92, 105] Per-synthesis method provides great control of the size and optical properties of the quantum dots. However, the loading of the quantum dots is low, which results in low efficiency. Thus, various other methods have been developed, such as chemical bath deposition, [106, 107] successive ionic layer adsorption and reaction (SILAR),[108-110] electrochemical deposition,[111] chemical vapour deposition[112] and electrophoretic deposition.[113] The most common TiO_2 scaffold used for sensitization is TiO_2 particles as the concept is evolved from dye sensitized solar cell. Unlike dye molecules, the size of semiconductor quantum dots is much larger than, resulting in much lower pore filling ability into the TiO_2 particle film. Thus, other structured TiO_2 film with more open area have been developed and used. One-dimensional nanostructures such as nanowires and nanotubes offer superior electron transport path ways and improved light scattering have been used. However, they suffer from very low surface area, resulting in low photoelectrochemical performance.[114, 115] Three-dimensional inverse opal (IO) nanostructures, with larger surface area

than TiO_2 nanowries and nanotubes and higher level of porosity than TiO_2 particle film have been proposed to enhance the performance. [116-124]

Though advancement of the sensitization of TiO_2 in different aspects have been made in the past decade, issues and challenges remain, such as no systematic study of the effect of different sensitizers have been discussed in a single article, the surface area of invers opal is still low, and the sensitization of high aspect ratio TiO_2 nanostructure is still a challenge. And these issues and challenges are the foucs of this thesis. In specific, chapter 2 is focused on the study of different kinds of sensitizers, their optical properties, band edge positions, electron injection efficiencies and stability for PEC hydrogen generation; chapter 3 is focused on improving the surface area of TiO_2 inverse opal; and chapter 4 is focusing on developing a new and highly sensitization method.

Chapter 2

TiO_2/(CdS, CdSe, CdSeS) Nanorod Heterostructures and Photoelectrochemical Properties

Understanding the physical properties of different sensitizers is the foundation for the design of highly efficient hydrogen generation device and the focus of this chapter. Here, we choose hydrothermally grown TiO_2 nanorod arrays as the model electrode to study and use the chemical vapor deposition method for the deposition of sensitizers. This chapter has been reproduced with permission from *J Luo, L Ma, T He, CF Ng, S Wang, H Sun, HJ Fan. The Journal of Physical Chemistry C 2012, 116, 11956-11963.* Copyright: American Chemical Society.

2.1 Introduction

Solar light driven water splitting by photoelectrochemical (PEC) cells offers an ideal route for H_2 generation due to the sustainable solar energy and abundant water resources.[12, 125] Since the first report on the electrochemical photolysis of H_2O with TiO_2 as photoanode by Fujishima and Honda,[36] the research on water splitting has received increasing attentions. TiO_2 has been one of the most attractive materials for this application because of its high photoactivity and low cost as well as excellent chemical stability.[126] However, because of its large bandgap (~ 3.2 eV), TiO_2 can only harvest the

UV light which takes only 5% of the sunlight, resulting in low energy conversion efficiency. Tremendous efforts have been made to enhance its visible light harvesting ability. Typically, the methods can be summarized into two categories: One way is through bandgap narrowing by element doping,[127],[48],[128] or introducing defect states within the forbidden band.[50] Another strategy is sensitizing TiO_2 with narrow band gap semiconductors such as CdS,[106, 129-131] CdSe[132, 133] and PbS,[134, 135] that is widely employed in quantum-dot sensitized solar cells (QDSSCs). Among various chalcogenides compounds, CdS and CdSe are the most commonly studied sensitizers due to their small band gap of 2.4 and 1.7 eV, respectively, and the synergistic effect of co-sensitization.[136]

Various methods have been developed for the sensitization, mainly in two approaches, post-synthesis assembly and direct growth. In the first method, pre-synthesized quantum dots (QDs) are bind to TiO_2 through organic molecule linkers.[137] The latter method (direct growth) includes chemical bath deposition,[106, 107] successive ionic layer adsorption and reaction (SILAR),[133] electrochemical deposition,[129] and chemical vapor deposition (CVD).[131, 138] The solution-based deposition is most commonly used for sensitizing TiO_2-based PEC anodes. However, the loading of the sensitizer by solution method is generally low, and the charge transfer from sensitizer to TiO_2 could be negatively affected due to the chemical species at the interface of the sensitizer and TiO_2. Direct growth of the sensitizer on TiO_2 by CVD

provides a compact physical contact to favour the charge transfer, a feasible way to increase the loading of the sensitizer, and high crystalline structure.

Albeit a large number of publications on CdS and CdSe sensitized TiO_2 PEC photoelectrodes,[106, 136, 139] little attention[140] has been paid to the effect of the morphology of sensitizer on the PEC performance and comparison of the stability and charge transfer dynamics of different Cd-based semiconductor sensitizers. In contrast to nanoparticles, nanorods possess several advantages, including higher surface areas, easier electron-hole charge separation and thus efficient electron injections, and larger optical absorption cross section.[136, 141, 142] All of these are beneficial to the PEC performance. Furthermore, cadmium chalcogenides differ from each other in terms of band gap, energy level, and chemical stability, and therefore their photosensitizing effect in PEC electrode. A comprehensive investigation of these differences is desirable.

In this chapter, we first deal with the shape effect of the CdS on quasi-aligned TiO_2 nanorod arrays by comparing three different nanostructures. It is found that nanorods have superior sensitizing effect to nanoparticles. We then fabricate CdSe and CdSeS alloy nanorods heterostructured with TiO_2 nanorods array electrodes. Through systematic PEC and optical characterizations, insights on the advantages and drawbacks of these cadmium chalcogenides nanorods in terms of chemical stability and interface electron injection efficiency are obtained. Our results provide useful information on the

structure design and rational selection of suitable photosensitizers on TiO_2 nanorod array-based electrodes towards efficient solar fuel cells.

2.2 Experimental methods

2.2.1 Preparation of TiO_2 nanorod array

The TiO_2 nanorod arrays on transparent conductive fluorine-doped tin oxide (FTO) were synthesized by a hydrothermal growth method according to the literature.[143] In a typical process, the FTO substrates were first cleaned with acetone, ethanol and deionized water for 5 min, respectively, and then dried by N_2 stream. The precursor was prepared by adding 0.45 ml titanium butoxide to a well-mixed solution containing 15 ml of HCl and 15 ml H_2O, and then the whole mixture was stirred for another 10 min till the solution became clear. After that, the precursor was poured into a Teflon-liner stainless steel autoclave with the FTO substrates placed at an angle against the wall with the conductive side facing down. The hydrothermal growth was conducted at 150 °C for 12 h in an electric oven. After that, the FTO substrates were rinsed with deionized water and dried in ambient air.

2.2.2 CVD deposition of CdS, CdSe and CdSeS

The deposition of CdS, CdSe and CdSeS on TiO_2 nanorod arrays was conducted by CVD based on a vapour-solid process without using metal catalyst.[144] The powder of CdS and CdSe precursor was put into a quartz

boat loaded into the center of a one-inch diameter quartz tube placed in a horizontal tube furnace. For the CdSeS alloy sample, considering the lower melting point of CdSe than CdS, CdSe powder was positioned at the upstream inside the quartz-tube furnace to make sure that the CdSe can vaporize with the CdS at a similar speed. FTO substrates grown with the TiO_2 nanorod arrays were put a few cm away from the source. Hydrogen diluted with argon (volume ratio 2%) served as the carrier gas with a flow rate of 10 sccm. The pressure was kept at 10 mbar. The precursor was heated to 700 °C at a rate of 25 °C per min, and kept at the peak temperature for 10 min, 30 min and 50 min for different samples before cooling down naturally to room temperature.

2.2.3 Structural and optical characterization

The morphology of the samples was characterized using a JEOL JSM-6700F field emission scanning electron microscope (SEM). The X-ray diffraction (XRD) patterns were recorded by the Bruker D8 Advanced diffractmeter with the Cu Kα as the radiation source. The UV-visible absorption spectra were recorded by the Cary 100 UV-Vis spectrophotometer. The diffused reflectance spectra were recorded by the Zolix Solar Cell QE/IPCE measurement system equipped with the integrated sphere and a Si diode. For steady state photoluminescence (PL) measurement, the 325 nm line from a He-Cd laser was used as the excitation source. Time-resolved photoluminescence spectra (TRPL) measurements were carried using the

time-correlated single photon counting (TCSPC) technique with a resolution of 10 ps (Pico-Quant PicoHarp 300). The second harmonic of Titanium sapphire laser (Chameleon, Coherent Inc.) at 450 nm (100 fs, 80 MHz) was used as the excitation source. The signal was measured at the wavelength of the correlated steady state PL peak. XPS measurements were performed in a VG ESCALAB 220i-XL system using a monochromatic Al K_{a1} source (1486.6 eV). All XPS spectra were obtained in the constant pass energy (CPA) mode. The pass energy of the analyzer was set to be 10 eV in order to have high measurement accuracy. The binding energy scale was calibrated with pure Au, Ag and Cu by setting the Au $4f_{7/2}$, Ag $3d_{5/2}$ and Cu $2p_{3/2}$ at binding energy of 83.98, 368.26, and 932.67 eV, respectively.

2.2.4 Photoelectrochemical measurements

The photoelectrochemical measurements were carried out in a three-electrode configuration with the as-prepared sample as the working electrode, Pt foil as the counter electrode, and saturated Ag/AgCl as the reference electrode. A mixture of 0.35 M Na_2SO_3 and 0.25 M Na_2S (pH=12.4 tested by the Sartorious PB-11 pH-meter) aqueous solution was used as the electrolyte and sacrificial reagent to maintain the stability of CdS and CdSe.[136] Before experiment, the solution was purged by argon to remove the dissolved oxygen. A 150 W Xe lamp (Sciencetech SS 150 Solar Simulator) equipped with an AM 1.5G filter was used as the light source. The intensity of

the incident light was calibrated with a standard Si solar cell and controlled at 100 mW/cm^2. Current density versus potential (*J*–V) curve of the working electrode was carried out by the linear seep voltammograms with a potentiostat (CHI760D CH Instruments) at a scan rate of 10 mV/s. The photoresponses of the different samples were carried out by potentiostatic (current vs time, I-t) measurements under intermittent illumination at a bias of 0 V versus Ag/AgCl electrode. The incident photon to current efficiency (IPCE) was measured using a Zolix Solar Cell QE/IPCE measurement system with a standard silicon solar cell as reference in three-electrode configuration at 0 V versus Ag/AgCl electrode.

2.3 Results and discussions

2.3.1 Optimizing the structure of CdS on TiO_2 nanorod array

The TiO_2 nanorod arrays on FTO were fabricated by the hydrothermal growth, during which a low precursor concentration was used in order to obtain relatively low density nanorod array (higher precursor concentration would result in severe bundling of the nanorods). The nanorods are quasi-aligned and have diameters of about 100 nm and lengths of about 1.5 μm as revealed by the SEM images in Figure 2.1(a), and the tips of the nanorods are rougher compared to their side faces due to the axial growth. For the subsequent deposition of CdS, the source temperature was maintained at 700 °C, and the

FTO substrates with TiO_2 nanorod arrays were put at the outlet of the furnace with a temperature around 500 °C.

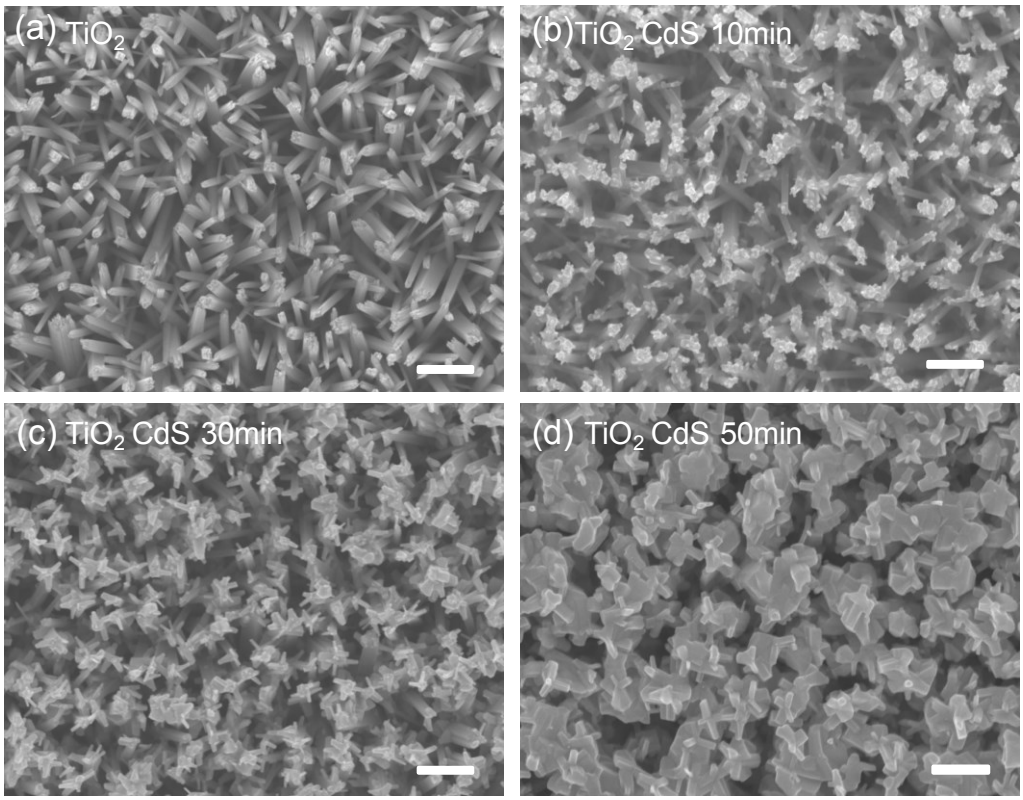

Figure 2.1 *SEM images of the nanostructures.* ***(a)*** *TiO_2 nanorod array grown on FTO.* ***(b)*** *After CVD of CdS for 10 min. The TiO_2 nanorods are covered by CdS nanoparticles on their tops due to preferential nucleation at the rough tips of the TiO_2 nanorods.* ***(c)*** *After CVD of CdS for 30 min. The CdS nanoparticles grow into short nanorods.* ***(d)*** *After CVD of CdS for 50 min with the coalescence of the short rods. The scale bars are 300 nm.*

Figure 2.1(b)–(d) show the morphology of CdS modified TiO_2 nanorod arrays in different deposition time. With a deposition time of 10 min, small CdS nanoparticles are formed on the top part of the TiO_2 nanorods due to preferential nucleation. The nanoparticles grow into the short nanorod structure

as the deposition time increasing to 30 min. Further increasing the deposition time to 50 min causes the formation of large irregular-shaped aggregates of CdS (for convenience, such aggregates are called nanostumps in the following text) covering the entire TiO_2 tips. It is known that vapour-solid (VS) is a typical nanorod growth mechanism occurring at high temperature deposition for various materials including metal oxides.[145-148] The resulting morphology is sensitively dependent on growth parameters such as the vapour pressure (a higher partial pressure is generally required for a high supersaturation), temperature (affect dynamics), and substrate features (e.g., a defect-rich surface is more favourable for nucleation and deposition than flat ones). In our case, the initial nucleation of CdS takes place preferentially at the tips of the TiO_2 nanorods as assisted by their high roughness. These nanoparticles serve as the seed for the next-stage anisotropic growth of short rods. VS growth of rod-shape nanostructure is typical for wurtzite crystals including ZnO.[149] As the deposition time increases, due to the increased overall surface roughness and reduced available space, the VS deposition of CdS occurs preferentially at the irregular sites which are the gaps between the short CdS nanorods, causing a merged growth into a less anisotropic morphology similar to stump.

XRD was conducted to characterize the phase and crystallinity of both pristine TiO_2 nanorod arrays and CdS decorated samples. The patterns are illustrated in Figure 2.2 (a). The hydrothermally grown TiO_2 nanorod arrays have a rutile structure (JCPDS card. No.21-1276) and the deposited CdS

nanoparticle, nanorod and nanostump structures show identical hexagonal wurtzite structure (JCPDS card. No.41-1049), which is in accordance with the previous report.[129, 150] The intensity of the diffraction peaks of CdS increases with increasing the deposition time, which indicates that the loading of CdS could be tuned by varying the deposition time. UV-vis absorption spectra were recorded to test the light harvesting capability of both the pristine and CdS decorated TiO_2 nanorod arrays. Due to the wide band gap of TiO_2, the pristine nanorod array could only absorb up to 410 nm as shown in Figure 2.2 (b).

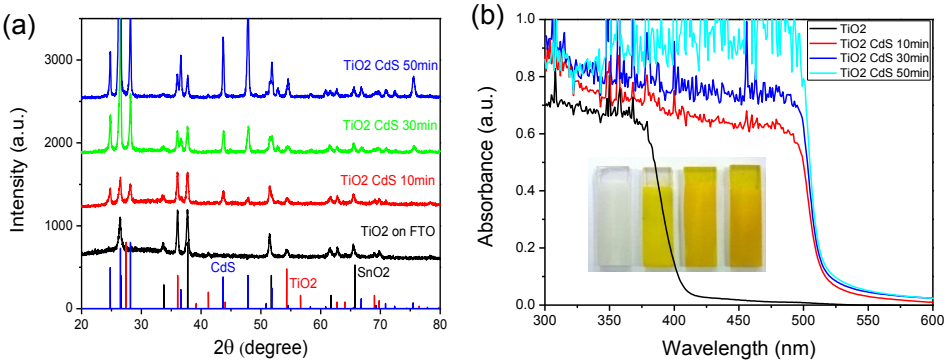

Figure 2.2 (a) *XRD patterns of the samples. The vertical lines are from calculation. Green: wurtzite CdS. Black: rutile SnO_2. Red: rutile TiO_2.* ***(b)*** *The UV-visible absorption spectra of the pristine TiO_2 nanorod array and the CdS-sensitized TiO_2 nanorod arrays. Inset is the photograph of the corresponding samples on FTO/glass.*

After sensitization with CdS, the absorption range broadens up to 520 nm. In addition, the UV-vis absorption spectra also show that as the CdS deposition time increases, the light absorption ability also increases. The type II band alignment between CdS and TiO_2 is favourable for the transfer of photogenerated electrons from CdS to TiO_2.[151] This is one of the reasons that

make the CdS, and other Cadmium Chalcogenides, suitable photosensitizers for TiO_2 as PEC photoanodes. To characterize the ability of the samples for PEC cells, linear sweep voltammograms were recorded both in the dark and with simulated solar light illumination condition to show the *J*-V curves. As shown in Figure 2.3, all electrodes show negligible current under dark condition. With light illumination, pristine TiO_2 nanorod array has a current density of 0.13mA/cm^2 at 0 V versus Ag/AgCl. In comparison, the CdS nanorod

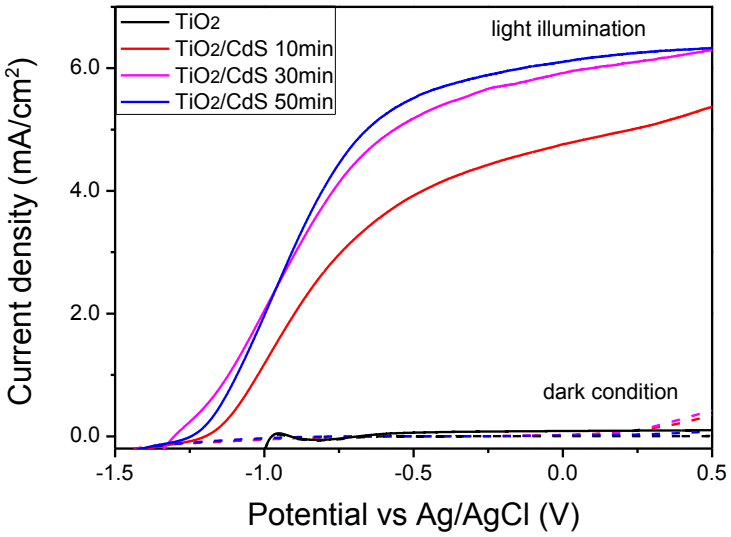

Figure 2.3 *J-V curves of the pristine TiO_2 nanorod array and the CdS sensitized TiO_2 samples under dark condition and simulated solar light illumination.*

sensitized TiO_2 shows a current density of 5.8mA/cm^2, which is nearly 45 times higher than that of the pristine TiO_2 electrode. The great enhancement of the photocurrent after CdS sensitization shows the advantage of the CVD compared to the solution process which has a photocurrent of 5.1 mA/cm^2.[136] For pristine TiO_2, the onset potential is only around -0.85 V. After CdS

sensitization, this value shifted to around -1.25 V, which indicates a shift in Fermi level to more negative potential as a result of the coupling between TiO_2 and CdS in the composite system. Among the three types of CdS morphologies, the CdS loading increases from nanoparticle, nanorod, to nanostump. Their photocurrent densities follow the same trend, except that the nanostump sensitized sample has only a slight increase in the current density compared to the nanorod sensitized one. A higher photocurrent would correspond to a higher efficiency of the PEC device for solar hydrogen generation, as the current is related to the electrons needed to reduce the H^+ ions into H_2 at the Pt cathode.

For a high PEC performance, the loading of the sensitizer needs to balance with the charge recombination loss. In general, a higher loading of the photosensitizer will increase the density of carriers, leading to a higher photocurrent density.[152] On the other hand, as previously reported, an increased sensitizer loading is also accompanied with a higher internal recombination rate within the sensitizer,[153] and a thicker coating of the sensitizer would also reduce the surface area of the photoanode. [154] Both of these two factors would lower the overall efficiency. In our experiment, though the nanostump structure has an evidently higher CdS loading than the nanorods, the increase of the photocurrent level is only marginal. This may be due to the negative contribution of higher internal recombination rate as well as a reduction of the surface area as mentioned above. Therefore, taking the cost of CdS and thermal budget into consideration, further increase of the CdS loading

by prolonged deposition was not attempted in our study; the nanorod structure will be adopted for other Cadmium Chalcogenides sensitizers in the rest part of this study.

2.3.2 Comparison between CdS, CdSe and CdSeS nanorod sensitizers

In this part we deal with other Cd-based narrow bandgap semiconductors

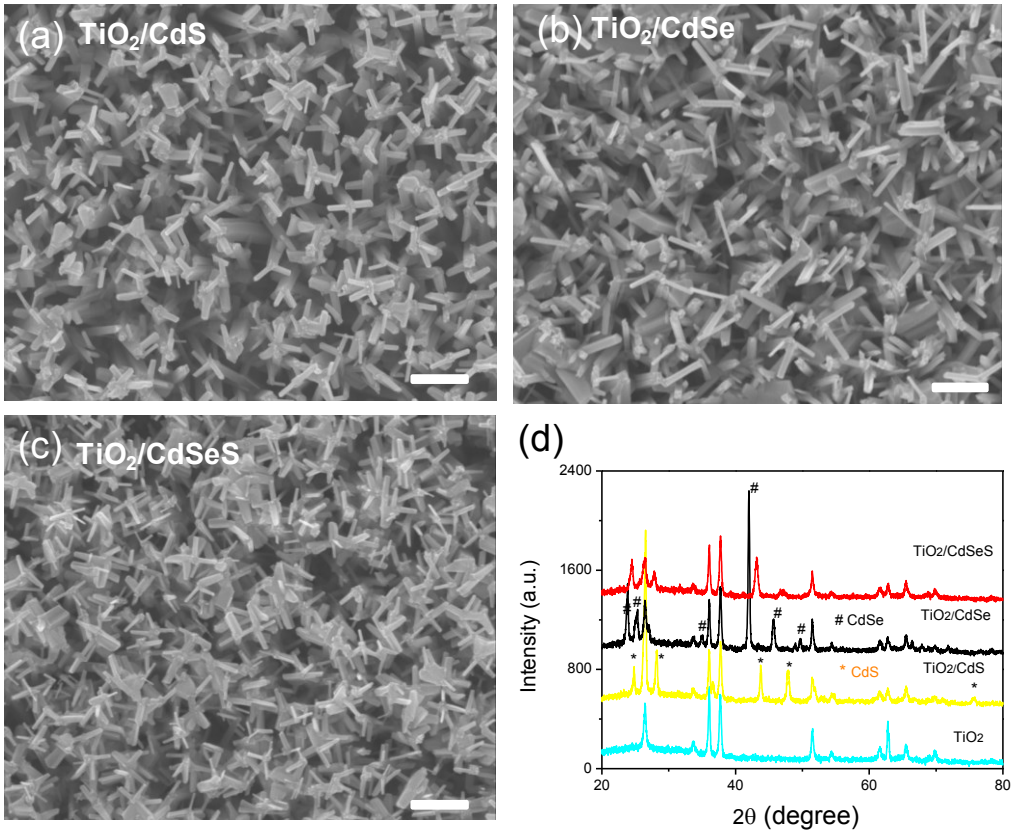

Figure 2.4 *SEM images of the CVD CdS, CdSe and CdSeS for 30 min on top of the TiO_2 nanorod array and their corresponding XRD patterns.* ***(a)*** *TiO_2 /CdS,* ***(b)*** *TiO_2/CdSe,* ***(c)*** *TiO_2/CdSeS, and* ***(d)*** *XRD patterns of the as prepared samples.* The scale bars are 300 nm.

as the photosensitizer of TiO_2. CdSe is commonly used as a co-sensitizer together with CdS because of its much narrower band gap (1.73 eV), albeit a lower conduction band position than CdS.[155] Furthermore, CdSeS alloy

semiconductor has a special advantage as the sensitizer that its band gap is variable by tuning the composition.[138] Following the preceding part, nanorod structures of CdSe and CdSeS alloy were deposited onto TiO_2 nanorod array under the same condition as that for CdS. The SEM images in Figure 2.4 (a)-(c) show that the morphology of the formed nanorods heterostructures is nearly the same. According to the X-ray diffraction data in Figure 2.4 (d), the as deposited CdSe nanorods have the same hexagonal wurtzite structure as CdS. The

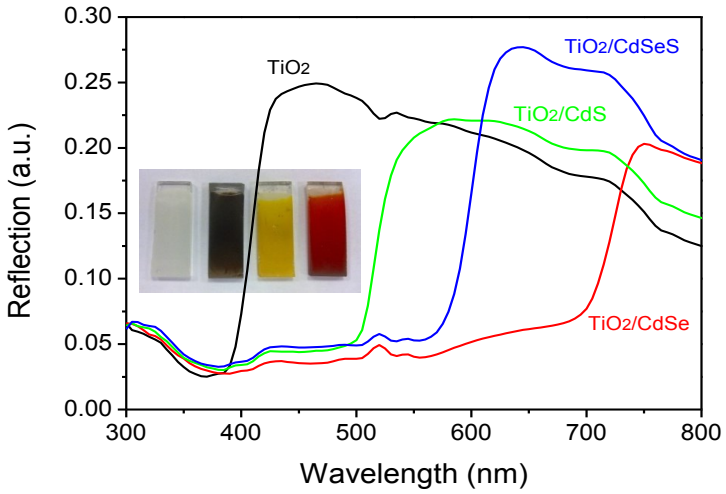

Figure 2.5 *Diffuse reflectance spectra of the pristine TiO_2 nanorod array and CdS, CdSe, CdSeS nanorod sensitized TiO_2 nanorod arrays. Inset: photographs of the as prepared samples.*

diffraction peaks of CdSeS lie between those of CdS and CdSe, which indicates that the CdS and CdSe components are thermodynamically miscible to form the alloy. Diffused reflectance spectra were recorded to reveal the light absorption capability of all the photoelectrodes (see Figure 2.5). Clearly, the absorption range is further increased to 720 nm by coating TiO_2 with CdSe as sensitizer.

For the CdSeS alloy sample, the absorption cuts off at ~ 600 nm in the current sample, between those of CdS and CdSe. The exact composition is unknown but it is not of major concern for its application as photoelectrode. The bandgaps of the different electrodes can be estimated by linear extrapolation of the absorption peaks to the baselines, which are 3.03, 2.39, 1.73 and 2.07 eV for the TiO_2, TiO_2/CdS, TiO_2/CdSe and TiO_2/CdSeS electrode, respectively.

The PEC properties of the above three photoanodes are compared. The linear sweep voltammograms (*J–V* curve) are illustrated in Figure 2.6(a). The CdSe sensitized electrode shows the highest photocurrent, around 9 mA/cm^2 at 0 bias versus Ag/AgCl. However, there is a peak appeared at the saturated photocurrent plateau which could be due to photocorrosion, and will be discussed later. The CdSeS alloy sensitized electrode with a photocurrent of 8 mA/cm^2 takes the second place compared to 6 mA/cm^2 of the CdS sample. One can also see that the CdS and CdSeS sensitized samples have the same onset potential of −1.3 V vs Ag/AgCl. In contrast, the onset potential of the CdSe sensitized electrode is around −1.1 V, which can be ascribed to the lower conduction band edge of CdSe compared to CdS and CdSeS (see also Figure 2.7). To characterize the photoactivity of the electrodes at various wavelengths, the incident photon to current conversion efficiency (IPCE) test was carried out. The results in Figure 2.6 (b) show that the response range of IPCE for each electrode is in accordance with the corresponding diffused reflectance spectrum in Figure 2.5. The IPCE of the CdS and CdSeS sensitized electrodes are around

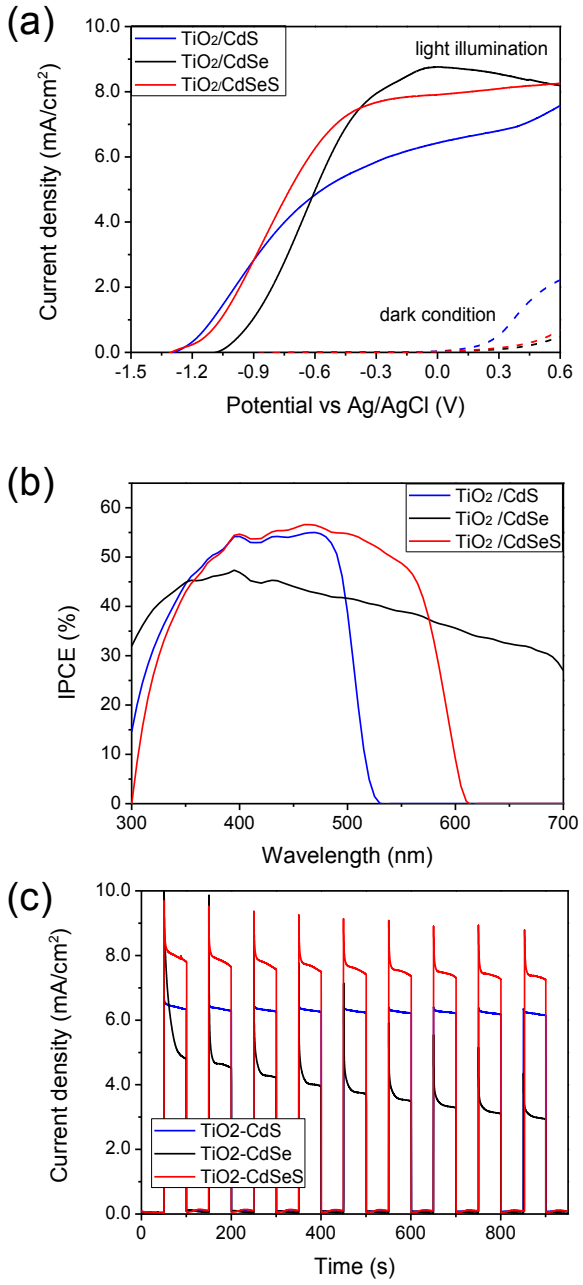

Figure 2.6 *Photoelectrochemical properties of the TiO_2/CdS, TiO_2/CdSe and TiO_2/CdSeS nanorod electrodes.* ***(a)*** *J-V curves.* ***(b)*** *IPCE spectra at a potential of 0 V versus Ag/AgCl.* ***(c)*** *Time-dependent photocurrents and the cycle stability test measured with the penitential bias of 0 V versus Ag/AgCl under chopped light irradiation.*

55% across the absorption ranges, which are higher than the CdSe sample, indicating that electron-hole pairs are separated more efficiently in the CdS and

CdSeS sensitized electrodes. However, the CdSe sample exhibits a wider response range than the former two. This may be the reason why the CdSe/TiO_2 electrode has the highest photocurrent.

In order to show the photo-response and stability of the elctrodes, the photocurrent versus time (*J*–t) curves were recorded in chopped light illumination. From the results in Figure 2.6 (c), the currents of all electrodes are nearly zero in the dark condition and have a transient increase after illumination, which reveals their good photo responses. However, for the TiO_2/CdSe and

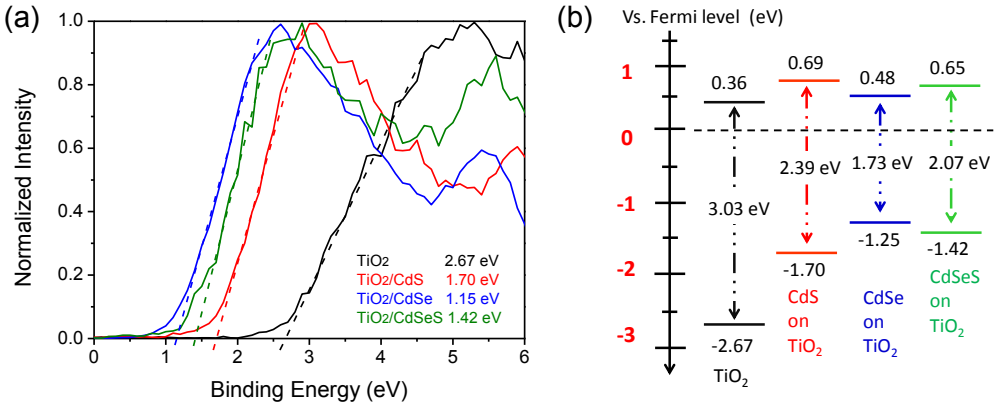

Figure 2.7 (a) *Normalized XPS valence band spectra of the TiO_2, TiO_2/CdS, TiO_2/CdSe and TiO_2/CdSeS electrodes.* ***(b)*** *Band diagram versus Fermi level.*

TiO_2/CdSeS electrodes, the photocurrents show a sharp decrease especially at the first few cycles. This phenomenon is due to carrier recombination according to Kamat;[156] the TiO_2/CdSe electrode has the highest magnitude of decrease as a result of the highest recombination rate in CdSe. With prolonged measurement, the CdS and CdSeS sensitized electrodes maintain stable photocurrents. However, the current of the CdSe sensitized electrode is the least

stable and drops drastically in a few min. The results of the stability of the electrodes are in accordance with the general trend that the narrower the band gap of the material, the less stable the material is.[157]

In addition to the absorption range which controls the light harvesting capability, the conduction band level is another important parameter that determines the onset potential and the electron injection efficiency. XPS is a powerful technique to characterize the valence band maximum (VBM) of a semiconductor. The valence band spectra of the different electrodes were studied by XPS, and the results are illustrated in Figure 2.7(a). The VBM of each electrode is derived by the linear extrapolation method to be 2.67, 1.70, 1.25 and 1.42 eV below the Fermi level for the TiO_2, TiO_2/CdS, TiO_2/CdSe and TiO_2/CdSeS electrode, respectively. Based on the results of the bandgap and the VBM, the positions of conduction band minimum (CBM) could be determined. Figure 2.7(b) shows the band diagrams of each heterostructures electrode from the above obtained bandgap and CBM values. As seen, the conduction band level of the TiO_2/CdSeS is very close to that of the TiO_2/CdS. The CBM of the TiO_2/CdSe is around 0.2 eV lower which is in agreement to the onset potential difference determined from the *J–V* curves (Figure 2.6). Recently Kamat reports that CdSe would undergo phototransformation when in contact with the aqueous sulfide solution (which is the case in our system), [158] forming a thin layer of CdSeS alloy on top of the electrode. As the valence band of CdSeS alloy is lower than CdSe, the layer would inhibit the hole transfer and thus

result in a lower photocurrent after a few min (see Figure 2.6c). The charge separation and transfer mechanism is the internal process that determines the photocurrent and open circuit potential of the electrode. This process can be revealed by measuring the electron injection efficiency by the steady state and time-resolved photoluminescence (TRPL) spectroscopy. [155, 159] Figure 2.8

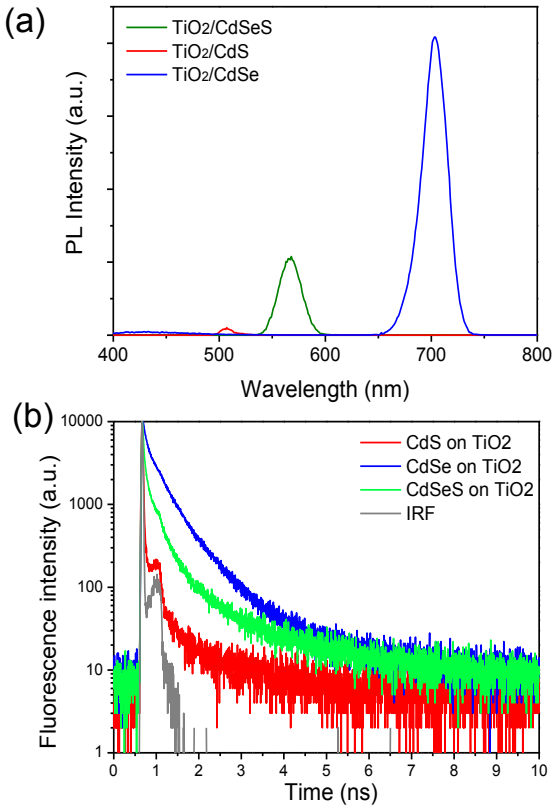

Figure 2.8 (a) *Steady state PL spectra of the TiO_2/CdS, TiO_2/CdSe and TiO_2/CdSeS electrodes at the excitation wavelength of 325 nm with a He-Cd laser.* ***(b)*** *TRPL spectra of the TiO_2/CdS, TiO_2/CdSe and TiO_2/CdSeS electrodes recorded at their corresponding steady state PL peak wavelengths.*

(a) shows the steady state PL spectra recorded at the same excitation intensity using the 325 nm line from a He-Cd laser as the excitation source. The pristine

TiO_2 has nearly undetectable PL signal across the measurement range compared to the intense emissions from the cadmium chalcogenides, which is not surprising since TiO_2 is an indirect wide bandgap semiconductor. From the intensities of the bandgap emissions, the order of the recombination rate can be determined to be TiO_2/CdSe > TiO_2/CdSeS > TiO_2/CdS. TRPL measurements were carried out at room temperature to characterize the electron injection efficiency in detail. The signal was measured at the wavelength of the correlated steady state PL peak, which is 510, 580, and 700 nm for the CdS ,CdSeS alloy, and CdSe sensitized TiO_2 nanrods. Figure 2.8 (b) shows the corresponding TRPL curves of the different electrodes and clearly reveals that CdS sensitized electrode has the shortest PL lifetime among these three which means the carrier transfer from the CdS toward the TiO_2 is the most efficient. The three exponential decay fitting analysis of the obtained curves reveals that the averaged photoluminescence lifetime of these samples are 19 ps for TiO_2/CdS, 220 ps for TiO_2/CdSe, and 58 ps for TiO_2/CdSeS, which are much faster than the reported sensitization by SILAR method,[155, 159] implying that hetero-interface by CVD is more efficient for the electron injection than the one by solution based method. The lowest electron injection efficiency for TiO_2/CdSe electrode indicated the potential chance for phototransformation discussed above. This result is in accordance with the Amperometric *J–t* data (Figure 2.6c) and the conduction band edge position of the different electrodes (Figure 2.7b).

With an optimized CVD condition, it is possible to achieve more homogenous coating of the TiO2 nanorods with cadmium chalcogenides and form core-shell heterogeneous nanowires. As a result of the increased interface areas and interface uniformity, it is envisaged that the IPCE values will be further improved, leading to an enhanced PEC performance. This work is currently underway.

2.4 Conclusion

Nanorods of CdS, CdSe, and CdSeS are deposited onto TiO_2 nanorod arrays as the photoelectrochemical electrode, which are studied thoroughly using optical and electrochemical techniques. A clear picture of the physical processes including charge injection efficiency, band alignment, stability, as well as the effect of the sensitizer morphology is presented. First, when the CdS is changed from particle, rod to stump-shape morphology, the latter two TiO_2 anodes have evidently higher photocurrent densities compared to the nanoparticle sample, which could be a result of competition between light absorption, recombination loss and surface areas. Among the three types of cadmium chalcogenides nanorod sensitizers, it is found that, *i*) while the TiO_2/CdSe electrode has the highest initial photocurrent due to smallest bandgap, the current degrades quickly to the lowest. Maintenance of its high photocurrent may need surface passivation. *ii*) The TiO_2/CdS electrode has the lowest photocurrent but the highest electron injection efficiency, as revealed by the TRPL measurement. *iii*) In terms of the photocurrent level and stability,

TiO_2/CdSeS heterostructure would be a favourable choice. The improvement of the efficiency is the focus of the next two chapters. We will do this in two aspects, the TiO_2 part and the sensitizer part, respectively.

Chapter 3

CdS Sensitized 3-D TiO_2-ZnO Inverse Opal Heteronanostructures

After the study of the physical properties of different sensitizers, we try to develop a highly efficient PEC cell for hydrogen generation by tailoring the TiO_2 structure in this chapter. The work is originally published as *SK Karuturi, J Luo, (equal contribution) C Cheng, L Liu, LT Su, AIY Tok, HJ Fan Advanced Materials 24 (30), 4157-4162.* Copy right: John Wiley & Sons, Inc.

3.1 Introduction

In recent years, PEC cells have attracted worldwide attention as a cheap alternative to conventional devices for solar energy generation and storage. Crucial to the light harvesting and conversion efficiency of a PEC cell is a nanostructured photoanode where the incident photons are captured, electron hole pairs are generated and the subsequent electron transfer takes place.[38, 160] To realize highly efficient PEC cells, nanostructured photoanode should possess several favourable intrinsic characteristics such as adequate specific surface area to permit higher photosensitizer loading (in the case of TiO_2), direct electron transport pathways for longer electron diffusion length and light scattering to promote the light harvesting ability by confining the light within the cell.[161-164] It is thus highly desirable to develop the photoanode that

meet all the above requirements. Towards this goal, immense effort has been put on tailoring the nanoscale features of photoanode materials.[165] Nanoparticle films provide a very high surface area to give higher sensitizer loading, but they lack direct electrical contacts and light scattering ability.[166, 167] On the other hand, one-dimensional nanostructures such as nanowires and nanotubes offer superior electron transport path ways and improved light scattering, but they suffer from very low surface area (roughly an order lower in comparison to nanoparticle films).[114, 115] In conjunction with these efforts, three-dimensional inverse opal (IO) nanostructures possessing highly ordered interconnected shells, high porosity (~75%) and photonic crystal light localization have been shown promising in photovoltaics and PEC cells.[116-124] While the fabrication scalability of these photoanodes has been established using a combination of simple doctor blading method and atomic layer deposition (ALD),[123] the highest efficiencies reported so far still fall behind those of mesoporous nanoparticle films mainly because of the surface area disparity. Highest PEC efficiencies of 3.47% and 2.7% have been reported for dye-sensitized and quantum dots sensitized unmodified TiO_2 IO photoanodes, respectively.[116, 120] The promise of these 3-D photoanodes can be further accomplished when the substantial proportion of pore volume is carefully exploited to resolve the issue of surface area shortage.

Herein, we demonstrate a novel nanoarchitecture consisting of 3-D ordered hierarchical nanobushes, using TiO_2 IO on Fluorine-doped SnO_2 (FTO) glass

substrate as the host template for the facile solution growth of ZnO nanowire networks. The TiO_2 IO-ZnO nanowire hybrid nanostructure is sensitized with CdS quantum dots (QDs) and studied as the PEC photoanode. The key idea here is to couple the ZnO nanowires with the TiO_2 inverse opal to achieve higher sensitizer loading and contact interface area with the electrolyte and enhanced light scattering. PEC performance measurements of nanobushes photoanode indeed show promising photocurrent density.

3.2 Experimental methods

3.2.1 Fabrication of TiO_2 Inverse Opals

Carboxylate-modified, monodispersed polystyrene particles of 500 nm diameter were brought from Duke scientific corporation and were assembled onto the Fluorine-doped SnO_2 (FTO) coated glass substrates via a vertical deposition process at 90 °C.[168] Subsequently, the self-assembled PS opals were infiltrated with TiO_2 using a self-made stop-flow-reactor type of ALD system at 70 °C.[169] Titanium tetrachloride (99.99%, Sigma Aldrich) and H_2O were used as the Ti and O precursors for TiO_2 deposition. Finally, inverse opal structures were developed by burning original polystyrene spheres in air at 450 °C for 2 h. Reactive ion etching (RIE, NSC ES371) has been used to cut the top surface and open up the pores. To give a clear view of the processes, the schematic diagram has been shown in Figure 3.1.

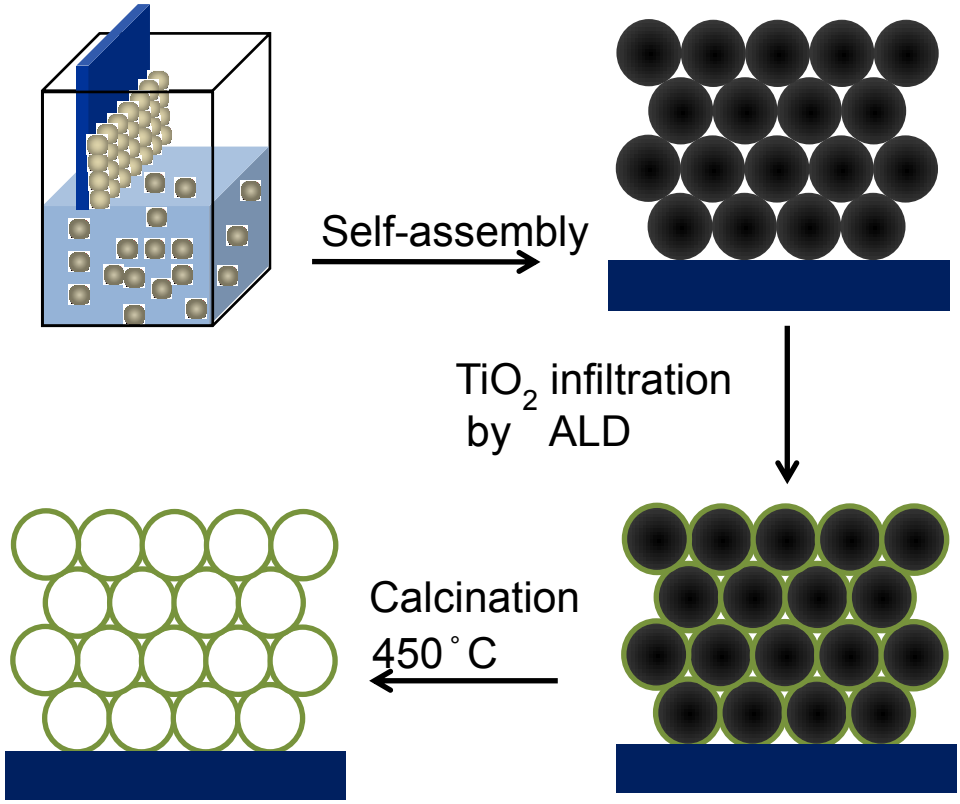

Figure 3.1 *Fabrication processes of the TiO_2 inverse opal. Reprinted with permission from reference 164. [170] Copyright: John Wiley & Sons, Inc.*

3.2.2 Fabrication of nanobushes

A conformal seed layer of ~10 nm ZnO (50 cycles of ALD) was deposited on the internal surface of TiO_2 inverse opals using stop-flow atomic layer deposition method. Subsequently, ZnO nanowires were grown based on the ZnO seed layer within the inverse opal structure using a standard solution growth method.[171] The TiO_2 inverse opal substrates were immersed into a 35-mL aqueous solution of equimolar zinc nitrate, $Zn(NO_3)_2\,6H_2O$ (0.025 M), and hexamethylenetetramine ($C_6H_{12}N_4$) in an autoclave. The reaction was conducted at 95 ^oC for controlled growth times.

3.2.3 Fabrication of ZnO nanowire array

ZnO nanowire array on FTO glass was developed using the standard solution growth method based on ALD ZnO seed layer of ~15 nm (70 cycles ALD) as described above. The growth reaction was conducted for 12 hrs and repeated again with freshly added chemicals for 12 hrs to achieve the desired thickness of ~6 μm.

3.2.4 Preparation of photoanodes

The three different types of nanostructures on FTO glass substrate, namely, TiO_2 inverse opals, nanobushes and ZnO nanowire array were sensitized with CdS quantum dots under the same conditions using a modified method of previous reported SILAR route.[172] In a typical procedure, the nanostructures on FTO glass substrates were immersed in a solution containing 50 mM cadmium acetate tetrahydrate, $Cd(Ac)_2$. $2H_2O$, (Alfa Aesar 98%) in ethanol for 1 min, to allow Cd^{2+} to adsorb onto the TiO_2. They were dried with N_2 stream. The dried substrates were then dipped into a solution containing 50 mM sodium sulfide nonahydrate (98% Na_2S, Alfa Aesar) in methanol for 1 min, where the pre-adsorbed Cd^{2+} reacts with S^{2-} to form the desired CdS. The substrates were then rinsed in water for 1 min to remove the excessive ions and dried again with N_2. This typical procedure was repeated ten times to get a desirable thickness of CdS. The as-sensitized substrates were annealed at 400 °C for 30 min in an Ar protective atmosphere to improve the crystallinity.

3.2.5 Materials characterizations

The morphology and microstructures of the nanostructured films were examined using a JEOL JSM-7600F field emission scanning electron microscopy (FE-SEM), and a JEM 2100F transmission electron microscope (TEM). The X-ray diffraction (XRD) patterns were recorded using Shimadzu thin film XRD equipment using Cu Kα radiation. The specular reflectance spectra were collected at 20° with respect to the normal incidence of light using UV-vis-NIR spectrophotometer (Cary5000, Varian). The diffused reflection spectra were taken using Zolix Solar Cell QE/IPCE Measurement System equipped with an integrating sphere and a silicon diode detector.

3.2.6 Photoelectrochemical characterizations

The PEC performance measurements were conducted in three electrodes configuration with as prepared nanostructured photoanodes as working electrodes, a Ag/AgCl in saturated KCl as a reference electrode and a Pt foil as the counter electrode. 0.25 M Na_2S and 0.35 M Na_2SO_3 mixed solution was used as electrolyte. The photoresponse was measured under chopped illumination from a 150W Xe lamp (Science tech SS150) equipped with an AM1.5 G filter, calibrated with a standard Si solar cell to simulate AM1.5 illumination (100 mW/cm^2). Photocurrent stability tests were carried out by measuring the photocurrents under AM1.5 sun light irradiation (light/dark cycles of 50 s) at a fixed bias of 0 V vs Ag/AgCl. The

incident-photon-to-electron conversion efficiency (IPCE) measurements were taken as function of wavelength from 300 to 650 nm using a specially designed IPCE system for solar cells (Zolix Solar cell Scan100), with two electrodes configuration under 0.5 V bias (the photocurrent level at this potential is comparable to 0 V vs Ag/AgCl). A 150 W Xe lamp equipped with gratings was used to generate a monochromatic beam. The incident light intensity was calibrated by a standard silicon photodiode.

3.3 Results and discussions

3.3.1 Analysis of the crystal phase, light absorption and morphological properties of the electrode

The fabrication procedure for the nanobushes photoanode is outlined in Figure 3.2. Self-assembled opal templates with face centered cubic lattice structure and long range ordering were developed using monodispersed polystyrene particles of 500 nm diameter and infiltrated with TiO_2 by ALD with close to theoretical filling fractions as demonstrated in previous works.[169, 173-176] After heat treating the as-infiltrated opal templates at 450 ^oC, TiO_2 IOs with highly ordered, interconnected spherical pores in hexagonal arrangements were obtained as shown in Figure 3.3 (a) and (b). The thickness of the TiO_2 shells can be estimated to be ~ 40 nm based on the maximum possible coating thickness, which is around 7.75% of the diameter of polystyrene particles. The obtained TiO_2 IOs of ~6 μm thickness were coated

with ~10 nm thick conformal ZnO film which serves as the seed layer for subsequent solution growth of ZnO nanowires, forming a 3-D ordered nanobushes structure.

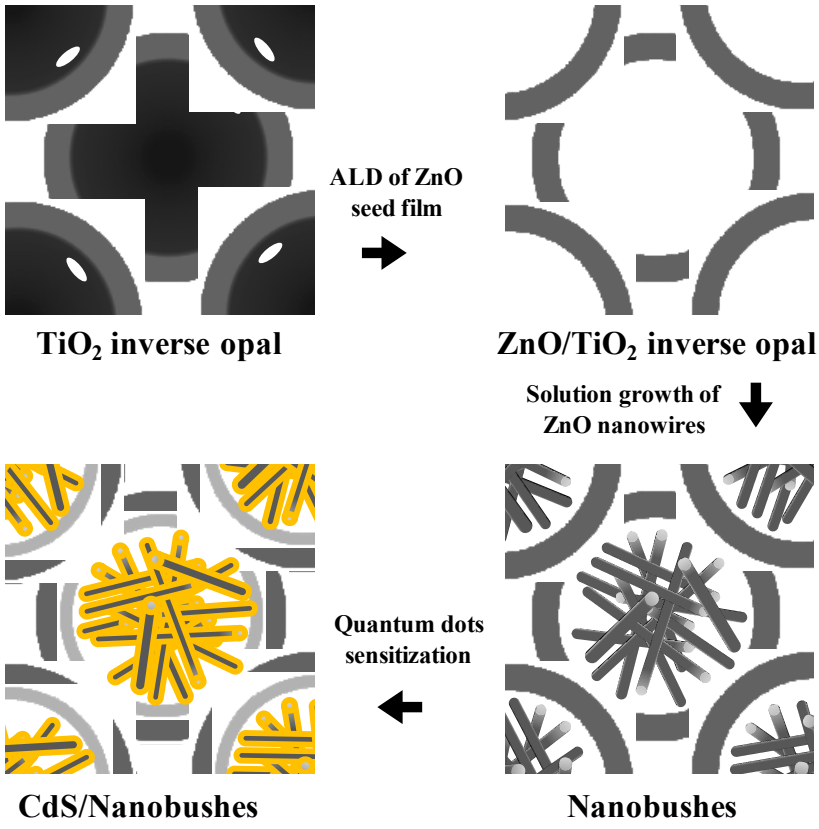

Figure 3.2 *Fabrication process for nanobushes photoanode.*

Growth conditions were optimized to control the nanowire diameter and length as detailed in the experimental section. Figure 3.3 (c) shows the top view FESEM image of the obtained nanobushes structure after 9 h of solution growth. At higher magnification, inset of Figure 3.3 (c) shows a single nanobush within an IO pore comprised of multiple ZnO nanowires randomly aligned covering the entire pore uniformly. Cross-sectional view of the nanobushes structure observed at a crack area can be seen in Figure 3.3 (d) depicting hierarchical organization of nanobushes. This kind of 3-D ordered growth of nanobushes is

observed over the entire high aspect ratio template of 1 cm^2. It is noted that although the 9 h growth was used to achieve the longest nanowires within the pore, the wire length can be conveniently controlled by changing the reaction time. In addition, the size of the nanobushes can also be tuned by changing the pore size, Figure 3.4.

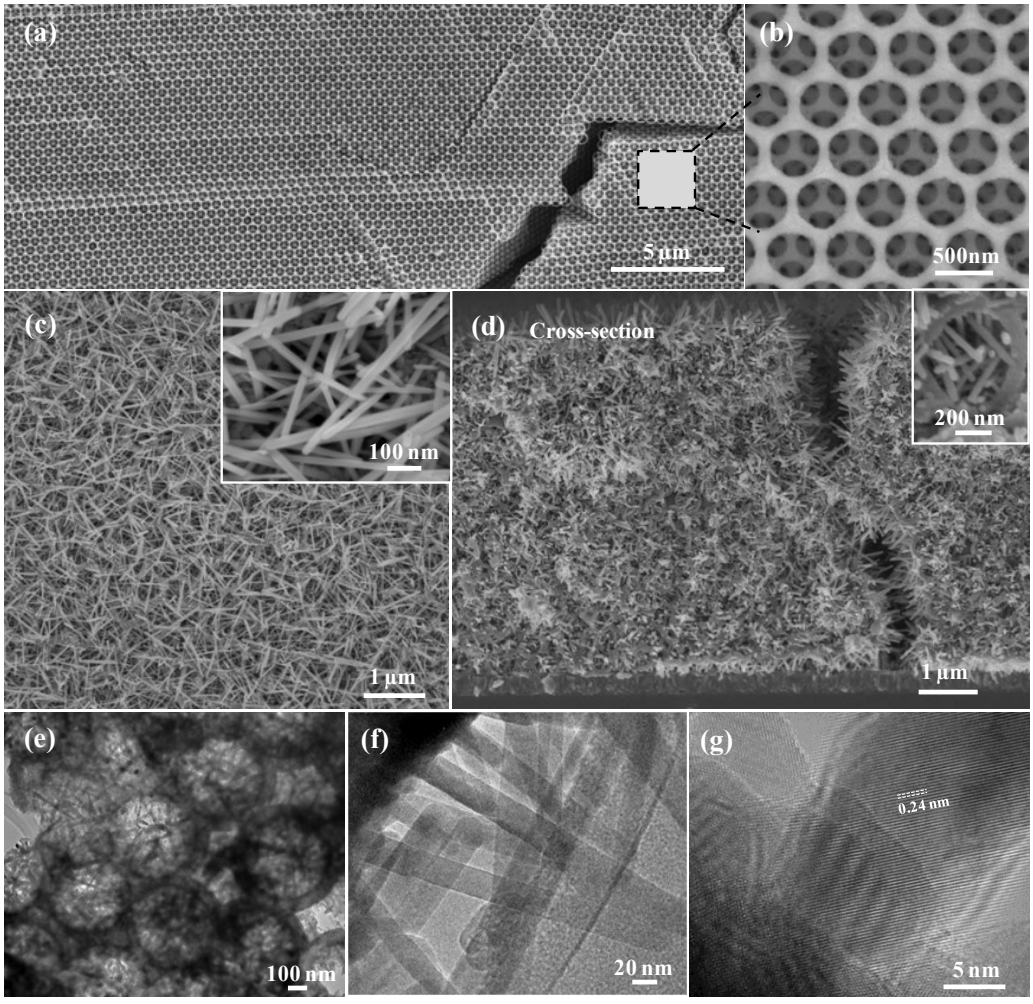

Figure 3.3 (a), (b) *Top view FESEM images of TiO_2 inverse opal at different magnifications.* ***(c), (d)*** *FESEM images of nanobushes structure;* ***(c)*** *top view and* ***(d)*** *cross-sectional view. The insets of* ***(c), (d)*** *show the magnified top view and cross-sectional view of a single nanobush structure, respectively.* ***(e), (f), (g)*** *TEM images of nanobushes structure taken at different magnifications.*

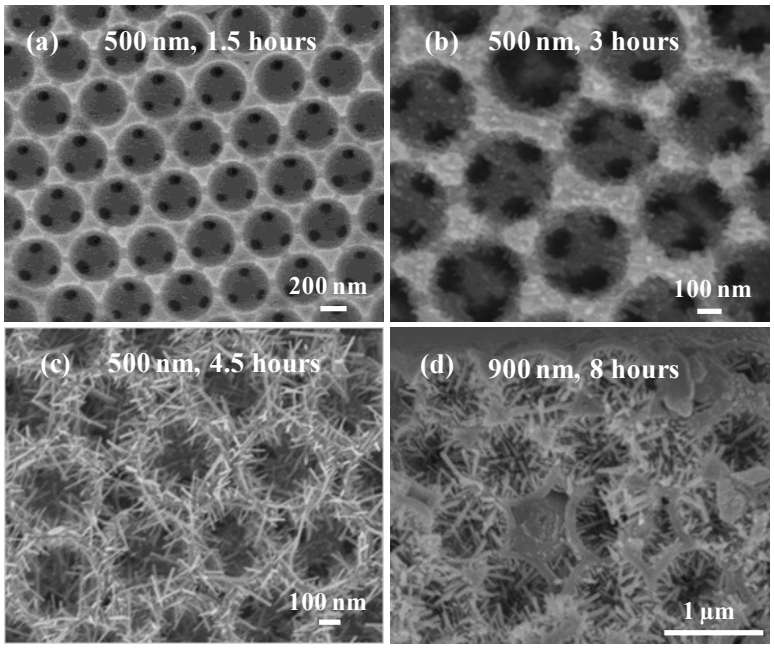

Figure 3.4 *Top view FESEM images of 500 nm pore size TiO_2 IOs with ZnO nanowires grown for different times;* ***(a)*** *1.5 hrs of solution growth,* ***(b)*** *3 hrs of solution growth and* ***(c)*** *4.5 hrs of solution growth.* ***(d)*** *Cross-sectional FESEM images of 900 nm pore size TiO_2 IOs with 8 hrs solution growth of ZnO nanowires.*

The nanoscale feature of the as-fabricated nanobushes was further examined using transmission electron microscope (TEM). Figure 3.3 (e) reveals the densely grown nanobushes within each opal pore. The diameter of the nanowires is ~30 nm as estimated from Figure 3.3 (f). At higher magnification, Figure 3.3 (g) shows the interface between the nanowires and ZnO seed film. Nanowires are highly crystalline exhibiting an inter-plane spacing (0.24 nm) that matches closely with the d-spacing of (101) plane in hexagonal ZnO. One notable feature of hierarchical nanobushes over vertically aligned ZnO nanowire array directly on transparent conducting substrates is the complete elimination of fusion of wires at their roots that commonly occurs when growing the nanowires of several microns length.[177] In addition, the dense

networks of nanowires with small diameters can be hierarchically extended to tens of microns by simply adjusting the thickness opal templates, fulfilling the high interfacial area requirement for PEC cells.

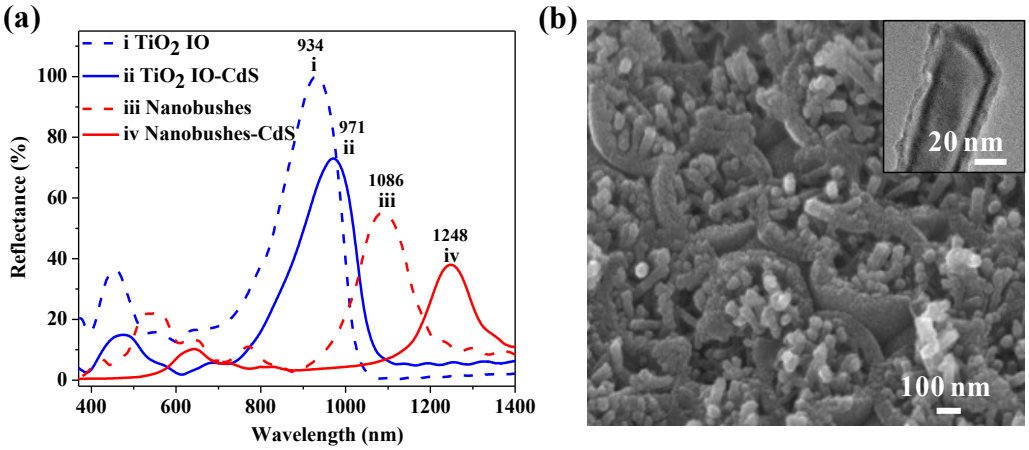

Figure 3.5 (a) *UV-vis-NIR specular reflectance spectra showing the photonic stop bands of i) TiO_2 IO, ii) CdS QDs sensitized TiO_2 IO, iii) nanobushes and iv) CdS QDs sensitized nanobushes.* ***(b)*** *Cross-sectional FESEM images of CdS QDs sensitized nanobushes photoanode; inset of* ***(b)*** *shows the HRTEM image of a single nanowire sensitized with CdS.*

Owing to the highly periodic arrangement of spherical pores, TiO_2 IOs are 3-D photonic crystals exhibiting photonic bandgaps, where the propagation of light is prohibited. TiO_2 IOs possess photonic stop bands centered at 934 nm (Figure 3.5 (a) i) with higher order photonic bands in the visible part (~450 nm). After growing the nanobushes, the stop band red shifted to 1086 nm (Figure 3.5 (a) iii) with comparable bandwidth and higher order photonic bands, manifesting that the long-range structural order is overall preserved. Since the position and width of the bandgap are dictated by the lattice size and refractive indices,[178] red-shift of the bandgap occurred due to the increased dielectric index after the deposition of ZnO seed film and the growth of nanowires within

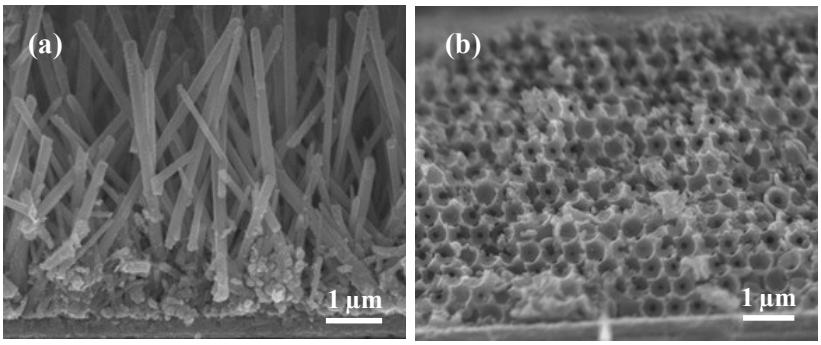

Figure 3.6 *Cross-sectional FESEM images (a) CdS quantum dots sensitized ZnO nanowire array and (b) CdS quantum dots sensitized TiO_2 inverse opals.*

the IO pores. Given the general interest in optical properties of ZnO nanowires and the ability of photonic crystal in confining, manipulating and guiding photons, this result augurs well for interesting optoelectronic properties of such coupled structure.[179, 180]

To comparatively examine the PEC performance of nanobushes photoanode, photosensitization with CdS QDs was carried out for the three

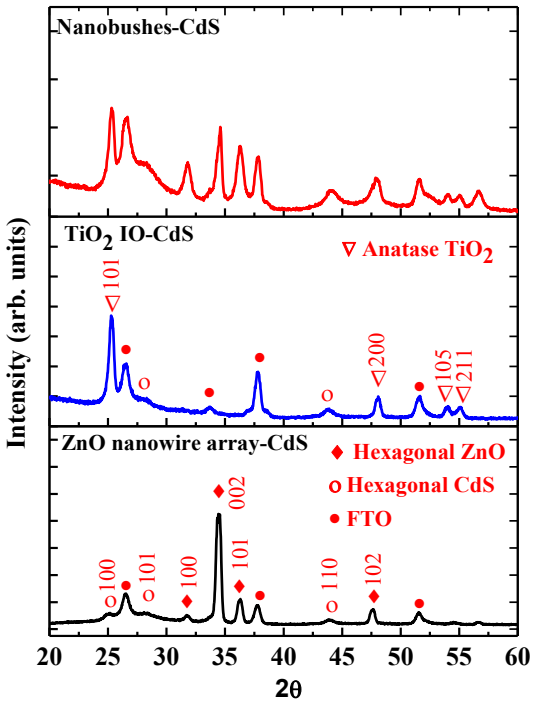

Figure 3.7 *XRD patterns recorded from CdS quantum dot sensitized photoanodes.*

nanostructured photoanodes, namely, TiO_2 IO, nanobushes, and ZnO nanowire array. The thickness for all the nanostructured photoanodes was kept at ~6 μm, Figure 3.6. Hexagonal CdS QDs is confirmed from X-ray diffraction patterns, Figure 3.7. Curves ii and iv in Figure 3.5(a) show the photonic stop bands after the CdS sensitization. Photonic bandgap shift of 37 nm and 162 nm can be observed for the TiO_2 IO and nanobushes, respectively. Larger shift for the nanobushes means that the amount of CdS QDs loading is increased by several times due to the higher specific surface area provided by the networks of nanowires within each pore. Quantitative analysis of the XRD patterns also confirms three times higher QDs loading in the nanobushes in comparison to the TiO_2 IO. Of major concern here is whether there exist photonic bands for the photoanodes within the absorption wavelength range of CdS (below ~530 nm). As seen from Figure 3.5(a), no major specular reflectance features below 530 nm were found for QDs sensitized nanobushes, whereas a high-order peak centered at ~470 nm exists for the sensitized TiO_2 IO. The absence of specular reflection features in the nanobushs is beneficial for light harvesting. FESEM image in Figure 3.3(b) shows the cross-sectional view of QDs sensitized nanobushes photoanode. Distinct CdS/ZnO core-shell nanowires without any aggregation can be observed. Interconnection of the TiO_2 shells that provide direct electron transport pathways can also be seen. TEM image of a detached nanowire from the nanobush structure verifies the CdS shell of ~7 nm around the entire ZnO nanowire.

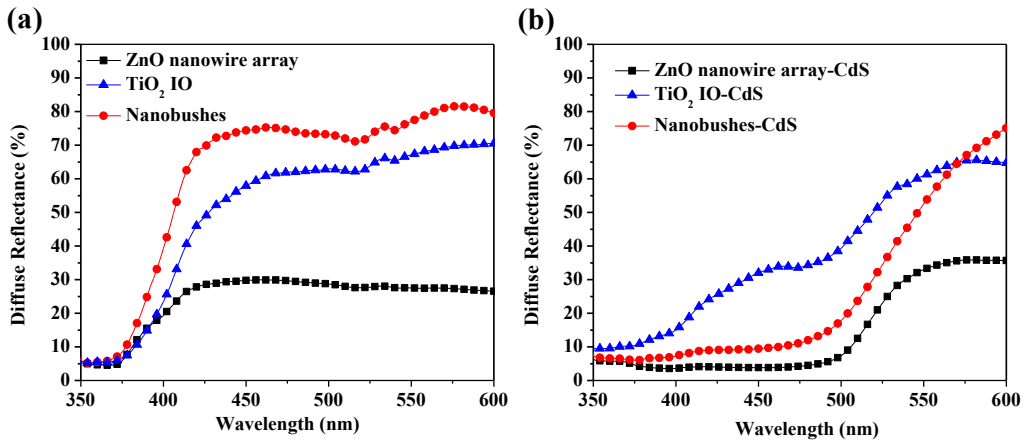

Figure 3.8 *UV-vis diffuse reflectance spectra of different photoanodes,* ***(a)*** *before CdS QDs sensitization and* ***(b)*** *after CdS QDs sensitization. Strong light scattering exhitbited by the 3-D photoanodes is expected to increase the path length travelled by the light with in the photoanode and thus the PEC light harvesting.*

In order to investigate the light scattering ability of different photoanodes, the UV-vis diffuse reflectance spectra before Figure 3.8(a) and after Figure 3.8(b) CdS QDs sensitization were measured. In the absence of CdS coating, the highest scattering was found in nanobushes structure, followed by TiO_2 IO and ZnO nanowire array. Given the fact that the effective Mie scattering originates from the particles with the size comparable to the wavelgth of the inccident light, void size of inverse opal used herein (~500 nm) apparently contributed for strong visible light scattering.[181] This clearly highlights the benefits of the 3-D structured photoanodes with specially engineered scattering centers over the one-dimensional ZnO nanowire array. Previous reports also suggest that disorder in photonic crystals induces broadband diffuse scattering.[182-184] The higher disorder present in the nanobushes due to the growth of ZnO nanowires is also expected to contribute

additionally to the improved diffuse scattering. As expected, all the photoanodes after sensitization show decreased diffuse reflectance in the wavelengths range up to 550 nm due to the light absorption by CdS. However, nanobushes-CdS photoanode shows very low diffuse reflectance in comparison to TiO_2 IO-CdS photoanode. This is attributed to the much higher amount of CdS anchored to the ZnO nanowire networks, which promotes stronger absorption of the scattered light in comparison to TiO_2 IO-CdS photoanode, thereby effectively capturing the benefits of strong light scattering with minimum reflection losses. Moreover, presence of higher order photonic bands for TiO_2 IO-CdS photoanode (Figure 3.5 (a) ii) may have contributed to specular reflections.

3.3.2 Investigation and understanding of the PEC performance of the electrodes

The PEC performance of different photoanodes was investigated by conducting the current density vs potential (I-V) measurements under the dark and simulated sunlight illumination (AM 1.5) in a three-electrode cell configuration. As shown in Figure 3.9(a), all the photoanodes present pronounced photocurrent density upon illumination, implying efficient light harvesting and charge separation. Typically, all the photoanodes show similar onset potentials with continuously increasing photoresponse with increasing bias voltage. The photocurrent density for nanobushes-CdS photoanode can be observed as 6.2 mA cm^{-2} at 0 V vs Ag/AgCl, compared to 3.6 and 2.9 mA cm^{-2}

for the photoanodes based on TiO_2 IO-CdS and ZnO nanowire array, respectively, measured under the same conditions.

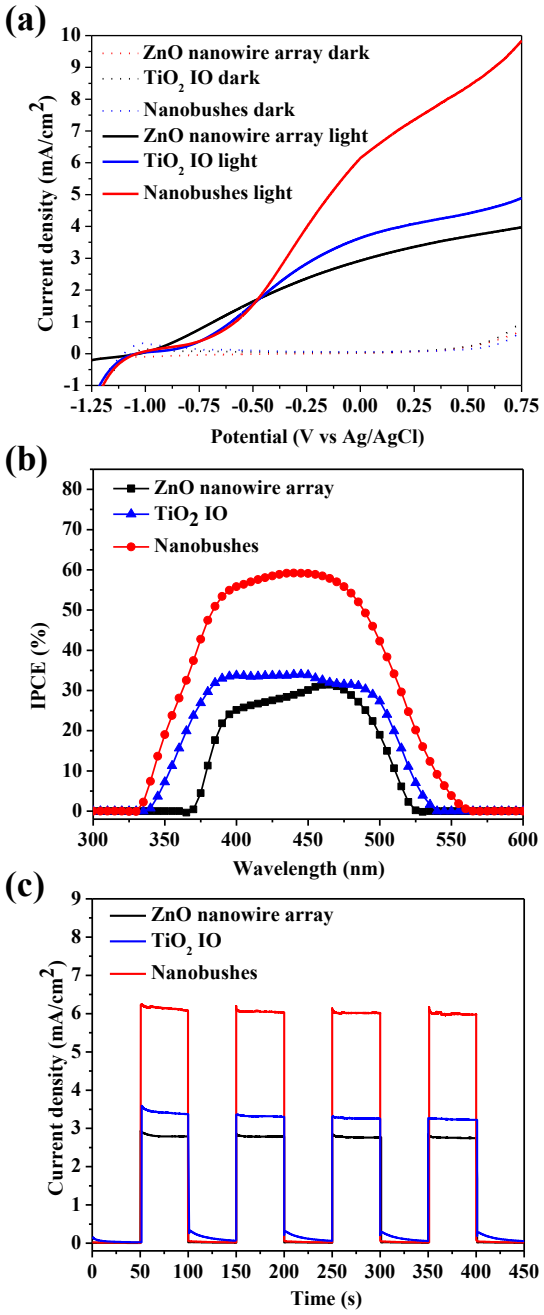

Figure 3.9 (a) *Linear sweep voltammetry measurements of the CdS QDs sensitized photoanodes; dotted lines show the measurements collected in the dark and the solid lines show the measurements collected under 100 mW* cm^{-2} *simulated sunlight illumination.* ***(b)*** *IPCE spectra of different photoanodes.* ***(c)*** *Amperometric I-t curves for CdS QDs sensitized photoanodes at an applied potential of 0 V vs AgCl/Ag at 100 mW* cm^{-2} *illumination with 50 s light on/off cycles.*

To evaluate the wavelength-dependent light harvesting efficiency of different photoanode structures, incident-photon-to-electron conversion efficiency (IPCE) tests for all the three photoanodes were performed from 300 nm to 600 nm wavelengths under 0 V bias, Figure 3.9(b). Strong photoactivity for all the photoanodes is observed in the visible light region from 375 nm to 525 nm. In contrast to the ZnO nanowire array-CdS photoanode, both the 3-D structured photoanodes show broader photoresponse indicating the indispensible role of light scattering to improve the light harvesting efficiency. Highest efficiencies for nanobushes and ZnO nanowire array photoanodes can be determined to be 60% and 30% respectively at the wavelength of around 460 nm. Considering the transmission losses of ~20% through FTO and the cell, 60% efficiency shows the immense potential of the hierarchical 3-D nanobushes for PEC cell applications. For the photoanode based on TiO_2 IO, the maximum efficiency of 36% can be discerned at around 405 nm with relatively flat conversions in the active region. This contrasting light harvesting feature could be attributed to the reflection losses at wavelengths >420 nm with the presence of higher order photonic stop bands, Figure 3.5(a)ii and Figure 3.8(b). IPCE results for all the photoanodes are also consistent with their corresponding I-V characteristics. Fast photoresponse and good photostability are observed for all the photoanodes from amperometric *I-t* curves, Figure 3.9(c). The improved performance for nanobushes photoanode may also be partly attributed to the fact that ZnO seed film coated on the electron transporting TiO_2 shells may

function as an energy barrier to suppress the recombination of photoinjected electrons with redox ions of the electrolyte.[185-187]

3.4 Conclusions

In summary, we demonstrated for the first time a facile fabrication strategy for 3-D ordered nanobushes comprising dense networks of ZnO nanowires embedded within TiO_2 inverse opals. Justified by several favorable attributes such as high specific surface area, direct electron transport networks and strong light scattering, the promise of the novel nanohierarhicial photoanode is unambiguously demonstrated for photoelectrochemical cells based on CdS quantum dots sensitization. A photocurrent density of 6.2 mA cm^{-2} at 0 V vs Ag/AgCl under AM1.5 simulated solar light illumination is achieved, which confirms the potential of novel nanobushes photoanode for photoelectrochemical cell applications. Perspectively, such hybrid nanobush photoanodes could be also equally useful in photovoltaics.

Chapter 4

A New Sensitization Method Based on Atomic Layer Deposition for Highly Efficient Hydrogen Generation

This chapter focuses on the sensitizer part to improve the PEC hydrogen generation efficiency. In the past, variously methods for the sensitizer deposition have been developed. However, the penetration of the sensitizer into the complex high aspect ratio structures is still a challenge. In this chapter, we try to solve this problem by combining two powerful techniques, atomic layer deposition (ALD) and ion exchange reaction (IER) together. The work is originally published as *J Luo, SK Karuturi, L Liu, LT Su, AIY Tok, HJ Fan Scientific Reports 2012, 2, 451.*

4.1 Introduction

Ever since the seminal paper on photoelectrolysis of water by Fujishima and Honda,[36] TiO_2 has received wide attentions in photocatalysts, water splitting and solar cells due to its high photoactivity, low cost and excellent chemical stability.[8, 188-190] The limiting factor for TiO_2 is the large band gap (~3.2 eV), which defines its light absorption range only in the UV part . During the past three decades, tremendous efforts have been put to enhance the visible light harvesting ability of TiO_2.[191] Heterogeneous structures have

been proposed to couple TiO_2 with materials exhibiting visible light harvesting ability, and the first trial was done by Serpone et al to couple TiO_2 with CdS which showed a significant improvement.[192] Later on Graetzel made a significant breakthrough in sensitizing TiO_2 with dye molecules, viz., the dye-sensitized TiO_2 photoanode.[189] Following the invention of Graetzel cell, quantum dot sensitized solar cells (QDSSC) quickly catches up due to the mature quantum dot synthesis protocol developed by Peng and Alivisatos.[193, 194] The key development of QDSSC is made by Kamat in 2005, with the pre-synthesized CdSe nanocrystals linked to TiO_2 thin films by organic molecules to harvest the solar energy.[156] Since then various methods of sensitization were developed, and they can be summarized into two main categories: assembly of pre-synthesized QDs and direct growth.[105, 152] Pre-synthesis provides the feasibility of facile control in the size, size distribution and morphology. However, the charge transfer would be retarded by the surface functional molecules. Also the loading of the sensitizer prepared by this method is usually low. Direct growth allows both a compact contact of the sensitizer with TiO_2, and the ease of increasing the loading of the sensitizer. A diverse range of methods are reported for the coating of the sensitizer, such as chemical bath deposition, [106, 107] successive ionic layer adsorption and reaction (SILAR),[108-110] electrochemical deposition,[111] chemical vapour deposition[112] and electrophoretic deposition.[113]

Despite the development of various sensitization methods, the sensitizer still suffers from poor thickness and uniformity control especially for deposition on high aspect-ratio TiO_2 nanostructures. As the size of QDs is much larger than dye molecules, penetration of QDs into TiO_2 nanoarchitectures with a depth >10 μm is more difficult than the case in dye-sensitized solar cells.[152] Due to the quantum confinement effect and the limited charge diffusion length, the size of the QDs plays an important role in charge transfer process. The poor control in conventional deposition techniques usually leads to aggregation of QDs into large particles, thus causing high internal recombination loss.

Atomic layer deposition (ALD) is a thin film deposition technique that is based on self-limiting surface reactions by sequential exposure to different gas phase precursors.[195] ALD provides precise thickness control at the angstrom or monolayer level and deposition on high aspect ratio nanostructures with excellent step coverage. By employing ALD for QDs sensitization, excellent infiltration and conformity could be achieved, and the size of QDs could be varied by simply tuning the number of ALD cycles. Recently Stacey et al showed the ALD CdS for solid state QDSSC.[196] However, there is a serious safety issue for such ALD CdS process, as the precursors of dimethyl cadmium (DMCd) and hydrogen sulfide (H_2S) are highly toxic.

Liquid-phase reaction via ion exchange has been developed as a method to fabricate semiconductor heteronanostructures.[197, 198] The principle of ion exchange is based on the solubility of the material which allows only a critical

selection of the target materials. Very recently ion exchange reaction has also been employed to fabricate nanowire p-n junctions for photovoltaics,[199] as well as photosensitizer layers on ZnO nanowires for semiconductor-sensitized solar cells.[200, 201] Due to its amphoteric property, ZnO is unstable for PEC in either acidic or alkaline electrolyte solutions, which is the bottleneck for practical applications. On the other hand, the amphipathicity of ZnO makes it an ideal template for nanofabrications. [202]

In order to have the merit of ALD without the highly toxic source for the QDs sensitization, in this chapter, ALD ZnO thin films were deposited on various TiO_2 nanostructures as the sacrificial templates to convert to the short bandgap semiconductor sensitizers by ion exchange reaction (we call the whole process as ALDIER). The thickness and the size of the sensitizer could be controlled by the thickness of the ZnO layer and the condition of ion exchange reaction. The reproducible photocurrent levels >15 mA/cm^2 is obtained using the TiO_2 inverse opals (TIO), which is the highest among all nanostructure TiO_2-based PEC cell for hydrogen generation. It is envisaged that when the electrodes are constructed into QDSSC, the efficiency could also be improved.

4.2 Experiment methods

4.2.1 Fabrication of TiO_2 Inverse Opals

Carboxylate-modified, monodispersed polystyrene spheres of 500 nm diameter (Duke scientific corporation) were assembled onto the Fluorine-doped

SnO_2 (FTO) coated glass substrates via a vertical deposition process at 90 °C.[170, 203] The self-assembled polystyrene sphereopals were then infiltrated with TiO_2 using a stop-flow-reactor ALD system at 70 °C, for which titanium tetrachloride (99.99%, Sigma Aldrich) and H_2O were used as the Ti and O precursors, respectively. Finally, TiO_2 inverse opal structures were developed by burning the original polystyrene spheres in air at 450 °C for 2 h, which also improved the crystallinity of the TiO_2. Last, reactive ion etching (RIE, NSC ES371) was used to cleave the top surface and open up the pores.

4.2.2 Preparation of TiO_2 particle film

TiO_2 nanoparticle films were deposited on the FTO by successive screen-printing using a TiO_2 paste consisting of Degussa P25 TiO_2 powder and an ethyl cellulose binder in α-terpinol.[110] The projected area of the TiO_2 layers was approximately 0.28 cm^2 (circles with 0.6 cm diameter). Then, the TiO_2 electrodes were gradually heated to 450 °C where they were held for 15 min before being heated to 500 °C for a further 30 min.

4.2.3 ALD ZnO layer and Ion Exchange Reactions

ZnO layers with different thickness were conformably deposited onto the TIO as the sacrificial layers for ion exchange reaction by ALD with the Diethyl Zinc (DEZ, 99.99%, Sigma Aldrich) and H_2O as the Zn and O precursors respectively. The ZnO coated TIOs were then annealed in air at 450 °C for 30 minutes to improve crystallinity. TIO/ZnSe core/shell structure was prepared by

immersing the ZnO coated TIO in a Se^{2-} ion solution (0.05 M, prepared by reacting 0.79 g Se powder with 0.8 g $NaBH_4$ in 200 ml deionized water) and kept at 60°C for 5 hours in order to fully exchange the ZnO layer into ZnSe.[201] The samples were then washed with deionized water and absolute ethanol and finally dried in air. Due to the fact that Se^{2-} is vulnerable to oxygen, all the experiments containing Se^{2-} ions were done in glove box. The TIO/ZnSe core/shell structures were then reacted with the 0.1 M $CdCl_2 \cdot 2.5H_2O$ aqueous solution at 90−140 °C for 10 hours to replace Zn^{2+} by Cd^{2+} in the ZnSe shell. By controlling the reaction temperature, the composition of the TIO/$Zn_xCd_{1-x}Se$ core/shell structure could be tuned. Finally, TIO/$Zn_xCd_{1-x}Se$ core/shell nanostructure was annealed in argon atmosphere at 400 °C for 30 minutes to improve crystallinity.

4.2.4 SILAR of CdSe on TIO

The SILAR process was modified from the previous reports.[108, 110] In a typical procedure, the TIO electrodes were immersed in a solution containing 0.05 M cadmium acetate dihydrate ($Cd(Ac)_2 \cdot 2H_2O$, Alfa Aesar, 98%) in ethanol for 1 min, to allow Cd^{2+} to adsorb onto the TiO_2 surface, and then rinsed with ethanol for 1 min to remove the excess Cd^{2+}. The electrodes were then dried for 2 min in an argon atmosphere. Subsequently, the dried electrodes were dipped into a solution containing 0.05 M Se^{2-} for 1 min. The Se^{2-} solution was prepared by mixing selenium (Se, Sigma-Aldrich, 99.8%) and sodium

borohydride (NaBH4, Sigma Aldrich, 99.8%) in water. The electrodes were then rinsed in ethanol for 1 min and dried again in an argon atmosphere for another 2 min. This procedure was repeated several times to get desired CdSe loading.

4.2.5 Materials Characterizations

The morphologies and microstructures of the nanostructured films were examined using a JEOL JSM-7600F field emission scanning electron microscopy (FE-SEM), and a JEM 2100F transmission electron microscope (TEM). The X-ray diffraction (XRD) patterns were recorded by Shimadzu thin film XRD equipment using Cu Kα radiation. The diffused reflection spectra were taken using Zolix Solar Cell QE/IPCE Measurement System equipped with an integrating sphere and a silicon diode detector.

4.2.6 Photoelectrochemical Characterizations

The PEC performance measurements were conducted in three electrodes configuration with the as prepared nanostructured photoanodes as working electrodes, Ag/AgCl in saturated KCl as a reference electrode and Pt foil as the counter electrode. 0.24 M Na_2S and 0.35 M Na_2SO_3 mixed aqueous solution was used as the electrolyte. The current density vs potential (*J*-V) measurements were measured in both dark and illumination with a 150W Xe lamp (Science tech SS150) equipped with an AM1.5 G filter, calibrated with a standard Si solar cell to simulate AM1.5 illumination (100 mW/cm^2).

Photocurrent versus time (*J*-t) curves were carried out by measuring the currents under chopped light illumination (light/dark cycles of 50 s) at a fixed bias of 0 V vs Ag/AgCl. The incident-photon-to-current conversion efficiency (IPCE) measurements were taken as a function of wavelength from 300 to 800 nm using a specially designed IPCE system for solar cells (Zolix Solar cell Scan100), with three electrodes configuration under zero bias versus Ag/AgCl. A 300 W Xe lamp equipped with gratings was used to generate a monochromatic beam. The incident light intensity was calibrated by a standard silicon photodiode.

4.3 Results and discussions

4.3.1 Analysis of the crystal phase, light absorption and morphological properties of the electrode

Figure 4.1(a) illustrates the flowchart of the ALDIER based on the example of TIO obtained by replicating a self-assembled multilayer polystyrene spheres.[170, 203] However, the TiO_2 host structures for the 3-D homogeneous photosensitization can include a wide range of common types, for example, hydrothermal-grown nanorods, anodized nanotubes, and commercial P25 nanoparticles. In the first step, the host is coated with a layer of ZnO of tunable thicknesses using ALD. The second step is the ion exchange reaction. In this process the ALD ZnO layer serves as the sacrificial reactant which transforms first into ZnSe through anion exchange with the Se^{2-} precursor and then to the

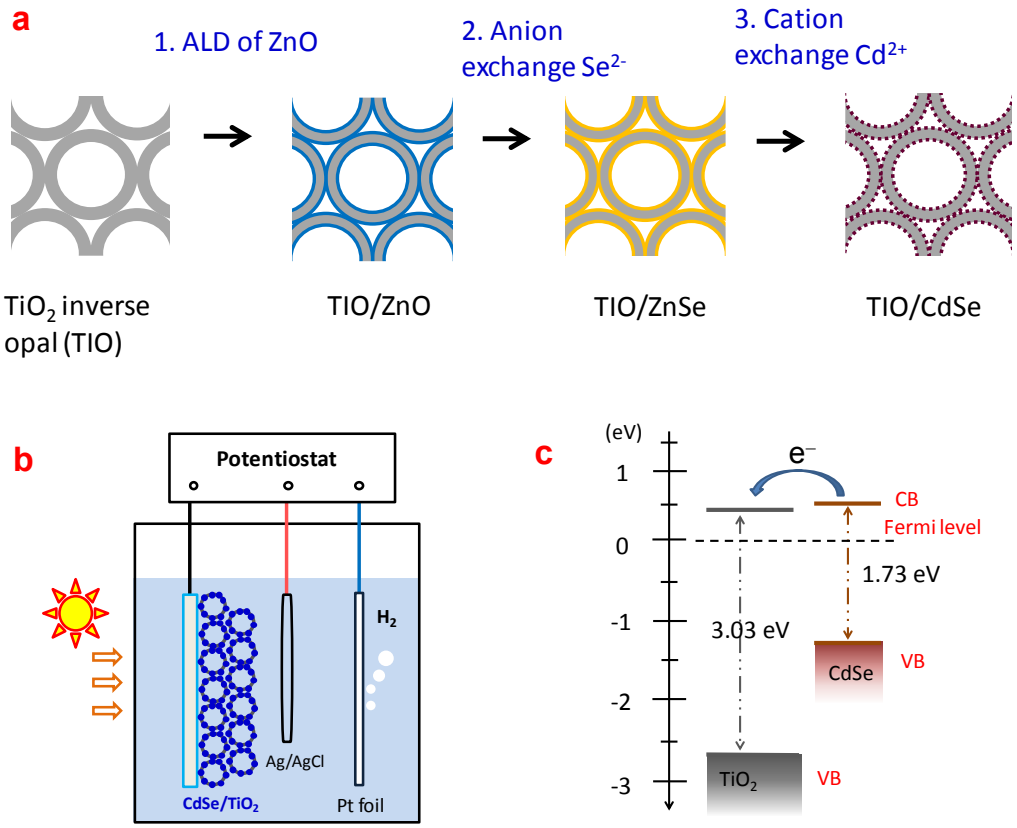

Figure 4.1 *Sensitization of TiO_2 inverse opals photoelectrochemical anode by ALDIER.* ***(a)*** *Schematics of the ALDIER process for uniform QD photosensitization of TiO_2 inverse opals (TIO). Step 1: coating the TIO with ALD ZnO layer. Step 2: anion exchange reaction converting the initial ZnO layer to ZnSe. Step 3: cation exchange reaction converting the intermediate ZnSe to CdSe.* ***(b)*** *Schematics of the photoelectrochemical cell: The as prepared nanostructure electrodes serve as the anode, saturated Ag/AgCl as the reference electrode and the Pt foil as counter electrode for hydrogen evolution.* ***(c)*** *Electron energy levels of TiO_2 and CdSe. The photogenerated electrons within CdSe will be transferred to TiO_2, while the holes (not drawn) will be scavenged by the Na_2SO_3 + Na_2S electrolyte solution. CB: conduction band. VB: valence band.*

final CdSe via cation exchange with Cd^{2+} source.[201] The ion exchange reaction is based on the solubility product constant (K_{sp}) of the material. As the constant of ZnO ($K_{sp} = 6.8 \times 10^{-17}$) is much larger than ZnSe (3.6×10^{-26}), ZnO can be converted into ZnSe by anion exchange reaction with Se^{2-} anions. With the same principle, ZnSe can be further exchanged into CdSe (6.31×10^{-36}).

The same process could result in CdS and PbSe if the anion exchange precursor is S^{2-} and the cation exchange precursor is Pb^{2+}, respectively. Due to the high conformity of the ALD ZnO layer,[204] this simple two-step ALDIER process can be utilized for homogeneous coating of photoactive CdS, CdSe, PbS, or PbSe nanoparticles onto a wide range of complex and high-aspect-ratio substrates. Furthermore, as the thickness of the ZnO seed layer is precisely tunable by ALD cycles, the self-limiting ion exchange reaction will thus lead to different size and coverage of the final sensitizer nanoparticles.

The sensitized TIO will be tested as the PEC photoanode in a three-electrode system for hydrogen generation. Figure 4.1(b) shows the diagram of the PEC cell where a piece of Pt foil was used as the cathode. H_2 gas bubbles are generated on the cathode through the water reduction reaction $2H^+ + 2e \rightarrow H_2$, whereas the holes are scavenged by the sulfide electrolyte. As CdSe has a wider light absorption range and better conduction band edge alignment with TiO_2 than ZnSe, the photocurrent level of TiO_2/CdSe is much higher than TiO_2/ZnSe, as have been reported in previous work.[201] Thus the following the discussion will be made to CdSe photosensitizer on TIO.

The composition transformation from ZnO to CdSe is confirmed using X-ray diffractometer, see Figure 4.2(a). The blue solid lines are the calculated XRD peaks for Anatase TiO_2 (PDF#21-1272), and the green dashed lines are the calculated XRD peaks for SnO_2 (PDF#41-1445). All the diffraction peaks of TIO structure on FTO correlate well with the calculated positions. The

diffraction peaks of ZnO (PDF#36-1451) appear only for the TIO samples after ZnO deposition by ALD. After the first step anion exchange reaction, the ZnSe peaks (PDF#37-1463) can be detected while the ZnO peaks disappear, implying that the ALD ZnO layer is totally converted to ZnSe. After the complete exchange reaction, the peaks can be indexed to hexagonal CdSe (PDF#08-0459). The peak intensities of the CdSe increase from the 60-cycle sample to 120-cycle one, in accordance with the increased loading of CdSe.

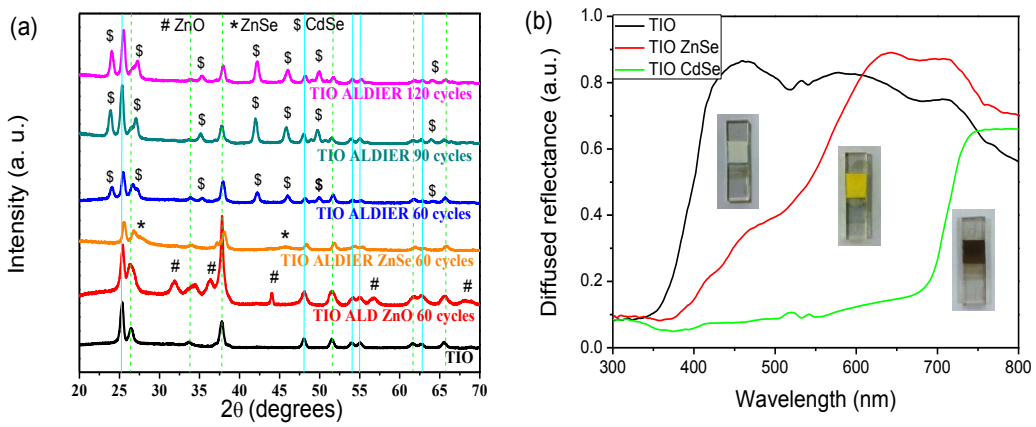

Figure 4.2 *Composition transformations.* ***(a)*** *XRD patterns of pristine TIO and the derived structures after ALD and ion exchange reactions. The green dashed lines indicate the peaks of FTO, and the blue solid lines indicate peaks of anatase TiO_2.* ***(b)*** *UV-vis diffuse reflection spectra of three photoanode samples. TIO: pure TiO_2 inverse opal. TIO/ZnSe: ZnSe-coated TiO_2 inverse opal after the anion exchange reaction. TIO/CdSe: CdSe-coated TiO_2 inverse opal after the cation exchange reaction. Insets are the photographs of the samples on FTO-coated glass.*

UV-visible diffuse reflection spectra are recorded to reveal the light harvesting capability of pristine TIO, ZnSe and CdSe sensitized TIO photoanodes (results shown in Figure 4.2(b)). Pristine TIO can only absorb light with a wavelength beyond 400 nm. The absorption range broadens up to 550 nm after the

exchange to ZnSe, and 700 nm after the final exchange into CdSe, consistent with their bandgap. The composition change after anion and cation exchange

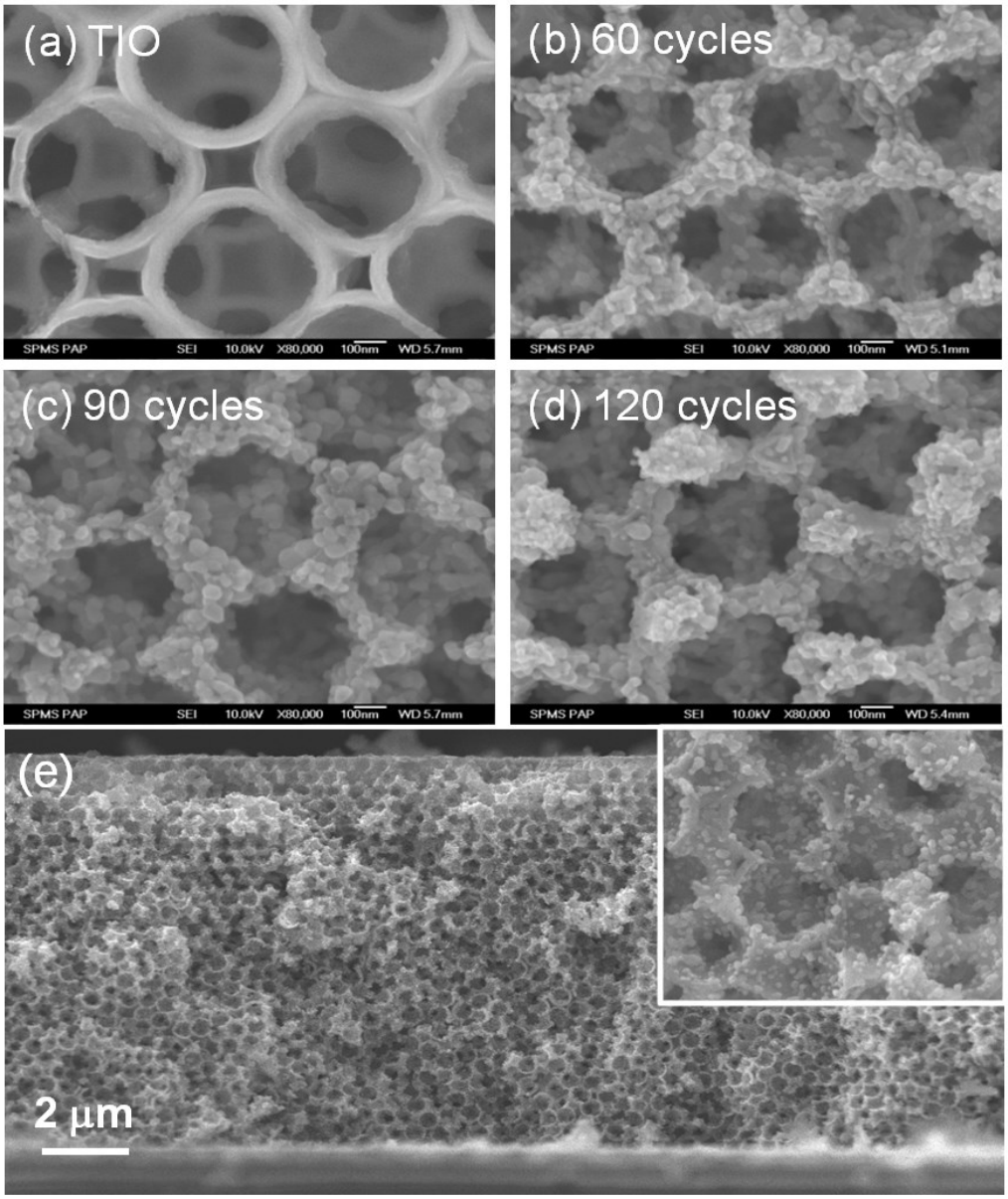

Figure 4.3 *SEM characterization.* ***(a)*** *Top view of pristine TiO_2 inverse opal.* ***(b-d)*** *Top view images of the ALDIER samples, where the CdSe layers were converted from the ZnO starting layers obtained by using 60, 90, and 120 ALD cycles, respectively.* ***(e)*** *Side view of the entire cross section of the photoanode in* ***(b)*** *showing the uniform sensitization from top to the bottom. Inset: enlarged view of part of the cross section.*

reactions and the light harvesting ability can also be revealed from the photographs of the samples in Figure 4.2(b) inset. The samples with CdSe

coating appear dark brown compared with the bright yellow colour of ZnSe and white pristine TIO.

Morphologies of the photoanodes prior to and after the ion exchange reactions with different ALD ZnO cycles are shown by the SEM images in Figure 4.3. The original TIO surfaces are smooth. After ALDIER, the open surfaces are coated with a granular layer of CdSe. The SEM image in Figure 4.3(e) provides an entire cross-sectional view of the structure with 60 ALD cycles. Clearly the ion exchange reactions proceed along the whole depth of 10

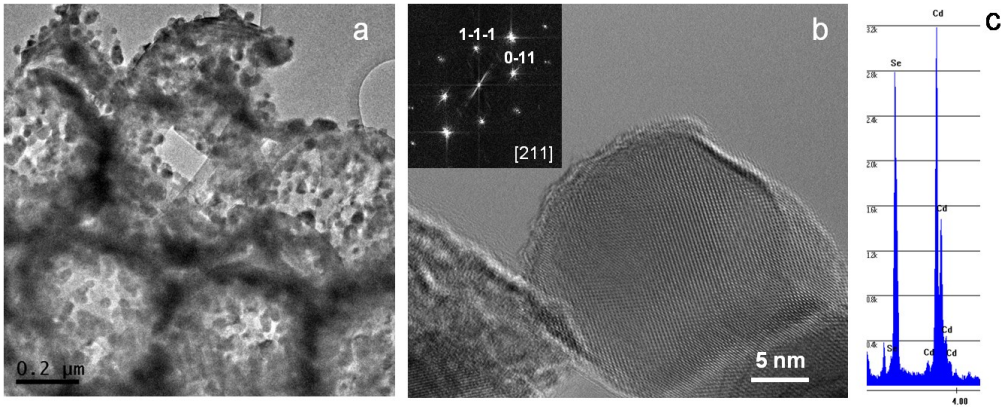

Figure 4.4 *TEM characterization.* ***(a)*** *Low-magnification TEM image of the CdSe nanoparticle-sensitized TiO_2 inverse opal.* ***(b)*** *Atomic-scale TEM image of one CdSe nanoparticle. Inset is the corresponding fast Fourier transformation pattern.* ***(c)*** *X-ray energy dispersion spectrum (EDS) recorded from the CdSe nanoparticle in (b).*

μm, owing to the effectiveness of ALD in creating conformal coatings on the surfaces of high aspect-ratio nanostructures. The morphology is further characterized using transmission electron microscopy (TEM). Figure 4.4(a) provides clear evidence of the attachment of nanoparticles on the available surfaces of the pores of TIO. High-resolution TEM image in Figure 4.4(b)

shows that the particles are crystalline, and the lattice spacing can be indexed into (0-11) and (1-1-1) planes of hexagonal CdSe. Pure elements of Cd and Se are confirmed by the X-ray energy dispersion spectrum shown in Figure 4.4(c).

4.3.2 Investigation and understanding of the PEC performance of the electrodes

The PEC performance of the ALDIER photoanodes is investigated by conducting the current density vs potential (*J-V*) measurements under the dark and simulated sunlight illumination (AM 1.5) in the three-electrode cell configuration (Figure 4.1(b)). First of all, all the electrodes are fabricated from 500 nm polystyrene spheres and have the same height of 10 μm. For ion exchange reaction, temperature is a critical parameter that affects the size and morphology of the resulting sensitizer layer. Hence the first step is to optimize the reaction temperature for CdSe exchange reaction while keeping ALD ZnO thickness the same (~10 nm by 60 ALD cycles).

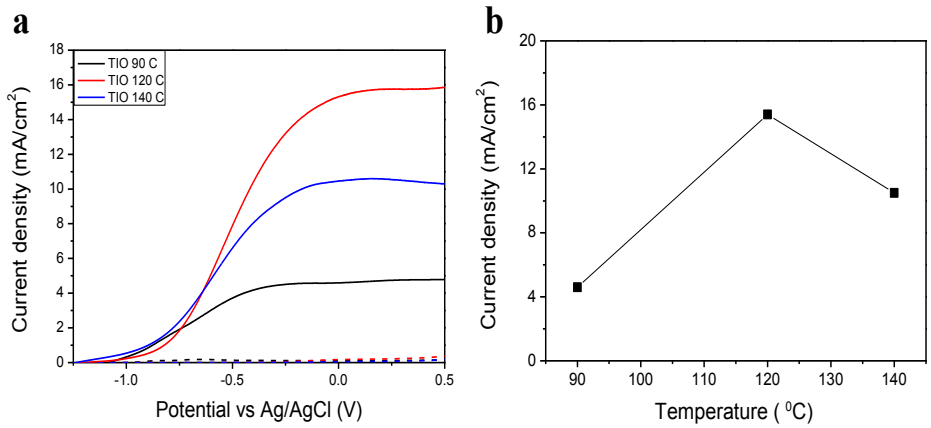

Figure 4.5 *Effect of ion exchange reaction temperature to the photocurrent.*

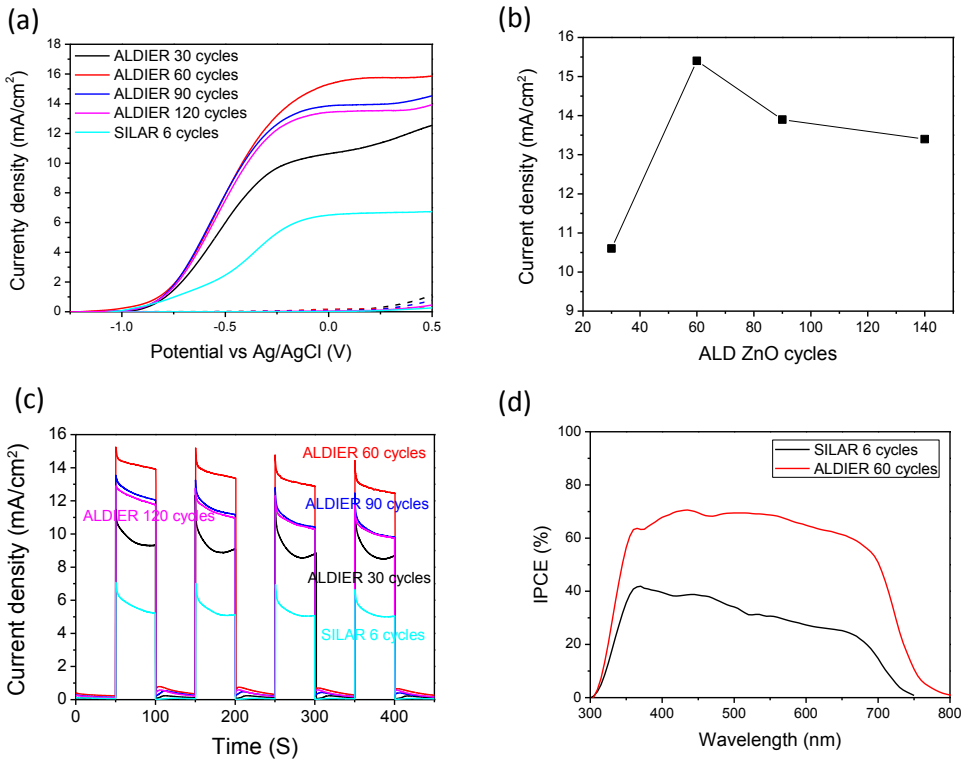

Figure 4.6 *The photoelectrochemical properties of the ALDIER TiO_2 inverse opal photoanodes.* ***(a)*** *Linear sweep voltammagrams (J-V curves) under dark condition and AM1.5 light illumination for samples by ALDIER technique with different ALD cycles, and one by 6 SILAR cycles.* ***(b)*** *Plot of the photocurrent density at zero bias in* ***(a)*** *versus the ALD ZnO cycle.* ***(c)*** *Photocurrent versus time tests (J-t curves) under chopped light illumination (light/dark cycles of 50 s) at a fixed bias of 0 V vs Ag/AgCl.* ***(d)*** *IPCE profile of the ALDIER photoanode with 60 ALD cycles. For comparison, the corresponding data of the optimized SILAR anode (6 cycles CdSe) are also shown.*

As shown in Figure 4.5, the electrode obtained from the reaction at 120 °C exhibits the highest photocurrent level (15.7 mA/cm^2 at zero bias vs Ag/AgCl) compared to those from reactions at 90 °C (4.6 mA/cm^2) and 140 °C (10.5 mA/cm^2). Therefore, for the rest experiments, the reaction temperature is fixed at 120 °C. Figure 4.6 (a) presents the *J-V* curves of TIO/CdSe anodes obtained from different cycles of ALD ZnO. All the photoanodes have negligible dark current while pronounced current densities, above 10 mA/cm^2, upon illumination. This implies an efficient light harvesting by the sensitizers

(see also IPCE below) and charge separation at the TiO_2 and CdSe interface rendered by the type-II band alignment. All the samples show similar onset potentials (−1.0 V vs Ag/AgCl), as a result of similar surface flat bands. The photocurrents saturate with increasing bias voltage, indicating good electrical conductivity of the TIO/CdSe and the good contact with the FTO.

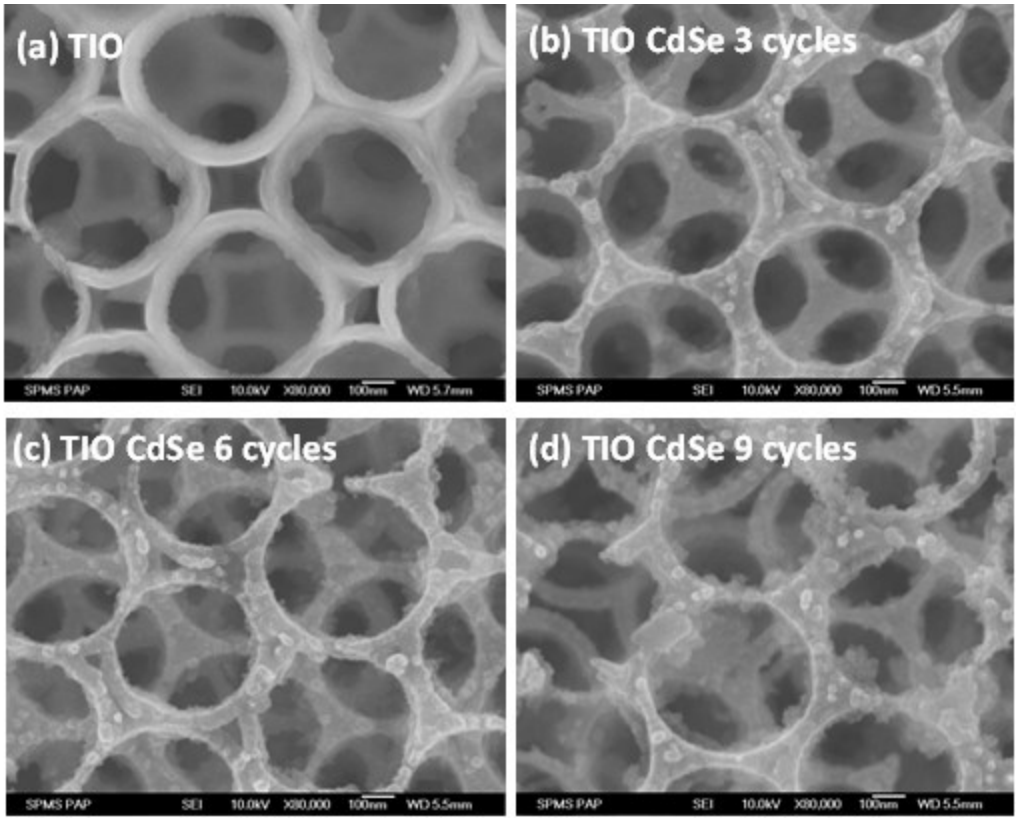

Figure 4.7 *SEM images of the CdSe-coated TiO_2 structure by the commonly used successive ionic layer adsorption and reaction (SILAR) method. The cycle number denotes the number of SILAR steps.*

We now discuss the effect of ALD ZnO thickness. Figure 4.6(a)-(c) show that the sample from 60 ALD cycles gives the highest photocurrent; further increasing in the ALD cycles to 90 and 120 slightly brings the photocurrent down to ~13 mA/cm^2. The lowering of the current with higher ALD cycles might originate from adverse effects such as increased carrier recombination

within the thicker CdSe layers. It is noted that a thicker ALD ZnO layer corresponds to larger CdSe nanoparticle size. Photocurrent versus time (*J*-t) curves in Figure 4.6(c) show that all the electrodes have good photoresponse and relatively good stability. For comparison, a series of control samples of the same height are sensitized with CdSe via the SILAR method and measured under the same condition (see SEM images in Figure 4.7).

Among samples with 3, 6, and 9 SILAR cycles, the highest photocurrent is ~6.5 mA/cm^2 obtained from the 6-cycle SILAR sample (also presented in Figure 4.6(a)). The CdSe nanoparticles appear to have a lower coverage than that by ALDIER based on SEM inspection. It is noteworthy that the photocurrent level obtained from our ALDIER electrode is very high among nano TiO_2 photoanodes, even higher than the previously reported TiO_2 nanoparticle electrode with CdS and CdSe co-sensitization (14.9 mA/cm^2).[205]

While the voltammagram *J-V* curves show the overall PEC performance of the photoanode, the insight of the photocarrier generation can be obtained by studying the incident-photon-to-current conversion efficiency (IPCE), which allows the evaluation of the wavelength-dependent light harvesting efficiency. The IPCE profile from the 60-ALD cycle sample is shown in Figure 4.6(d). One can see that, within the test range of 300−800 nm wavelength, a strong and nearly constant photoresponse is observed in the visible region from 305 to 750

nm; the efficiency lies between 60–70% with a nearly flat profile. In contrast, the IPCE of the photoanode by SILAR sensitization is significantly lower, probably due to the aforementioned lower coverage of CdSe and the non-uniform sensitization, in correlation with its higher light reflectivity.

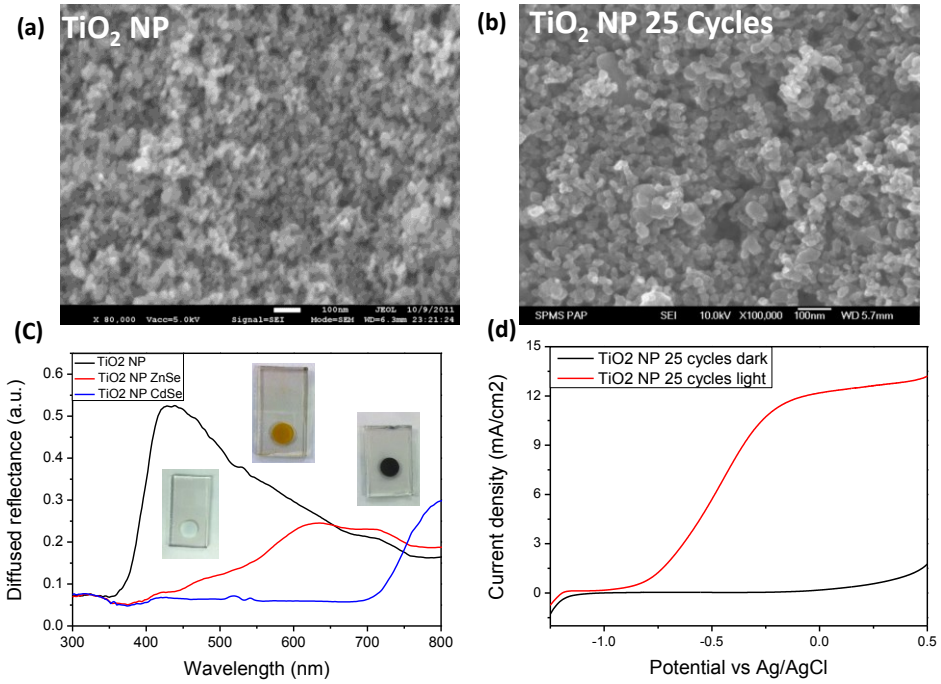

Figure 4.8 *Application of the ALDIER method to TiO_2 P25 nanoparticles film.* ***(a)*** *SEM image of the pristine nanparticle film,* ***(b)*** *SEM image of the film after the CdSe coating by ALDIER.* ***(c)*** *UV-vis diffuse reflection spectra. The corresponding photographs of the sample are shown in inset.* ***(d)*** *J-V curve of the sample after SILIAR with 25 ALD ZnO cycles.*

The significant performance enhancement of ALDIER anodes compared with SILAR ones implies the superior quality of the sensitizer coating by this simple yet powerful ALD plus ion exchange reaction technique, which results in an excellent penetration depth, uniform coverage and increased amount of loading of the sensitizers. As a result, both the light harvesting ability and the charge transfer process would be enhanced. It is envisaged that the performance

could be further improved by ZnS passivation as described before [206] or by doping of the CdSe which is recently developed by Kamat.[207]

To generalize this ALDIER technique to various nanostructures, same experiments are also conducted to TiO_2 nanorod arrays and nanoparticle films (see Figure 4.8 and Figure 4.9). Shown in Figure S6 are the results from the commercial P25 nanoparticle film. Clearly, one can also see the very low diffusive reflectance and high photocurrent up to 12 mA/cm^2. The detailed study of the interface between CdSe and TiO_2 by the HRTEM and the inner charge transfer process by ultrafast optical spectroscopy is currently underway to provide a comprehensive physical understanding.

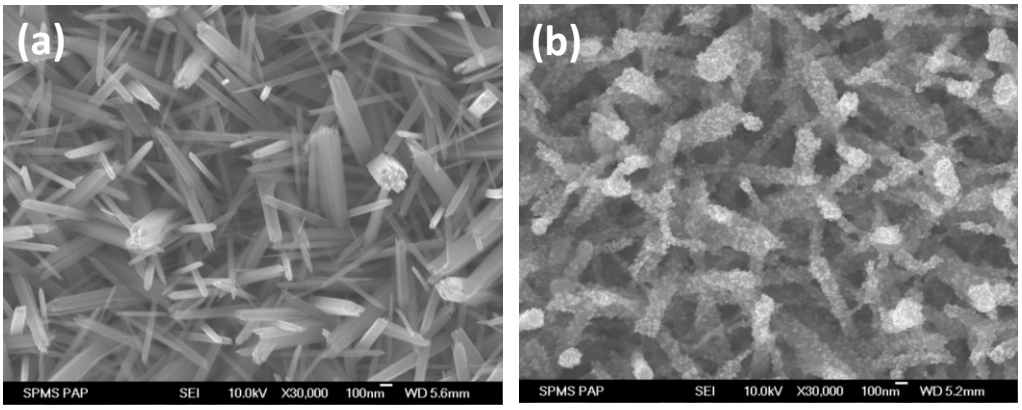

Figure 4.9 *SEM images of the CdSe-coated TiO_2 nanorods by ALDIER.* ***(a)****Pristine nanorods,* ***(b)*** *after the coating.*

4.4 Conclusions

In conclusion, we have developed a new strategy to coat TiO_2 nanostructures with a homogeneous layer of CdSe photosensitizer based on ion

exchange reaction using ALD ZnO layer as sacrificial template. With the optimized ion exchange reaction temperature and ALD ZnO thickness, the highest photocurrent for the TIO/CdSe electrode reaches 15.7 mA/cm^2 at zero bias versus Ag/AgCl, which is the highest value among TiO_2-based photoelectrochemical cells for hydrogen generation. The enhancement of the performance is mainly attributed to the larger sensitizer loading quantity and better sensitizer coating quality. This sensitization method can be generalized to other sensitizers like CdS, PbS and PbSe, that are currently being followed in the same group. While only PEC application is demonstrated in this case study of the ALDIER method, there is in principle no limit for it to be extended to the other applications, such as light emitting diode (LED) and photodetectors.

Chapter 5 Final Conclusions, Comments and Recommendations

5.1 Final conclusions of the thesis

The work conducted in this thesis aims at improving the efficiency of TiO_2 for PEC hydrogen generation. In chapter 1, a general introduction and review of recent efforts in using TiO_2 for hydrogen generation is conducted.

The chapter 2 is the start and foundation of the whole thesis. In this part, the properties and performances of different sensitizers were systematically studied and compared. The TiO_2 nanorod array was chosen as the model TiO_2 nanostructure due to its facial preparation method. The sensitizers were deposited by CVD method, which could provide high loading amount and high crystallinity of the sensitizer. In the first part, the loading of the CdS on TiO_2 nanorod array was studied by tuning the deposition time. It was found that the CdS formed tiny nanoparticles on the tips of TiO_2 nanorod at the initial deposition stage. The CdS nanoparticles grew into nanorods as the depsotion time increasing, and further grew into nanobundles. By using CdS and CdSe precursors together, the CdSeS alloy samples could be made, and the band edge positions could be tuned by varying the composition between the CdS and CdSe. In PEC hydrogen generation, the CdSe sensitized TiO_2 nanorod array shows the highest photocurrent level, up to 9 mA/cm^2 at 0V vs Ag/AgCl. However, it is highly unstable, the photocurrent degrades quickly below both the CdS and

CdSeS sensitized samples in just minutes. Though the CdS sensitized sample shows the lowest photocurrent, around 5.8 mA/cm^2, it is highly stable without degradation during the test. The photocurrent level and stability of the CdSeS sensitized sample is between the CdS and CdSe. Thus, In terms of the photocurrent level and stability, the CdSeS sensitized sample would be a favorable choice.

The following two chapters are the two approaches to increase the efficiency of the sensitized TiO_2 nanostructure for PEC hydrogen generation. As there are two parts for the heterostructures, the sensitizer and the TiO_2 scaffold. The strategy can be focused on either the sensitizer or TiO_2 scaffold. Chapter 3 is focused on tailoring the TiO_2 scaffold structure. Compared to the TiO_2 nanorod array, TiO_2 inverse opal has higher surface area and unique three dimensional structure. However, compared to the TiO_2 nanoparticles, the surface area of TiO_2 inverse opal is still quite low. The surface area can be increased by further growth of nanowires inside. We first tried TiO_2 nanowires, as they would easily form bundles into big nanorod, the growth inside the inverse opal is quite challenging. While for ZnO, the growth is facile and band edge position is almost the same as TiO_2 which favors the charge transport. With the same concept to increase the surface area, we grew ZnO nanowires inside the TiO_2 inverse opal, and it is quite successful. The density and length of ZnO nanowires could be tuned by varying the growth time. We have compared hydrogen generation ability of the samples with same thickness of

pure TiO_2 inverse opal, ZnO nanowire arrays and hierarchical three dimensional structures with CdS sensitization. It was found that the 3D hierarchical structure shows highest photocurrent, which is roughly the sum of the TiO_2 inverse opal and ZnO nanowire array samples.

Chapter 4 is focused on the sensitizer part. There are various methods for the sensitizer deposition, such as chemical bath deposition (CBD), chemical vapour depositon (CVD), successive ionic layer adsorption and reaction (SILAR) and electrochemical deposition (ED). However, deposition of the sensitizer into the complex 3D nanostructures, especially the high aspect ratio samples is still a challenge. ALD is powerful thin film deposition technique, which could provide precise thickness control at the angstrom or monolayer level and deposition on high aspect ratio nanostructures with excellent step coverage. If ALD could be used to deposit the sensitizers, the penetration challenge of the sensitizers will be solved. However, direct deposition of the sensitizer by ALD is limited by the precursors and the harsh conditions. ZnO can be exchanged into ZnS and ZnSe by anion exchange, and CdS, CdSe, PbS, PbSe and Cu_2S et al could be generated through further cation exchange. Most importantly, ZnO can be well deposited by the ALD. By combining the ALD and the ion exchange reaction together, various sensitizers can be coated onto TiO_2 nanostructures with high quality. We choose TiO_2 inverse opal samples as the model structure to demonstrate this concept, and the results show that this

technique indeed outperform the conventional SILAR method by nearly double the photocurrent.

In summary, chemical vapor deposition method of CdS and CdSe gives better performance compared to solution method due to high crystallinity of the material, which is critical for the charge transport. However, it is difficult to control and expensive due to the high temperature and vacuum process. TiO_2 nanrod has a better charge carrier transport property compared to TiO_2 particle and TiO_2 inverse opal film due to its one dimensional structure and single crystal property. But it suffers from low surface area, TiO_2 inverse opal gives higher performance after sensitization mainly due to higher amount of sensitizer loading. Based on all these factors together, combing the nanobush structure fabricated in chapter 3 and the ALDIER sensitization method developed in chapter 4 might give the best performance.

5.2 Comments

Though CdS and CdSe sensitized electrodes show high efficiencies in PEC hydrogen generation, they cannot be counted as pure water splitting, because CdS and CdSe have the stability issue during the water oxidation process. The decomposition potentials of the CdS and CdSe are more favorable than the water oxidation. Thus, to stabilize the electrode, sacrificial agent has to be used in the electrolyte. Actually, CdS is the most ideal semiconductor for water splitting, due to its relatively small band gap (2.4 eV) and suitable band edge

positions, with conduction band level enough to reduce water and the valence band sufficient to oxidize water. Thus, a lot of studies have been conducted in the 1980s.[208-213]The photocorrosion of the CdS can be categorized in two conditions, with O_2 or without.[208] In the absence of O_2, the corrosion is mainly dominated by the following reaction,

$$2h^+ + CdS \xrightarrow{hv} Cd^{2+} + S$$

In the presence of O_2, the corrosion is through the following reaction.

$$CdS + 4h^+ + 2H_2O + O_2 \rightarrow Cd^{2+} + SO_4^{2-} + 4H^+$$

To solve the stability issue, various electrolytes have been developed, mainly by adding the reducing agents, such as $Fe(CN)_6^{4-}$, I^{1-}, Fe^{II}-EDTA complex, S^{2-}, SO_3^{2-}, $S_2O_3^{2-}$ or their mixtures.[208] The sulfide (S^{2-}) and sulfite (SO_3^{2-}) mixtures are the most frequently used sacrificial agents.[214] These agents can be oxidized through two electron processes, or even one electron process to form the intermediate radical, which are more accessible compared to the four electron process to oxidize water. By adding the S^{2-} agent into the electrolyte, the dissolved Cd^{2+} can react with the S^{2-} to reform CdS.[129] However, S^{2-} will from S_2^{2-} oxidant through the following reaction,

$$2S^{2-} + 2h^+ \rightarrow S_2^{2-}$$

which is more favorable than proton reduction and the product of this reaction presents a yellowish color, blocking the light absorption of CdS. This problem can be avoided by adding SO_3^{2-} into the electrolyte.[129]

$$S_2^{2-} + SO_3^{2-} \rightarrow S_2O_3^{2-} + S^{2-}$$

$S_2O_3^{2-}$ is transparent and soluble in water, and can transform into SO_3^{2-} through the following reaction

$$S_2O_3^{2-} + 3H_2O + 4h^+ \rightarrow 2SO_3^{2-} + 6H^+$$

SO_3^{2-} can be oxidized into SO_4^{2-} through reaction

$$2OH^- + SO_3^{2-} \rightarrow SO_4^{2-} + H_2O$$

There may be also other reactions in the electrolyte.[214] As the cathodic reaction is H_2 generation, the overall reaction could be written as

$$S^{2-} + SO_3^{2-} + 5H_2O \rightarrow 5H_2 + 2SO_4^{2-}$$

rather than water splitting reaction,

$$2H_2O \rightarrow 2H_2 + O_2$$

There is often misunderstanding of the efficiency calculation, especially for the beginners. The equation for the efficiency calculation discussed in the introduction part is for pure water splitting reaction, without adding any sacrificial agents.

$$\eta = \frac{(1.23 - V_{bias}) \times J}{P}$$

First, in the presence of sacrificial agents, the efficiency calculated based on the above equation will be greatly exaggerated. 1.23 V is based on the Gibbs free energy change for water splitting reaction, by adding sulfide and sulfite into the electrolyte, this potential will be greatly reduced. Second, the applied bias

should be based on the two electrode configuration, rather than the commonly used three electrode configuration.[31] The calculation based on the bias referred to the reference electrode will lead to an overestimated efficiency, because the potential between the working electrode and the counter electrode is larger.

In order to calculate the efficiency accurately, the H_2 generated should be quantified by gas chromatography. Simply measuring the photocurrent is not enough, because there might be side reactions, such as the corrosion of the electrode, which will also contribute to the current. The addition of sacrificial agents in the electrolyte can be reflected by the volume ratio between generated H_2 and O_2.

Though sulfur compounds are greatly reserved on earth and also often produced in large quantities from chemical industry such as natural gas utilization, hydrodesulphurization of crude oil and coal chemistry,[209, 215] the usage of the sulfur compounds as sacrificial agents still sets an obstacle for the real application of the systems studied in the thesis. This might be avoided through the development of the passivation method to stabilize the electrode. Corrosion is a common issue for the semiconductors whose oxidation potential is more cathodic than water oxidation or reduction potential more anodic than water reduction. To solve this problem, passivation of the electrode surface with stable semiconductors can be employed. It should be noted that the passivation layer should not block the minority carrier transport to the

electrolyte. Specifically, for photocathode, the passivation layer should be the electron transport layer, and for photoanode, the passivation layer should be the hole transport layer. For example, there are two recent reports about the passivation of Cu_2O photocathode and Si photoanode, respectively.[216, 217]

5.3 Recommendations

5.3.1 Boost the efficiency by catalyst decoration

According to the Gibbs free energy, 1.23 eV is just enough for water splitting reaction. However, due to the limitation of reaction kinetics and other factors, overpotentials are necessary to give a reasonable current. Adding catalyst on the electrode could reduce the overpotential by improving the reaction kinetics and changing the energetics of the electron transfer process. Catalysts are usually deposited on the surface of the electrode forming a thin layer. This layer has to be thin in order not to block the light absorption of the electrode. Besides improving the reaction kinetics, the catalyst layer may also increase the stability of the electrode by functioning as a passivation layer.

5.3.2 Building unassisted hydrogen generation device

The current study with three electrode configuration for characterizing the PEC property of the electrode is often with external bias. In the ideal case, the device should function like natural plant when put into the water with light illumination, the water will split into H_2 and O_2 spontaneously. This has

stringent requirement of the material. The band edge positions of the semiconductor should straddle the water splitting reaction potentials with enough overpotential. Only very few materials can fulfill this requirement and have demonstrated the unassisted water splitting with a single junction, such as $SrTiO_3$ and $KTaO_4$.[23] CdS has perfect band edge positions, if the catalyst is used, the unassisted water splitting could be realized. Early in 1987, Allen J. Bard has demonstrated the unassisted water splitting with the bipolar CdSe/CoS electrode.[213] Recently, Juan Bisquert group also demonstrated unassisted water splitting with the CdS and PbS co-sensitized TiO_2 electrode.[218] Future efforts are needed to engineer the electrode structure to make highly efficient unassisted water splitting device.

In the case when an external bias is required for the electrode, tandem cell configuration can be used to give enough overpotential.[7] The electrode can be connected with the conventional solar cell to provide the bias, such as the Si solar cell or dye sensitized solar cell.

5.3.3 Improve the stability of the electrode

Besides efficiency, stability is also an important step towards real application. In 1998, hydrogen generation device with efficiency of 12.4% has already been developed.[219] However, the high fabrication cost of the electrode and the stability issue hinder the real application of the device. The device uses GaAs and $GaInP_2$ tandem structure, which is far more expensive

compared to the electrodes developed in this thesis. Though we have achieved unprecedented photocurrent level by modifying the fabrication method of the electrode, we haven't solved the stability issue of the electrode. Developing effective passivation method is highly demanded for real application. As there are many well-known high performance materials, such as Si, GaAs and CdSe, that are limited by the stability.

5.3.4 Discovering new materials through theoretical calculation and high throughput experiment

Either highly efficient but unstable or highly stable but inefficient, this is a dilemma for the current known electrode materials. Thus it is highly demanded to discover and synthesize new materials. It is rational to do the theoretical calculations first before experiment. Modeling the device efficiency is also very important. High throughput experimental method to check the PEC properties of the new materials has to be developed.

References

[1] http://www.nrel.gov/ncpv/images/efficiency_chart.jpg.

[2] *International Energy Outlook 2013*, U.S.E.I. Administration, Editor. 2013.

[3] Roel van de Krol, M.G., *Photoelectrochemical Hydrogen Production*. 2012, New York: Springer.

[4] Cho, I.S., et al., *Branched TiO2 Nanorods for Photoelectrochemical Hydrogen Production.* Nano Letters, 2011. **11**(11): p. 4978-4984.

[5] Liu, B., et al., *Large-Scale Synthesis of Transition-Metal-Doped TiO2 Nanowires with Controllable Overpotential.* Journal of the American Chemical Society, 2013. **135**(27): p. 9995-9998.

[6] Liu, C., N.P. Dasgupta, and P. Yang, *Semiconductor Nanowires for Artificial Photosynthesis.* Chemistry of Materials, 2013: p. 131002125040005.

[7] Prévot, M.S. and K. Sivula, *Photoelectrochemical Tandem Cells for Solar Water Splitting.* The Journal of Physical Chemistry C, 2013. **117**(35): p. 17879-17893.

[8] Walter, M.G., et al., *Solar Water Splitting Cells.* Chemical Reviews, 2010. **110**(11): p. 6446-6473.

[9] Shafiee, S. and E. Topal, *When will fossil fuel reserves be diminished?* Energy Policy, 2009. **37**(1): p. 181-189.

[10] *http://en.wikipedia.org/wiki/Fukushima_Daiichi_nuclear_disaster*.

[11] B. Metz, O.R.D., P.R. Bosch, R. Dave, L.A. Meyer *Contribution of Working Group III to the Fourth Assessment Report of the Intergovernmental Panel on Climate Change*. 2007, Cambridge, United Kingdom and New York, NY, USA.: Cambridge University Press.

[12] Lewis, N.S. and D.G. Nocera, *Powering the planet: Chemical challenges in solar energy utilization.* Proceedings of the National Academy of Sciences, 2006. **103**(43): p. 15729-15735.

[13] Yinghao Chu, P.M. *Review and Comparison of Different Solar Energy Technologies* 2011.

[14] http://www.nrel.gov/csp/solarpaces/project_detail.cfm/projectID=3.

[15] Burschka, J., et al., *Sequential deposition as a route to high-performance perovskite-sensitized solar cells.* Nature, 2013. **499**(7458): p. 316-319.

[16] Liu, M., M.B. Johnston, and H.J. Snaith, *Efficient planar heterojunction perovskite solar cells by vapour deposition.* Nature, 2013. **501**(7467): p. 395-398.

[17] Armand, M. and J.M. Tarascon, *Building better batteries.* Nature, 2008. **451**(7179): p. 652-657.

[18] Bruce, P.G., et al., *Li-O2 and Li-S batteries with high energy storage.* Nat Mater, 2012. **11**(1): p. 19-29.

[19] Ponce de León, C., et al., *Redox flow cells for energy conversion.* Journal of Power Sources, 2006. **160**(1): p. 716-732.

[20] Gray, H.B., *Powering the planet with solar fuel.* Nat Chem, 2009. **1**(1): p. 7-7.

[21] Bard, A.J. and M.A. Fox, *Artificial Photosynthesis: Solar Splitting of Water to Hydrogen and Oxygen.* Accounts of Chemical Research, 1995. **28**(3): p. 141-145.

[22] Blankenship, R.E., et al., *Comparing photosynthetic and photovoltaic efficiencies and recognizing the potential for improvement.* Science, 2011. **332**(6031): p. 805-9.

[23] Vayssieres, L., *On solar hydrogen & nanotechnology*. 2009, Singapore: John Wiley & Sons (Asia) Pte Ltd.

[24] Craig A. Grimes, O.K.V., Sudhir Ranjan *Light, Water, Hydrogen The Solar Generation of Hydrogen by Water Photoelectrolysis* 2008, New York: Springer Science.

[25] Dutta, S., *Technology assessment of advanced electrolytic hydrogen production.* International Journal of Hydrogen Energy, 1990. **15**(6): p. 379-386.

[26] LeRoy, R.L., *Industrial water electrolysis: Present and future.* International Journal of Hydrogen Energy, 1983. **8**(6): p. 401-417.

[27] Kittel, C., *Introduction to Solid State Physics* 2005: Wiley: New York.

[28] Nozik, A.J. and R. Memming, *Physical Chemistry of Semiconductor−Liquid Interfaces.* The Journal of Physical Chemistry, 1996. **100**(31): p. 13061-13078.

[29] Reiss, H., *The Fermi level and the redox potential.* The Journal of Physical Chemistry, 1985. **89**(18): p. 3783-3791.

[30] Koval, C.A. and J.N. Howard, *Electron transfer at semiconductor electrode-liquid electrolyte interfaces.* Chemical Reviews, 1992. **92**(3): p. 411-433.

[31] Zhebo Chen, H.N.D., Eric Miller, *Photoelectrochemical Water Splitting Standards, Experimental Methods, and Protocols*. 2013, New York Springer

[32] Bott, A.W., *Electrochemistry of Semiconductors.* Current Separations, 1998. **3**(17): p. 87-91.

[33] Gelderman, K., L. Lee, and S.W. Donne, *Flat-Band Potential of a Semiconductor: Using the Mott–Schottky Equation.* Journal of Chemical Education, 2007. **84**(4): p. 685.

[34] Hu, S., et al., *An analysis of the optimal band gaps of light absorbers in integrated tandem photoelectrochemical water-splitting systems.* Energy & Environmental Science, 2013. **6**(10): p. 2984-2993.

[35] Reichman, J., *The current‐voltage characteristics of semiconductor‐electrolyte junction photovoltaic cells.* Applied Physics Letters, 1980. **36**(7): p. 574-577.

[36] Fujishima, A. and K. Honda, *Electrochemical Photolysis of Water at a Semiconductor Electrode.* Nature, 1972. **238**(5358): p. 37-38.

[37] Ni, M., et al., *A review and recent developments in photocatalytic water-splitting using for hydrogen production.* Renewable and Sustainable Energy Reviews, 2007. **11**(3): p. 401-425.

[38] Gratzel, M., *Photoelectrochemical cells.* Nature, 2001. **414**(6861): p. 338-344.

[39] Choi, W., A. Termin, and M.R. Hoffmann, *The Role of Metal Ion Dopants in Quantum-Sized TiO2: Correlation between Photoreactivity and Charge Carrier Recombination Dynamics.* The Journal of Physical Chemistry, 1994. **98**(51): p. 13669-13679.

[40] Anpo, M., *Use of visible light. Second-generation titanium oxide photocatalysts prepared by the application of an advanced metal ion-implantation method.* Pure and Applied Chemistry, 2000. **72**(9): p. 1787-1792.

[41] Zaleska, A., *Doped-TiO2: A Review.* Recent Patents on Engineering, 2008. **2**(3): p. 157-164.

[42] Dvoranová, D., et al., *Investigations of metal-doped titanium dioxide photocatalysts.* Applied Catalysis B: Environmental, 2002. **37**(2): p. 91-105.

[43] Martin, S.T., C.L. Morrison, and M.R. Hoffmann, *Photochemical Mechanism of Size-Quantized Vanadium-Doped TiO2 Particles.* The Journal of Physical Chemistry, 1994. **98**(51): p. 13695-13704.

[44] Janisch, R., P. Gopal, and N.A. Spaldin, *Transition metal-doped TiO2 and ZnO - present status of the field.* Journal of Physics-Condensed Matter, 2005. **17**(27): p. R657-R689.

[45] Litter, M.I. and J.A. Navío, *Photocatalytic properties of iron-doped titania semiconductors.* Journal of Photochemistry and Photobiology A: Chemistry, 1996. **98**(3): p. 171-181.

[46] Gai, Y., et al., *Design of Narrow-Gap TiO_{2}: A Passivated Codoping Approach for Enhanced Photoelectrochemical Activity.* Physical Review Letters, 2009. **102**(3): p. 036402.

[47] Sato, S., *Photocatalytic activity of NOx-doped TiO2 in the visible light region.* Chemical Physics Letters, 1986. **123**(1–2): p. 126-128.

[48] Asahi, R., et al., *Visible-Light Photocatalysis in Nitrogen-Doped Titanium Oxides.* Science, 2001. **293**(5528): p. 269-271.

[49] Chen, X., et al., *Nanomaterials for renewable energy production and storage.* Chemical Society Reviews, 2012. **41**(23): p. 7909-7937.

[50] Chen, X., et al., *Increasing Solar Absorption for Photocatalysis with Black Hydrogenated Titanium Dioxide Nanocrystals.* Science, 2011. **331**(6018): p. 746-750.

[51] Khan, S.U., M. Al-Shahry, and W.B. Ingler, Jr., *Efficient photochemical water splitting by a chemically modified n-TiO2.* Science, 2002. **297**(5590): p. 2243-5.

[52] Sasikala, R., et al., *Modification of the photocatalytic properties of self doped TiO2 nanoparticles for hydrogen generation using sunlight type radiation.* International Journal of Hydrogen Energy, 2009. **34**(15): p. 6105-6113.

[53] Zuo, F., et al., *Self-Doped Ti3+ Enhanced Photocatalyst for Hydrogen Production under Visible Light.* Journal of the American Chemical Society, 2010. **132**(34): p. 11856-11857.

[54] Omurzak, E., et al., *Synthesis of Blue Amorphous TiO_2 and Ti_nO_{2n-1} by the Impulse Plasma in Liquid.* Journal of Nanoscience and Nanotechnology, 2009. **9**(11): p. 6372-6375.

[55] Yin, W.-J., et al., *Band structure engineering of semiconductors for enhanced photoelectrochemical water splitting: The case of TiO_{2}.* Physical Review B, 2010. **82**(4): p. 045106.

[56] Wang, P., et al., *Optimizing photoelectrochemical properties of TiO_{2} by chemical codoping.* Physical Review B, 2010. **82**(19): p. 193103.

[57] Cho, I.S., et al., *Codoping titanium dioxide nanowires with tungsten and carbon for enhanced photoelectrochemical performance.* Nat Commun, 2013. **4**: p. 1723.

[58] Kubacka, A., M. Fernández-García, and G. Colón, *Advanced Nanoarchitectures for Solar Photocatalytic Applications.* Chemical Reviews, 2011. **112**(3): p. 1555-1614.

[59] Tong, H., et al., *Nano-photocatalytic Materials: Possibilities and Challenges.* Advanced Materials, 2012. **24**(2): p. 229-251.

[60] Trentler, T.J., et al., *Synthesis of TiO2 Nanocrystals by Nonhydrolytic Solution-Based Reactions.* Journal of the American Chemical Society, 1999. **121**(7): p. 1613-1614.

[61] Feng, X., et al., *Vertically Aligned Single Crystal TiO2 Nanowire Arrays Grown Directly on Transparent Conducting Oxide Coated Glass: Synthesis Details and Applications.* Nano Letters, 2008. **8**(11): p. 3781-3786.

[62] Grimes, C.A., *Synthesis and application of highly ordered arrays of TiO2 nanotubes.* Journal of Materials Chemistry, 2007. **17**(15): p. 1451-1457.

[63] Burnside, S.D., et al., *Self-Organization of TiO2 Nanoparticles in Thin Films.* Chemistry of Materials, 1998. **10**(9): p. 2419-2425.

[64] Liu, B. and E.S. Aydil, *Growth of oriented single-crystalline rutile TiO(2) nanorods on transparent conducting substrates for dye-sensitized solar cells.* J Am Chem Soc, 2009. **131**(11): p. 3985-90.

[65] Brus, L.E., *Electron – electron and electron - hole interactions in small semiconductor crystallites: The size dependence of the lowest excited electronic state.* The Journal of Chemical Physics, 1984. **80**(9): p. 4403-4409.

[66] Peng, H., et al., *First-Principles Study on Rutile TiO2 Quantum Dots.* The Journal of Physical Chemistry C, 2008. **112**(36): p. 13964-13969.

[67] Peng, H. and J. Li, *Quantum Confinement and Electronic Properties of Rutile TiO2 Nanowires.* The Journal of Physical Chemistry C, 2008. **112**(51): p. 20241-20245.

[68] Diebold, U., *The surface science of titanium dioxide.* Surface Science Reports, 2003. **48**(5–8): p. 53-229.

[69] Thomas, A.G., et al., *Resonant photoemission of anatase TiO_2 (101) and (001) single crystals.* Physical Review B, 2003. **67**(3): p. 035110.

[70] Thomas, A.G., et al., *Resonant photoemission of anatase TiO_{2} (101) and (001) single crystals.* Physical Review B, 2003. **67**(3): p. 035110.

[71] Gong, X.-Q. and A. Selloni, *Reactivity of Anatase TiO2 Nanoparticles: The Role of the Minority (001) Surface.* The Journal of Physical Chemistry B, 2005. **109**(42): p. 19560-19562.

[72] Herman, G.S., M.R. Sievers, and Y. Gao, *Structure Determination of the Two-Domain (1×4) Anatase TiO_2 (001) Surface.* Physical Review Letters, 2000. **84**(15): p. 3354-3357.

[73] Lazzeri, M., A. Vittadini, and A. Selloni, *Structure and energetics of stoichiometric TiO_{2} anatase surfaces.* Physical Review B, 2001. **63**(15): p. 155409.

[74] Zaban, A., et al., *The Effect of the Preparation Condition of TiO2 Colloids on Their Surface Structures.* The Journal of Physical Chemistry B, 2000. **104**(17): p. 4130-4133.

[75] Jun, Y.-w., et al., *Surfactant-Assisted Elimination of a High Energy Facet as a Means of Controlling the Shapes of TiO2 Nanocrystals.* Journal of the American Chemical Society, 2003. **125**(51): p. 15981-15985.

[76] Yang, H.G., et al., *Anatase TiO2 single crystals with a large percentage of reactive facets.* Nature, 2008. **453**(7195): p. 638-641.

[77] Mor, G.K., et al., *Enhanced Photocleavage of Water Using Titania Nanotube Arrays.* Nano Letters, 2004. **5**(1): p. 191-195.

[78] Hwang, Y.J., et al., *Photoelectrochemical Properties of TiO2 Nanowire Arrays: A Study of the Dependence on Length and Atomic Layer Deposition Coating.* ACS Nano, 2012. **6**(6): p. 5060-5069.

[79] O'Regan, B. and M. Grätzel, *A low-cost, high-efficiency solar cell based on dye-sensitized colloidal TiO2 films.* Nature, 1991. **353**(6346): p. 737-740.

[80] Bierman, M.J. and S. Jin, *Potential applications of hierarchical branching nanowires in solar energy conversion.* Energy & Environmental Science, 2009. **2**(10): p. 1050-1059.

[81] Cheng, C. and H.J. Fan, *Branched nanowires: Synthesis and energy applications.* Nano Today, 2012. **7**(4): p. 327-343.

[82] http://en.wikipedia.org/wiki/Titanium_dioxide.

[83] Li, G. and K.A. Gray, *The solid–solid interface: Explaining the high and unique photocatalytic reactivity of TiO2-based nanocomposite materials.* Chemical Physics, 2007. **339**(1–3): p. 173-187.

[84] Liu, G., et al., *Titania-based photocatalysts-crystal growth, doping and heterostructuring.* Journal of Materials Chemistry, 2010. **20**(5): p. 831-843.

[85] Ohno, T., et al., *Synergism between rutile and anatase TiO2 particles in photocatalytic oxidation of naphthalene.* Applied Catalysis A: General, 2003. **244**(2): p. 383-391.

[86] Liu, Z., et al., *Anatase TiO2 Nanoparticles on Rutile TiO2 Nanorods: A Heterogeneous Nanostructure via Layer-by-Layer Assembly.* Langmuir, 2007. **23**(22): p. 10916-10919.

[87] Li, G., et al., *Synthesizing mixed-phase TiO2 nanocomposites using a hydrothermal method for photo-oxidation and photoreduction applications.* Journal of Catalysis, 2008. **253**(1): p. 105-110.

[88] Zachariah, A., et al., *Synergistic Effect in Photocatalysis As Observed for Mixed-Phase Nanocrystalline Titania Processed via Sol−Gel Solvent Mixing and Calcination.* The Journal of Physical Chemistry C, 2008. **112**(30): p. 11345-11356.

[89] Kawahara, T., et al., *A Patterned TiO2(Anatase)/TiO2(Rutile) Bilayer-Type Photocatalyst: Effect of the Anatase/Rutile Junction on the Photocatalytic Activity.* Angewandte Chemie International Edition, 2002. **41**(15): p. 2811-2813.

[90] Hurum, D.C., et al., *Recombination Pathways in the Degussa P25 Formulation of TiO2: Surface versus Lattice Mechanisms.* The Journal of Physical Chemistry B, 2004. **109**(2): p. 977-980.

[91] Youngblood, W.J., et al., *Visible Light Water Splitting Using Dye-Sensitized Oxide Semiconductors.* Accounts of Chemical Research, 2009. **42**(12): p. 1966-1973.

[92] Mora-Seró, I.n. and J. Bisquert, *Breakthroughs in the Development of Semiconductor-Sensitized Solar Cells.* The Journal of Physical Chemistry Letters, 2010. **1**(20): p. 3046-3052.

[93] St. John, M.R., A.J. Furgala, and A.F. Sammells, *Hydrogen generation by photocatalytic oxidation of glucose by platinized n-titania powder.* The Journal of Physical Chemistry, 1983. **87**(5): p. 801-805.

[94] Bamwenda, G.R., et al., *Photoassisted hydrogen production from a water-ethanol solution: a comparison of activities of Au・TiO2 and Pt・TiO2.* Journal of Photochemistry and Photobiology A: Chemistry, 1995. **89**(2): p. 177-189.

[95] Kim, S. and W. Choi, *Dual Photocatalytic Pathways of Trichloroacetate Degradation on TiO2: Effects of Nanosized Platinum Deposits on Kinetics and Mechanism.* The Journal of Physical Chemistry B, 2002. **106**(51): p. 13311-13317.

[96] Subramanian, V., E.E. Wolf, and P.V. Kamat, *Catalysis with TiO2/Gold Nanocomposites. Effect of Metal Particle Size on the Fermi Level Equilibration.* Journal of the American Chemical Society, 2004. **126**(15): p. 4943-4950.

[97] Jakob, M., H. Levanon, and P.V. Kamat, *Charge Distribution between UV-Irradiated TiO2 and Gold Nanoparticles: Determination of Shift in the Fermi Level.* Nano Letters, 2003. **3**(3): p. 353-358.

[98] Liu, Z., et al., *Plasmon Resonant Enhancement of Photocatalytic Water Splitting Under Visible Illumination.* Nano Letters, 2011. **11**(3): p. 1111-1116.

[99] Mubeen, S., et al., *Plasmonic Photosensitization of a Wide Band Gap Semiconductor: Converting Plasmons to Charge Carriers.* Nano Letters, 2011. **11**(12): p. 5548-5552.

[100] Mubeen, S., et al., *An autonomous photosynthetic device in which all charge carriers derive from surface plasmons.* Nat Nano, 2013. **8**(4): p. 247-251.

[101] Grätzel, M., *Dye-sensitized solar cells.* Journal of Photochemistry and Photobiology C: Photochemistry Reviews, 2003. **4**(2): p. 145-153.

[102] Rühle, S., M. Shalom, and A. Zaban, *Quantum-Dot-Sensitized Solar Cells.* ChemPhysChem, 2010. **11**(11): p. 2290-2304.

[103] Youngblood, W.J., et al., *Photoassisted Overall Water Splitting in a Visible Light-Absorbing Dye-Sensitized Photoelectrochemical Cell.* Journal of the American Chemical Society, 2009. **131**(3): p. 926-927.

[104] Kamat, P.V., *Quantum Dot Solar Cells. Semiconductor Nanocrystals as Light Harvesters†.* The Journal of Physical Chemistry C, 2008. **112**(48): p. 18737-18753.

[105] Watson, D.F., *Linker-Assisted Assembly and Interfacial Electron-Transfer Reactivity of Quantum Dot-Substrate Architectures.* Journal of Physical Chemistry Letters, 2010. **1**(15): p. 2299-2309.

[106] Niitsoo, O., et al., *Chemical bath deposited CdS/CdSe-sensitized porous TiO2 solar cells.* Journal of Photochemistry and Photobiology A: Chemistry, 2006. **181**(2-3): p. 306-313.

[107] Chang, C.-H. and Y.-L. Lee, *Chemical bath deposition of CdS quantum dots onto mesoscopic TiO[sub 2] films for application in quantum-dot-sensitized solar cells.* Applied Physics Letters, 2007. **91**(5): p. 053503.

[108] Lee, H.J., et al., *Multilayered Semiconductor (CdS/CdSe/ZnS)-Sensitized TiO2 Mesoporous Solar Cells: All Prepared by Successive Ionic Layer Adsorption and Reaction Processes.* Chemistry of Materials, 2010. **22**(19): p. 5636-5643.

[109] Lee, H., et al., *Efficient CdSe Quantum Dot-Sensitized Solar Cells Prepared by an Improved Successive Ionic Layer Adsorption and Reaction Process.* Nano Letters, 2009. **9**(12): p. 4221-4227.

[110] Hossain, M.A., et al., *Carrier Generation and Collection in CdS/CdSe-Sensitized SnO2 Solar Cells Exhibiting Unprecedented Photocurrent Densities.* ACS Nano, 2011. **5**(4): p. 3172-3181.

[111] Banerjee, S., et al., *Synthesis of Coupled Semiconductor by Filling 1D TiO2 Nanotubes with CdS.* Chemistry of Materials, 2008. **20**(21): p. 6784-6791.

[112] Lee, J.-C., et al., *Growth of CdS Nanorod-Coated TiO2 Nanowires on Conductive Glass for Photovoltaic Applications.* Crystal Growth & Design, 2009. **9**(10): p. 4519-4523.

[113] Islam, M.A., et al., *Controlled Electrophoretic Deposition of Smooth and Robust Films of CdSe Nanocrystals.* Chemistry of Materials, 2003. **16**(1): p. 49-54.

[114] Zhu, K., et al., *Enhanced charge-collection efficiencies and light scattering in dye-sensitized solar cells using oriented TiO2 nanotubes arrays.* Nano Letters, 2007. **7**(1): p. 69-74.

[115] Zhuge, F., et al., *Toward hierarchical TiO2 nanotube arrays for efficient dye-sensitized solar cells.* Advanced Materials, 2011. **23**(11): p. 1330-1334.

[116] Kwak, E.S., et al., *Compact inverse-opal electrode using non-aggregated TiO2 nanoparticles for dye-sensitized solar cells.* Advanced Functional Materials, 2009. **19**(7): p. 1093-1099.

[117] Liu, L., et al., *TiO2 inverse-opal electrode fabricated by atomic layer deposition for dye-sensitized solar cell applications.* Energy and Environmental Science, 2011. **4**(1): p. 209-215.

[118] Nishimura, S., et al., *Standing wave enhancement of red absorbance and photocurrent in dye-sensitized titanium dioxide photoelectrodes coupled to photonic crystals.* Journal of the American Chemical Society, 2003. **125**(20): p. 6306-6310.

[119] Guldin, S., et al., *Dye-sensitized solar cell based on a three-dimensional photonic crystal.* Nano Letters, 2010. **10**(7): p. 2303-2309.

[120] Diguna, L.J., et al., *High efficiency of CdSe quantum-dot-sensitized Ti O2 inverse opal solar cells.* Applied Physics Letters, 2007. **91**(2).

[121] Cheng, C., et al., *Quantum-dot-sensitized TiO2 inverse opals for photoelectrochemical hydrogen generation.* Small, 2012. **8**(1): p. 37-42.

[122] Zhang, L., et al., *Bi2WO6 Inverse Opals: Facile Fabrication and Efficient Visible-Light-Driven Photocatalytic and Photoelectrochemical Water-Splitting Activity.* Small, 2011. **7**(19): p. 2714-2720.

[123] Tetreault, N., et al., *High-Efficiency Dye-Sensitized Solar Cell with Three-Dimensional Photoanode.* Nano Letters, 2011.

[124] Chen, X., et al., *Enhanced incident photon-to-electron conversion efficiency of tungsten trioxide photoanodes based on 3d-photonic crystal design.* ACS Nano, 2011. **5**(6): p. 4310-4318.

[125] Das, K. and S.K. De, *Optical Properties of the Type-II Core−Shell TiO2@CdS Nanorods for Photovoltaic Applications.* Journal of Physical Chemistry C, 2009. **113**(9): p. 3494-3501.

[126] Chen, X. and S.S. Mao, *Titanium Dioxide Nanomaterials: Synthesis, Properties, Modifications, and Applications.* Chemical Reviews, 2007. **107**(7): p. 2891-2959.

[127] Khan, S.U.M., *Efficient Photochemical Water Splitting by a Chemically Modified n-TiO2.* Science, 2002. **297**(5590): p. 2243-2245.

[128] Yu, J.C., et al., *Effects of F- doping on the photocatalytic activity and microstructures of nanocrystalline TiO2 powders.* Chemistry of Materials, 2002. **14**(9): p. 3808-3816.

[129] Banerjee, S., et al., *Synthesis of Coupled Semiconductor by Filling 1D TiO2Nanotubes with CdS.* Chemistry of Materials, 2008. **20**(21): p. 6784-6791.

[130] Li, J.H., et al., *CdS Quantum Dots-Sensitized TiO(2) Nanorod Array on Transparent Conductive Glass Photoelectrodes.* Journal of Physical Chemistry C, 2010. **114**(39): p. 16451-16455.

[131] Lee, J.-C., et al., *Growth of CdS Nanorod-Coated TiO2Nanowires on Conductive Glass for Photovoltaic Applications.* Crystal Growth & Design, 2009. **9**(10): p. 4519-4523.

[132] Kamat, P.V., et al., *Quantum dot solar cells. Tuning photoresponse through size and shape control of CdSe-TiO2 architecture.* Journal of the American Chemical Society, 2008. **130**(12): p. 4007-4015.

[133] Lee, H., et al., *Efficient CdSe quantum dot-sensitized solar cells prepared by an improved successive ionic layer adsorption and reaction process.* Nano Lett, 2009. **9**(12): p. 4221-7.

[134] Kramer, I.J., et al., *Solar Cells Using Quantum Funnels.* Nano Letters, 2011: p. 3701–3706.

[135] Lee, H., et al., *PbS and CdS Quantum Dot-Sensitized Solid-State Solar Cells: "Old Concepts, New Results".* Advanced Functional Materials, 2009. **19**(17): p. 2735-2742.

[136] Salant, A., et al., *Quantum Rod Sensitized Solar Cell; Nanocrystal shape effect on the Photovoltaic Properties.* Nano Letters, 2012.

[137] Guijarro, N., et al., *CdSe Quantum Dot-Sensitized TiO(2) Electrodes: Effect of Quantum Dot Coverage and Mode of Attachment.* Journal of Physical Chemistry C, 2009. **113**(10): p. 4208-4214.

[138] Myung, Y., et al., *Composition-tuned ZnO--CdSSe core--shell nanowire arrays.* ACS Nano, 2010. **4**(7): p. 3789-800.

[139] Cheng, S.L., et al., *Photoelectrochemical Performance of Multiple Semiconductors (CdS/CdSe/ZnS) Cosensitized TiO2 Photoelectrodes.* Journal of Physical Chemistry C, 2012. **116**(3): p. 2615-2621.

[140] Salant, A., et al., *Quantum Rod Sensitized Solar Cell; Nanocrystal shape effect on the Photovoltaic Properties.* Nano Letters, 2012. **12**(4): p. 2095–2100.

[141] Kuno, M. and J. Giblin, *Nanostructure Absorption: A Comparative Study of Nanowire and Colloidal Quantum Dot Absorption Cross Sections.* Journal of Physical Chemistry Letters, 2010. **1**(23): p. 3340-3348.

[142] Garnett, E.C., et al., *Nanowire Solar Cells.* Annual Review of Materials Research, 2011. **41**(1): p. 269-295.

[143] Aydil, E.S. and B. Liu, *Growth of Oriented Single-Crystalline Rutile TiO2 Nanorods on Transparent Conducting Substrates for Dye-Sensitized Solar Cells.* Journal of the American Chemical Society, 2009. **131**(11): p. 3985-3990.

[144] Zhang, J., F.H. Jiang, and L.D. Zhang, *Fabrication of single-crystalline semiconductor CdS nanobelts by vapor transport.* Journal of Physical Chemistry B, 2004. **108**(22): p. 7002-7005.

[145] Wu, X.C. and Y.R. Tao, *Growth of CdS nanowires by physical vapor deposition.* Journal of Crystal Growth, 2002. **242**(3-4): p. 309-312.

[146] Shen, G.Z. and C.J. Lee, *CdS multipod-based structures through a thermal evaporation process.* Crystal Growth & Design, 2005. **5**(3): p. 1085-1089.

[147] Yamai, I. and H. Saito, *Vapor-Phase Growth of Alumina Whiskers by Hydrolysis of Aluminum Fluoride.* Journal of Crystal Growth, 1978. **45**(1): p. 511-516.

[148] Umar, A., et al., *Catalyst-free large-quantity synthesis of ZnO nanorods by a vapor–solid growth mechanism: Structural and optical properties.* Journal of Crystal Growth, 2005. **282**(1-2): p. 131-136.

[149] Fan, H.J., et al., *On the growth mechanism and optical properties of ZnO multi-layer nanosheets.* Applied Physics A, 2004. **79**(8).

[150] Matsumura, M., et al., *Cadmium-Sulfide Photocatalyzed Hydrogen-Production from Aqueous-Solutions of Sulfite - Effect of Crystal-Structure and Preparation Method of the Catalyst.* Journal of Physical Chemistry, 1985. **89**(8): p. 1327-1329.

[151] Shi, J., et al., *Photoluminescence Characteristics of TiO2 and Their Relationship to the Photoassisted Reaction of Water/Methanol Mixture.* The Journal of Physical Chemistry C, 2006. **111**(2): p. 693-699.

[152] Mora-Sero, I. and J. Bisquert, *Breakthroughs in the Development of Semiconductor-Sensitized Solar Cells.* Journal of Physical Chemistry Letters, 2010. **1**(20): p. 3046-3052.

[153] Mora-Sero, I., et al., *Recombination in quantum dot sensitized solar cells.* Acc Chem Res, 2009. **42**(11): p. 1848-57.

[154] Mora-Sero, I., et al., *Modeling High-Efficiency Quantum Dot Sensitized Solar Cells.* Acs Nano, 2010. **4**(10): p. 5783-5790.

[155] Chi, C.F., et al., *Energy level alignment, electron injection, and charge recombination characteristics in CdS/CdSe cosensitized TiO(2) photoelectrode.* Applied Physics Letters, 2011. **98**(1).

[156] Robel, I., et al., *Quantum Dot Solar Cells. Harvesting Light Energy with CdSe Nanocrystals Molecularly Linked to Mesoscopic TiO2 Films.* Journal of the American Chemical Society, 2006. **128**(7): p. 2385-2393.

[157] van de Krol, R., Y.Q. Liang, and J. Schoonman, *Solar hydrogen production with nanostructured metal oxides.* Journal of Materials Chemistry, 2008. **18**(20): p. 2311-2320.

[158] Chakrapani, V., D. Baker, and P.V. Kamat, *Understanding the Role of the Sulfide Redox Couple (S(2-)/S(n)(2-)) in Quantum Dot-Sensitized Solar Cells.* Journal of the American Chemical Society, 2011. **133**(24): p. 9607-9615.

[159] Lin, K.H., et al., *Charge Transfer in the Heterointerfaces of CdS/CdSe Cosensitized TiO2 Photoelectrode.* Journal of Physical Chemistry C, 2012. **116**(1): p. 1550-1555.

[160] Kamat, P.V., et al., *Beyond photovoltaics: Semiconductor nanoarchitectures for liquid-junction solar cells.* Chemical Reviews, 2010. **110**(11): p. 6664-6688.

[161] Varghese, O.K., M. Paulose, and C.A. Grimes, *Long vertically aligned titania nanotubes on transparent conducting oxide for highly efficient solar cells.* Nature Nanotechnology, 2009. **4**(9): p. 592-597.

[162] Chen, D., et al., *Mesoporous anatase TiO2 beads with high surface areas and controllable pore sizes: A superior candidate for high-performance dye-sensitized solar cells.* Advanced Materials, 2009. **21**(21): p. 2206-2210.

[163] Luo, Y., D. Li, and Q. Meng, *Towards optimization of materials for dye-sensitized solar cells.* Advanced Materials, 2009. **21**(45): p. 4647-4651.

[164] Zhang, Q., et al., *Aggregation of ZnO nanocrystallites for high conversion efficiency in dye-sensitized solar cells.* Angewandte Chemie - International Edition, 2008. **47**(13): p. 2402-2406.

[165] Zhang, Q. and G. Cao, *Nanostructured photoelectrodes for dye-sensitized solar cells.* Nano Today, 2011. **6**(1): p. 91-109.

[166] Lee, Y.-L., C.-F. Chi, and S.-Y. Liau, *CdS/CdSe Co-Sensitized TiO2Photoelectrode for Efficient Hydrogen Generation in a Photoelectrochemical Cell†.* Chemistry of Materials, 2010. **22**(3): p. 922-927.

[167] Tvrdy, K., P.A. Frantsuzov, and P.V. Kamat, *Photoinduced electron transfer from semiconductor quantum dots to metal oxide nanoparticles.* Proceedings of the National Academy of Sciences of the United States of America, 2011. **108**(1): p. 29-34.

[168] Marlow, F., et al., *Opals: Status and prospects.* Angewandte Chemie - International Edition, 2009. **48**(34): p. 6212-6233.

[169] Karuturi, S.K., et al., *Kinetics of stop-flow atomic layer deposition for high aspect ratio template filling through photonic band gap measurements.* Journal of Physical Chemistry C, 2010. **114**(35): p. 14843-14848.

[170] Cheng, C.W., et al., *Quantum-Dot-Sensitized TiO2 Inverse Opals for Photoelectrochemical Hydrogen Generation.* Small, 2012. **8**(1): p. 37-42.

[171] Cheng, C., et al., *Fabrication and SERS performance of silver-nanoparticle-decorated Si/ZnO nanotrees in ordered arrays.* ACS Applied Materials and Interfaces, 2010. **2**(7): p. 1824-1828.

[172] Baker, D.R. and P.V. Kamat, *Photosensitization of TiO2 nanostructures with CdS quantum dots: Particulate versus tubular support architectures.* Advanced Functional Materials, 2009. **19**(5): p. 805-811.

[173] Liu, L., et al., *Electrochromic photonic crystal displays with versatile color tunability.* Electrochemistry Communications, 2011(13): p. 1163-1165.

[174] Juarez, B.H., et al., *ZnO inverse opals by chemical vapor deposition.* Advanced Materials, 2005. **17**(22): p. 2761-2765.

[175] King, J.S., E. Graugnard, and C.J. Summers, *TiO2 inverse opals fabricated using low-temperature atomic layer deposition.* Advanced Materials, 2005. **17**(8): p. 1010-1013.

[176] Scharrer, M., et al., *Fabrication of inverted opal ZnO photonic crystals by atomic layer deposition.* Applied Physics Letters, 2005. **86**(15): p. 1-3.

[177] Xu, C., et al., *Preferential growth of long ZnO nanowire array and its application in dye-sensitized solar cells.* Journal of Physical Chemistry C, 2010. **114**(1): p. 125-129.

[178] Busch, K. and S. John, *Photonic band gap formation in certain self-organizing systems.* Physical Review E - Statistical Physics, Plasmas, Fluids, and Related Interdisciplinary Topics, 1998. **58**(3 SUPPL. B): p. 3896-3908.

[179] Lodahl, P., et al., *Controlling the dynamics of spontaneous emission from quantum dots by photonic crystals.* Nature, 2004. **430**(7000): p. 654-657.

[180] Vanmaekelbergh, D. and L.K. Van Vugt, *ZnO nanowire lasers.* Nanoscale, 2011. **3**(7): p. 2783-2800.

[181] Zhang, Q., et al., *Polydisperse aggregates of ZnO nanocrystallites: A method for energy-conversion-efficiency enhancement in dye-sensitized solar cells.* Advanced Functional Materials, 2008. **18**(11): p. 1654-1660.

[182] Chen, J.I.L., et al., *Effect of disorder on the optically amplified photocatalytic efficiency of titania inverse opals.* Journal of the American Chemical Society, 2007. **129**(5): p. 1196-1202.

[183] Neale, N.R., et al., *Near-infrared light trapping in disordered inverse opals.* Journal of Physical Chemistry C, 2011. **115**(29): p. 14341-14346.

[184] Galisteo-Lopez, J.F., et al., *Optical study of the pseudogap in thickness and orientation controlled artificial opals.* Physical Review B - Condensed Matter and Materials Physics, 2003. **68**(11): p. 1151091-1151098.

[185] Palomares, E., et al., *Control of charge recombination dynamics in dye sensitized solar cells by the use of conformally deposited metal oxide blocking layers.* Journal of the American Chemical Society, 2003. **125**(2): p. 475-482.

[186] Chen, C., et al., *Improved conversion efficiency of CdS quantum dots-sensitized TiO 2 nanotube array using ZnO energy barrier layer.* Nanotechnology, 2011. **22**(1): p. 015202.

[187] Lee, W., et al., *TiO2 nanotubes with a ZnO thin energy barrier for improved current efficiency of CdSe quantum-dot-sensitized solar cells.* Nanotechnology, 2009. **20**(33).

[188] Chen, X. and S.S. Mao, *Titanium dioxide nanomaterials: Synthesis, properties, modifications, and applications.* Chemical Reviews, 2007. **107**(7): p. 2891-2959.

[189] Oregan, B. and M. Gratzel, *A Low-Cost, High-Efficiency Solar-Cell Based on Dye-Sensitized Colloidal Tio2 Films.* Nature, 1991. **353**(6346): p. 737-740.

[190] Kamat, P.V., *Quantum Dot Solar Cells. Semiconductor Nanocrystals as Light Harvesters.* Journal of Physical Chemistry C, 2008. **112**(48): p. 18737-18753.

[191] Serpone, N. and A.V. Emeline, *Semiconductor Photocatalysis — Past, Present, and Future Outlook.* The Journal of Physical Chemistry Letters, 2012. **3**(5): p. 673-677.

[192] Serpone, N., E. Borgarello, and M. Gratzel, *Visible-Light Induced Generation of Hydrogen from H2s in Mixed Semiconductor Dispersions - Improved Efficiency through Inter-Particle Electron-Transfer.* Journal of the Chemical Society, Chemical Communications, 1984(6): p. 342-344.

[193] Alivisatos, A.P., *Semiconductor Clusters, Nanocrystals, and Quantum Dots.* Science, 1996. **271**(5251): p. 933-937.

[194] Peng, Z.A. and X. Peng, *Formation of High-Quality CdTe, CdSe, and CdS Nanocrystals Using CdO as Precursor.* Journal of the American Chemical Society, 2000. **123**(1): p. 183-184.

[195] George, S.M., *Atomic Layer Deposition: An Overview.* Chemical Reviews, 2010. **110**(1): p. 111-131.

[196] Brennan, T.P., et al., *Atomic Layer Deposition of CdS Quantum Dots for Solid-State Quantum Dot Sensitized Solar Cells.* Advanced Energy Materials, 2011. **1**(6): p. 1169-1175.

[197] Son, D.H., et al., *Cation Exchange Reactions in Ionic Nanocrystals.* Science, 2004. **306**(5698): p. 1009-1012.

[198] Robinson, R.D., et al., *Spontaneous Superlattice Formation in Nanorods Through Partial Cation Exchange.* Science, 2007. **317**(5836): p. 355-358.

[199] Tang, J., et al., *Solution-processed core-shell nanowires for efficient photovoltaic cells.* Nat Nano, 2011. **6**(9): p. 568-572.

[200] Myung, Y., et al., *Composition-Tuned ZnO−CdSSe Core−Shell Nanowire Arrays.* Acs Nano, 2010. **4**(7): p. 3789-3800.

[201] Xu, J., et al., *Arrays of ZnO/ZnxCd1–xSe Nanocables: Band Gap Engineering and Photovoltaic Applications.* Nano Letters, 2011. **11**(10): p. 4138-4143.

[202] Fan, H.J., Y. Yang, and M. Zacharias, *ZnO-based ternary compound nanotubes and nanowires.* Journal of Materials Chemistry, 2009. **19**(7): p. 885-900.

[203] Liu, L., et al., *TiO2 inverse-opal electrode fabricated by atomic layer deposition for dye-sensitized solar cell applications.* Energy & Environmental Science, 2011. **4**(1): p. 209-215.

[204] Yamada, A., B. Sang, and M. Konagai, *Atomic layer deposition of ZnO transparent conducting oxides.* Applied Surface Science, 1997. **112**(0): p. 216-222.

[205] Lee, Y.-L., C.-F. Chi, and S.-Y. Liau, *CdS/CdSe Co-Sensitized TiO2 Photoelectrode for Efficient Hydrogen Generation in a Photoelectrochemical Cell†.* Chemistry of Materials, 2009. **22**(3): p. 922-927.

[206] Mora-Seró, I.n., et al., *Recombination in Quantum Dot Sensitized Solar Cells.* Accounts of Chemical Research, 2009. **42**(11): p. 1848-1857.

[207] Santra, P.K. and P.V. Kamat, *Mn-Doped Quantum Dot Sensitized Solar Cells: A Strategy to Boost Efficiency over 5%.* Journal of the American Chemical Society, 2012. **134**(5): p. 2508-2511.

[208] Buehler, N., K. Meier, and J.F. Reber, *Photochemical hydrogen production with cadmium sulfide suspensions.* The Journal of Physical Chemistry, 1984. **88**(15): p. 3261-3268.

[209] Pelizzetti, E., et al., *Photocatalytic Cleavage Of Hydrogen Sulfide And Organosulfur Compounds*, in *Studies in Surface Science and Catalysis*, S. Kaliaguine and A. Mahay, Editors. 1984, Elsevier. p. 327-334.

[210] Serpone, N., E. Borgarello, and M. Gratzel, *Visible light induced generation of hydrogen from H2S in mixed semiconductor dispersions; improved efficiency through inter-particle electron transfer.* Journal of the Chemical Society, Chemical Communications, 1984(6): p. 342-344.

[211] Meissner, D., R. Memming, and B. Kastening, *Photoelectrochemistry of cadmium sulfide. 1. Reanalysis of photocorrosion and flat-band potential.* The Journal of Physical Chemistry, 1988. **92**(12): p. 3476-3483.

[212] Rubin, H.-D., B.D. Humphrey, and A.B. Bocarsly, *Role of surface reactions in the stabilization of n-CdS-based photoelectrochemical cells.* Nature, 1984. **308**(5957): p. 339-341.

[213] Smotkin, E.S., et al., *Bipolar cadmium selenide/cobalt(II) sulfide semiconductor photoelectrode arrays for unassisted photolytic water splitting.* The Journal of Physical Chemistry, 1987. **91**(1): p. 6-8.

[214] Schneider, J. and D.W. Bahnemann, *Undesired Role of Sacrificial Reagents in Photocatalysis.* The Journal of Physical Chemistry Letters, 2013. **4**(20): p. 3479-3483.

[215] Ma, G., et al., *Direct splitting of H2S into H2 and S on CdS-based photocatalyst under visible light irradiation.* Journal of Catalysis, 2008. **260**(1): p. 134-140.

[216] Paracchino, A., et al., *Highly active oxide photocathode for photoelectrochemical water reduction.* Nat Mater, 2011. **10**(6): p. 456-461.

[217] Kenney, M.J., et al., *High-Performance Silicon Photoanodes Passivated with Ultrathin Nickel Films for Water Oxidation.* Science, 2013. **342**(6160): p. 836-840.

[218] Trevisan, R., et al., *Harnessing Infrared Photons for Photoelectrochemical Hydrogen Generation. A PbS Quantum Dot Based "Quasi-Artificial Leaf".* The Journal of Physical Chemistry Letters, 2012. **4**(1): p. 141-146.

[219] Khaselev, O. and J.A. Turner, *A Monolithic Photovoltaic-Photoelectrochemical Device for Hydrogen Production via Water Splitting.* Science, 1998. **280**(5362): p. 425-427.